Master Thesis : Room temperature wear behavior of laser clad 316L+WC composite coating

Auteur : Mario, Daniele
Promoteur(s) : Mertens, Anne
Faculté : Faculté des Sciences appliquées
Diplôme : Cours supplémentaires destinés aux étudiants d'échange (Erasmus, ...)
Année académique : 2018-2019
URI/URL : http://hdl.handle.net/2268.2/6636

Université de Liège – Università degli Studi di Padova

Faculté des Sciences Appliquées -Scuola di Ingegneria

Room temperature wear behavior of laser clad 316L+WC composite coating

DANIELE MARIO

Final Year Project

Supervisors:

Prof. ANNE MERTENS

Prof. IRENE CALLIARI

Academic year: 2018/2019

Abstract

Additive manufacturing (AM), also known as three-dimensional (3D) printing, has experienced significant growth over the past 25 years in several areas, ranging from the conception of new machines to the number and complexity of parts produced. Consequently, an equivalent interest and development is increased in the form of publications and patents.

Currently only few alloys, the most relevant being some Stainless steels, TiAl6V4, AlSi10Mg, Inconel 718 and CoCr, can be reliably printed. Indeed, the vast majority of the more than 5,500 alloys used in today industry cannot be additively manufactured due to the formation of intolerable microstructures with periodic cracks, the problems to obtain them as AM feedstock or the lower mechanical properties in comparison to traditional parts. Nowadays just 50 alloys are commercially available alloys for AM. A handful more are being researched, but it remains a tremendous opportunity in processing new material and in developing new alloys specifically for AM and by AM. Indeed, a particularly interesting research field is the conception of alloys that are only accessible due to the peculiar, powder-metallurgical and non-equilibrium characteristics of AM processing. The improvement or modification of existing alloys by AM may be a further step in some problems resolution or the opening of new applications and possibilities for the industries.

The 316L stainless steel is a metal widely used in construction, automotive and medicine due to excellent corrosion resistance and mechanical properties. The main drawback of the 316L is the weak wear resistance. To overcome this weakness, the improvement in wear resistance could be achieved by the introduction of a harder reinforcement during fabrication by Laser Cladding (LC), creating a Metal Matrix Composite (MMC) coating on the surface of the SS316L part. The LC is an AM technology, also known as Direct Metal Deposition, capable to handle two different powders that are fed into a focused laser beam while being scanned across a substrate, thus leaving behind a coating or object. Among the possible reinforcements, tungsten carbide (WC) is a promising candidate due to its hardness, chemical affinity and theoretical high melting temperature higher than 2200°C. This new material by AM presents peculiar features in its microstructure and it is supposed to have enhanced mechanical properties than the pure SS316L. This work is focused on the understanding of the wear behavior of the MMC based on SS316L and 20% (vol. %) of WC.

Firstly, microstructural and chemical analysis were performed to characterize the new composite. Slight inhomogeneities in the carbides distribution lead to slight variations of the hardness. Moreover, the introduction of tungsten carbides in the 316L stainless steel has a reinforcing action.

Many phases were detected inside the material. Near to the original tungsten carbides (coming from the raw powder material for the cladding) and in the Heat Affected Zone close-to-equilibrium M_6C and $M_{23}C_6$ carbides were well recognized. Instead, inside the track, complex-regular shaped out-

of-equilibrium carbides were observed. The analysis performed did not allow to fully understand their nature. The wear tests were performed after the microstructural characterization and the investigation on its influence on the hardness.

All the samples shown almost the same friction behavior characterized by some different steps in the Coefficient Of Friction (COF) evolution. Each of these stages suggested the presence of many wear mechanisms acting during the tests. Hence, shorter tests were carried out in order to check the wear response of the material for each COF evolutions. Profilometer measurements allowed to evaluate the dimensions of the worn track and the worn Al_2O_3 ball. With the cross consideration of pin-on-disk results, profilometer analysis and SEM observation, it was possible to understand the wear behavior of the SS316L+WC composite material.

After only few cycles a very consistent part of the wear already takes place. Indeed, several wear mechanisms that leads to materials consumption act just at the beginning of the tests. Proofs of adhesive wear, abrasion wear (especially 2-body type) and delamination were found related to the evolutions of the COF within 1500/2000 cycles. In this part of the experiments the formation of the tribolayer begins. Material consumption continues further. The oxidation of the tribolayer gives a steady COF period. Typical of this wear mechanism is the action of protection by the tribolayer on the samples. When the thickness reaches a critical value and when the strain accumulation cannot be sustained anymore, the partially oxidized tribolayer breaks down. The debris resulting from this phenomenon act as 3rd body between the sample and the alumina ball. Thus, weak abrasion wear (3-body type) take place. When the debris go away abrasion, adhesion and delamination act again till the beginning of the oxidation of a second newly formed tribolayer. The second COF steady state and the second COF drop observed in some uninterrupted tests, suggests a sort of repetitiveness of some wear mechanism corresponding to the COF cycling evolution.

Table of Contents

List of Figures

List of Tables

1.   Introduction

Additive manufacturing (AM), also known as three-dimensional (3D) printing, has experienced significant growth over the past 25 years in several areas, ranging from the conception of new machines to the number and complexity of parts produced. Consequently, an equivalent interest and development is increased in the form of publications and patents.

AM is also increasingly being explored targeting the development of new products, homogeneous mechanical properties and a better part quality due to a series of problems, i.e. inadequate dimensional tolerance, presence of defects, surface roughness, and residual stress can limit its use in high-value or mission-critical applications.

Currently only few alloys, the most relevant being some Stainless steels, TiAl6V4, AlSi10Mg, Inconel 718 and CoCr, can be reliably printed. Indeed, the vast majority of the more than 5,500 alloys used in today industry cannot be additively manufactured due to the formation of intolerable microstructures with periodic cracks, the problems to obtain them as AM feedstock or the lower mechanical properties in comparison to traditional parts. Nowadays just 50 alloys are commercially available alloys for AM. A handful more are being researched, but it remains a tremendous opportunity in processing new material and in developing new alloys specifically for AM and by AM. Indeed, a particularly interesting research field is the conception of alloys that are only accessible due to the peculiar, powder-metallurgical and non-equilibrium characteristics of AM processing. The improvement or modification of existing alloys by AM may be a further step in some problems resolution or the opening of new applications and possibilities for the industries.

The 316L stainless steel is a metal widely used in construction, automotive and medicine due to excellent corrosion resistance and mechanical properties. The main drawback of the 316L is the weak wear resistance. To overcome this weakness, the improvement in wear resistance could be achieved by the introduction of a harder reinforcement during fabrication by Laser Cladding (LC), creating a Metal Matrix Composite (MMC) coating on the surface of the 316L part. The LC is an AM technology, also known as Direct Metal Deposition, capable to handle two different powders that are fed into a focused laser beam while being scanned across a substrate, thus leaving behind a coating or object. Among the possible reinforcements, tungsten carbide (WC) is a promising candidate due to its hardness, chemical affinity and theoretical high melting temperature higher than 2200°C. This new material by AM presents peculiar features in its microstructure and it is supposed to have enhanced mechanical properties than the pure SS316L. This work is focused on the understanding of the wear behavior of the MMC based on 316L and 20% (vol. %) of WC. Firstly, the microstructure was briefly analyzed, and special attention was given to the carbides distribution and the phases

formed during solidification are underlined. Hardness tests were performed in order to have an idea about the influence of the WC on the mechanical properties of the composite. The main part of this study was about the wear tests conducted by a pin-on-disc device. The further investigations were carried out by profilometer and by Scanning Electron Microscope (SEM) on the post-mortem surfaces in order to observe the worn tracks produced by the experiments and the worn counterpart pin. From those analyses, it is possible to fully elucidate to the wear behavior of the MMC.

2. *State of the art*

In this section, the state of the art is shown. First, the different *Additive Manufacturing* (AM) technologies (1) are presented, focusing on the *Laser Cladding* (LC) technique. A brief description of the composite materials and particularly of the *Metal Matrix Composites* (MMC) (2) is provided. The materials used in this work, which are 316L stainless steel and Tungsten carbides powders are described (3) with a short review which depict the microstructures that are present in the 316L stainless steel subjected to the LC process. At the end of this section, the wear and the tribology processes are illustrated (4).

2.1 *Additive Manufacturing*

Additive Manufacturing (AM) can be used to produce different objects made of different materials such as metals, polymers, ceramics and composites. The definition is given by the ISO/ASTM 52900-15: "process of joining materials to make objects from 3D model data, usually layer upon layer, as opposed to subtractive manufacturing methodologies" [2].

This relatively new processing route can be applied in different fields like automotive, aerospace and every day life [3]. The production of a piece is quite easy with the use of a CAD (Computer-Aided Design [4]) file and a machine suitable for the material we want to use. AM is a very attractive technology and it has already replaced the traditional techniques for production of medical implants, dentures, fashion objects, aircraft and engine parts. Many factories are interested in the AM routes because of their advantages such as: less waste produced in comparison with the machining process, a possibility to increase the geometric complexity of the object without increasing the production cost, weight reduction by rethinking the shape, short delivery times. Moreover some techniques allow the addition of functionalities and one-shot manufacturing of multi-material [5].

The AM is characterized by high cooling rates that bring to a fine structure. The laser processes lead to solidification in metals that is more cellular dendritic instead of the classical columnar dendric owned by the casting routes as Y. Lee et al. [6] report.

Figure 2-1: Correlation between Temperature gradient (G), Solidification rate (R) and the microstructure [6]

Moreover C. Navas et al. and also V. Balla e al. [7,8] noticed that the laser cladding process (which is a particular AM technique, as it will be shown in the follow) can enhance the proprieties, i.e. the wear behavior.

Thus, to take advantage of all these opportunities a good knowledge of the different processes, including the resulting microstructures, and the properties of the end objects is required.

2.1.1 Additive Manufacturing techniques

In the market, there are many different machines based on different AM concepts. The different AM processes can be classified i.e. on basis of the feedstock material, the energy source used and the building volume Table 2-1 is a list of the most common systems. The three main categories are: powder bed system, powder feed system and wire feed system [9].

Table 2-1: Main AM system and equipment sources [9]

System	Process	Build volume (mm)	Energy source
Powder bed			
ARCAM (A2)(a)	EBM	$200 \times 200 \times 350$	7 kW electron beam
EOS (M280)(b)	DMLS	$250 \times 250 \times 325$	200-400 W Yb-fiber laser
Concept laser cusing (M3)(b)	SLM	$300 \times 350 \times 300$	200 W fiber laser
MTT (SLM 250)(b)	SLM	$250 \times 250 \times 300$	100-400 W Yb-fiber laser
Phenix system group (PXL)(c)	SLM	$250 \times 250 \times 300$	500 W fiber laser
Renishaw (AM 250)(d)	SLM	$245 \times 245 \times 360$	200 or 400 W laser
Realizer (SLM 250)(b)	SLM	$250 \times 250 \times 220$	100, 200, or 400 W laser
Matsuura (Lumex Advanced 25)(e)	SLM	250×250 diameter	400 W Yb fiber laser; hybrid additive/subtractive system
Powder feed			
Optomec (LENS 850-R)(f)	LENS	$900 \times 1500 \times 900$	1 or 2 kW IPG fiber laser
POM DMD (66R)(f)	DMD	$3,200° \times 3°,670° \times 360°$	1-5 kW fiber diode or disk laser
Accufusion laser consolidation(g)	LC	$1,000 \times 1,000 \times 1,000$	Nd:YAG laser
Irepa laser (LF 6000)(c)	LD		Laser cladding
Trumpf(b)	LD	$600 \times 1,000$ long	
Huffman (HC-205)(f)	LD		CO_2 laser clading
Wire feed			
Sciaky (NG1) EBFFF(f)	EBDM	$762 \times 483 \times 508$	>40 kW @ 60 kV welder
MER plasma transferred arc selected FFF(f)	PTAS FFF	$610 \times 610 \times 5,182$	Plasma transferred arc using two 350A DC power supplies
Honeywell ion fusion formation(f)	IFF		Plasma arc-based welding

Country of Manufacturer: (a) Sweden, (b) Germany, (c) France, (d) United Kingdom, (e) Japan, (f) United States, and (g) Canada

➤ *Powder bed system:* a thin layer of powder is spread by a coater. Then it is scanned by the energy source (laser or electron beam) that melts or sinters the powder in the desired shape controlled by the CAD file (STL). During the second step, the working plate is lowered, another powder layer is spread by the coater and the energy source scans the new deposited powder. The process is repeated until the object, designed with the CAD software, is created. The advantages of this technique are the high resolution, the capability to produce complex lattices and the large range of material.
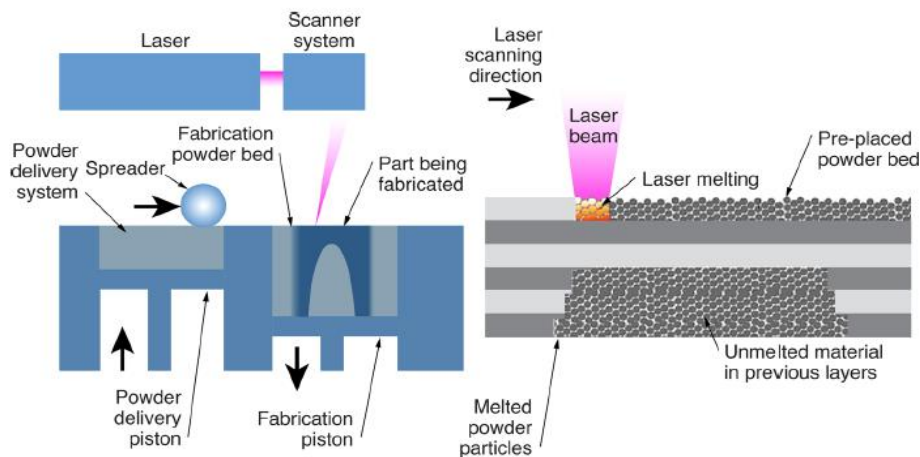
Figure 2-2: Schematic illustration of a powder bed AM system [10]

➢ *Powder feed system:* in this technique the powder is fed in a nozzle and deposited on the build surface. At the same time, a laser provides heat to melt the powder. These systems are especially used to repair worn or damaged parts. The main advantage of this manufacturing process is the use of many materials. This can be obtained through the additional feeding of a different types of powder. Other two advantages are the possibility to build a large volume and a gain a good control of the quantity of the material that is deposited.
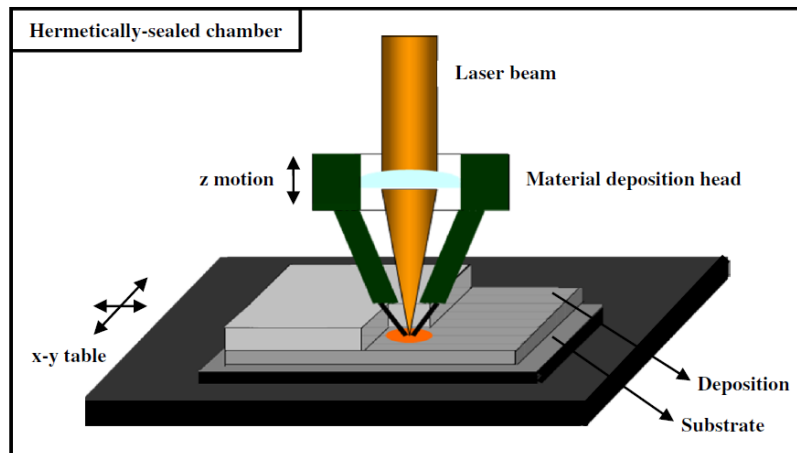
Figure 2-3: Schematic illustration of a powder feed AM system [3]

➢ *Wire feed system:* the feedstock material is in form of a wire. The energy source can either be an electron beam, a laser or even a plasma arc. At the beginning, a single track is deposited, then through different sequentially passes the 3D structure is built. This technique allows a high deposition rate of material and it is well suited for the building of large volumes.
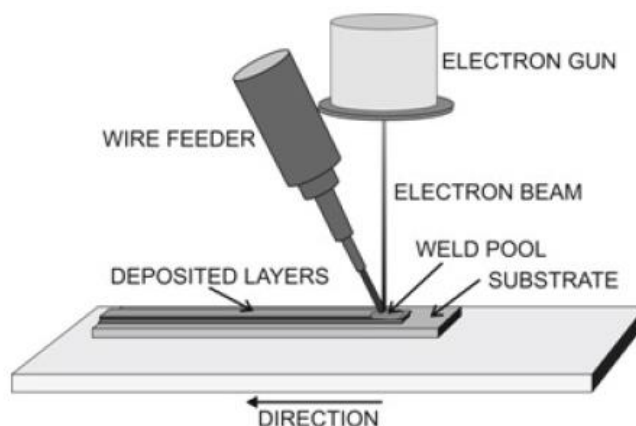
Figure 2-4: Schematic illustration of a wire feed AM system [11]

The most common AM processes for the metal parts production are: Laser Beam Melting (LBM), Electron Beam Melting (EBM), and Laser Metal Deposition (LMD). The LBM route is also known as Selective Laser Melting (SLM), Direct Metal Laser Sintering (DMLS) or industrial 3D printing. The LMD technology is also called Direct Metal Deposition (DMD), Laser Cladding (LC) or laser deposition welding. There are several different names to designate the same techniques, corresponding to trademarks of the different machine manufacturers.

2.1.2 Laser cladding (LC)

Laser cladding is a LMD process. In this technique a laser energy source is utilized to deposit a thin layer of metal on a substrate in order to reach a pore- and crack-free coating. This coating is perfectly bonded with the substrate thanks to the very low dilution between the substrate itself and the coating. The material transfer can be performed using different methods: powder injection, pre-placed powder on the substrate, or wire feeding. The pre-placed powder method is a two-step process where the material is deposited on the substrate and then scanned by the laser to ensure the formation of the coating by the melting the powder. The powder injection and the wire feeding are single-step processes in which the feeding material is supplied continuously into the nozzle while the laser provides heat. The single-step process is the only one that is really used because it is more energy-efficient and it allows for better process control and reproducibility. The powder based is the most use because in the wire process the laser energy is poorly absorbed [12]. Indeed, the powder injection LC allows to control the composition of the material during the whole process. This is a huge advantage of this technique and it is very useful in the production of composites.

A carrier gas is needed to carry the clad material to the nozzle. The powder stream is blown under the laser beam which generates the melt pool. The powder can be fed with an angle between 0° and 45° with respect to the melt pool. The mostly commonly used carrier gas is Argon, as it is an inert gas and the contamination of the powder is highly undesired. Some researchers found that the best efficiency is achieved when the powder arrives almost perpendicular to the substrate [13].
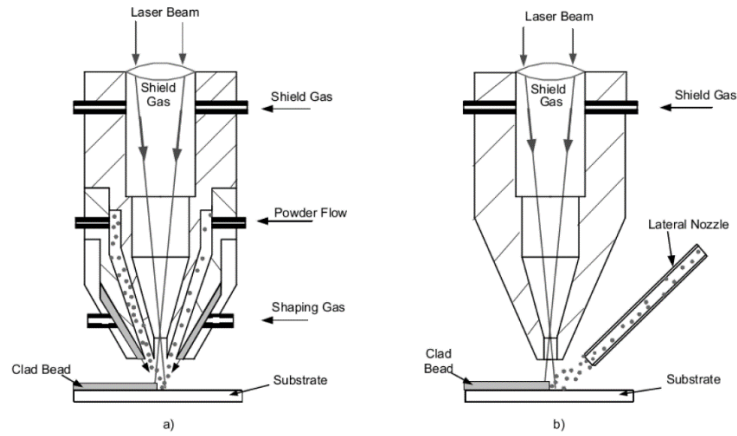
Figure 2-5: Coaxial (left) and lateral (right) laser cladding powder feeding [14]

Moreover, when the powder is delivered almost coaxially with the laser beam, all the directions of the substrate movement on a plane perpendicular to the laser beam are equivalent. Therefore, it is possible to create equal tracks independently on the moving direction of the specimen [15].

One clad track is formed by one scan of the laser beam. Overlapping tracks are made for a complete surface coverage: the powder and a thin layer of the previous deposit must be melted when a new track is deposited, this in order to avoid insufficient adhesion of the coating and the formation of defects [12].

A wide range of materials is suitable for the LC process with the powder feed technology. The process is very complex because many parameters must be optimized in order to obtain the best results possible. The most important parameters are: laser power, scanning speed and powder feeding rate but several additional parameters play an important role on the fabrication's quality, i.e. the spot size of the laser beam. Furthermore, it is important to analyze the different type of interactions (i.e. laser beam/powder) and the physical phenomena like mass and heat transfer, fluid flow and phase transformation. De Oliveira et al. underlined these events in their work [16].

Inputs

Laser
- Average power
- Spot size
- Wave length
- Pulsed/CW
- Beam profile
- Laser pulse shaping

Motion Device
- Relative velocity
- Relative acceleration
- System accuracy

Material
- Substrate geometry
- Composition
- Metallurgical, thermo physical & optical properties
- Powder size
- Surface tension

Powder Feeder
- Powder feed rate
- Inert gas flow rate
- Nozzle specification
- Powder stream profile

Ambient Properties
- Preheating
- Shield gas velocity
- Kind of shield gas

Processes

Physical phenomena
- Absorption
- Conduction
- Diffusion
- Melt pool dynamics
- Fluid convection
- Gas/melt pool interaction
- Laser attenuation by powder
- Rapid solidification

Outputs

Clad quality
- Geometry
- Microstructure
- Hardness
- Cracks
- Pores
- Residual stresses
- Surface roughness
- Microstructure
- Dilution

Figure 2-6: Schematic illustration of a wire feed AM system [17].

9

2.2 Composite materials

In the recent years the industries have started requiring very performant materials to be ready to the technological evolutions in the automotive, aerospace, marine and nuclear fields. These must be able to withstand extreme working conditions without losing their mechanical properties. Strength, high temperature resistance and wear resistance are required, as well as lightweight [15–17]. To fulfill all these characteristics, researchers try to enhance the performance of the materials currently available, i.e. they try to combine different materials to create composites. These new class of materials typically consists of: i) a matrix as a continuous phase; ii) a reinforcement as a discontinuous or dispersed phase, and sometimes iii) an interface or binder [18]. The reinforcement can be introduced in different forms i.e. as: i) particles (spherical); ii) fibers (short or long, aligned or random); and iii) platelets [19].

As shown in section 2.1, the AM has lots of advantages, i.e. the short delivery product time. AM is used also in the production of the composites materials [20].

2.2.1 Metal Matrix Composites (MMCs)

The Metal Matrix Composites (MMCs) as the name suggests, are a particular class of composite materials in which the matrix is a metallic material. They are typically used as abrasion resistant materials. In literature there are many examples of different combinations i.e. titanium alloys matrix reinforced with titanium borides and carbides [19], aluminum matrix reinforced with silicon carbides [21] , and even stainless steel matrix reinforced with titanium borides [22]. In these materials, a ceramic phase is introduced as reinforcement to enhance the properties of the metal, properties such as strength, stiffness, and wear resistance [23]. Indeed graphite, silicon carbide, titanium carbide, and tungsten carbide are commonly used in AM of MMCs [18]. The reinforcement can be provided in two basic ways: segregation of an hard phase from molten metal or direct introduction into the metal matrix [24]. The reinforcement in the shape of particles is chosen because it provides more isotropic properties than the fiber reinforcement, and the final material is easier to manufacture [25]. Moreover the ceramic materials are selected due to their high hardness value, high melting temperature, good corrosion and creep resistance [26,27].

2.3 Utilized materials

The materials used in this work are 316L stainless steel and tungsten carbide (WC) both in the form of powder. These two different powders are mixed in the LC feeder and, through the cladding process, the MMC (Metal Matrix Composite) is cladded on a 316L substrate. The 316L stainless steel and the tungsten carbide are respectively matrix and reinforcement.

2.3.1 Stainless steel 316L

Stainless steels are widely used alloys in many fields such as construction, automotive and medical [28–30]. Indeed, it combines corrosion resistance with high toughness, good ductility, formability and high absorption of impact energy [31]. They exhibit really good corrosion resistance due to the high chromium content (10-14%) and they are characterized by an amount of carbon lower than 2% [28,32]. The high presence of chromium leads to the formation of an oxide layer that gains the corrosion resistance.

304 and 316 type are the stainless steels most largely utilized by the industries. These iron based alloys exhibit an austenitic matrix (FCC-face centered cubic), obtained by means of alloying austenitizing elements, such as Ni, Mn and N [33].

During the industrial evolution it has been possible to produce another version of these two materials. It consists of the decreasing of the carbon amount. This reduction avoids the formation of chromium carbides which result in a loss of chromium from the matrix and a loss in corrosion resistance (sensitization) [34]). They are differentiated by a L after the AISI classification numbers, e.g. AISI 304L. Therefore, the L alloys have weak wear resistance and it is a strong limitation for the applications. AISI 316 and 316L compositions provided by Altlas Steels are given in Table 2-2.

Table 2-2: Typical 316 and 316L chemical compositions [35]

Grade		C	Mn	Si	P	S	Cr	Mo	Ni	N
316	min.	-	-	-	-	-	16.0	2.00	10.0	-
	max.	0.08	2.0	0.75	0.045	0.030	18.0	3.00	14.0	0.10
316L	min.	-	-	-	-	-	16.0	2.00	10.0	-
	max.	0.030	2.0	0.75	0.045	0.030	18.0	3.00	14.0	0.10

2.3.2 Tungsten carbide (WC)

Carbides are the combination between carbon and a metal. The production of large size pure carbides is attractive to produce cutting tools because due to their high melting temperatures, great hardness, high chemical resistance. One of the most interesting carbide is the tungsten carbide. Wear-resistant parts made by tungsten carbide-cobalt (WC-Co) composite powder had a huge world market

production in the recent years [36]. The tungsten carbide exists in nature as Qusongite (WC). This mineral presents, besides tungsten and carbon, impurities of other elements as chromium [37].

The commercial tungsten carbide is mainly known as two compounds, WC and W_2C. They show many structural modifications in accordance with a certain range of temperatures and compositions, as shown in Figure 2-7 [38].
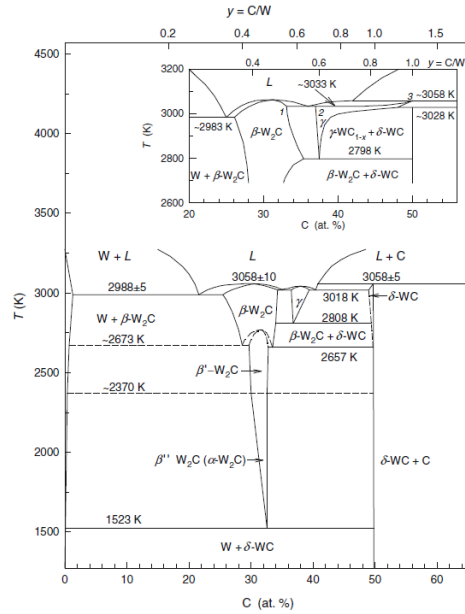
Figure 2-7: Phase diagram of the W-C system [38]

At lower C content the β-W_2C is stable and it has a hexagonal structure (hcp). A higher amount of C leads to the stability of the WC which has a hexagonal structure which is called δ-WC. Furthermore, the γ-WC1-x ranges between 38-50 % of C amount (% at.). It has a cubic structure and it is considered as a structural modification of the WC carbide.
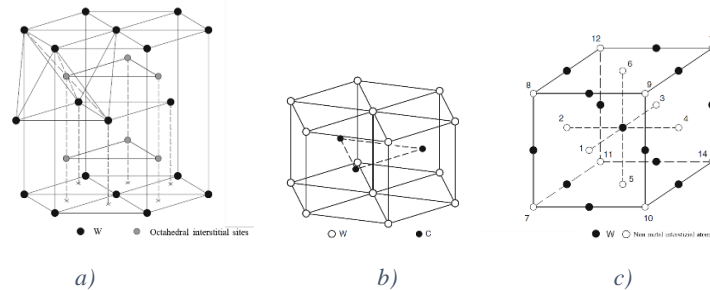
Figure 2-8: Crystallographic structures of the Tungsten carbides. a) Hexagonal structure of the β-WC carbide. The sites indicated with the ◎ are randomly occupied by carbon atoms with a probability of ½. b) Cubic structure (rock salt) of the γ-WC1-x carbide. d) Hexagonal structure of higher δ-WC carbide [38]

In Table 2-3 the principal properties of the Tungsten carbide are reported.

Table 2-3: General characteristics of the Tungsten carbide [39]

Density	15300 – 15900 kg/m^3
Young's modulus	600 – 670 GPa
Yeld strength (elastic limit)	373 – 530 MPa
Tensile strength	373 – 530 MPa
Elongation	0,06 – 0,09 %strain
Flexural strength (modulus of rupture)	510 – 820 MPa
Fracture toughness	7,4 – 9 MPa*m$^{1/2}$
Hardness Vickers	3100 – 3600 HV
Fatigue strength at 10^7	360 – 420 MPa
Melting Point	2820 – 2920 °C
Maximum service temperature	727 – 777 °C
Thermal conductivity	28 – 88 W/m*°C
Specific heat capacity	184 – 190 J/kg*°C
Thermal expansion coefficient	4,5 – 7,1 µstrain/°C
Latent heat of fusion	330 – 370 kJ/kg
Price	17,1 – 26,6 €/kg

2.4 Microstructure of 316L+WC

In the next paragraph, the microstructure of the laser cladded pure 316L stainless steel (1) and the phases formed by the addition of tungsten carbide (2) will be underlined. Finally, a list of the carbides present in the classical manufacturing processes is provided (3).

2.4.1 Microstructure of pure 316L by laser cladding

The laser processes are characterized by high temperatures and high cooling rates. These two features lead to a refined microstructure in comparison to the traditional fabrication methods. As a consequence, the mechanical properties are usually enhanced as well as said in section 2.1[6–8]. The complex thermal history of the material subjected to the Laser Cladding process was analysed by M.L. Griffith et al., showing the relative thermal cycle [40].
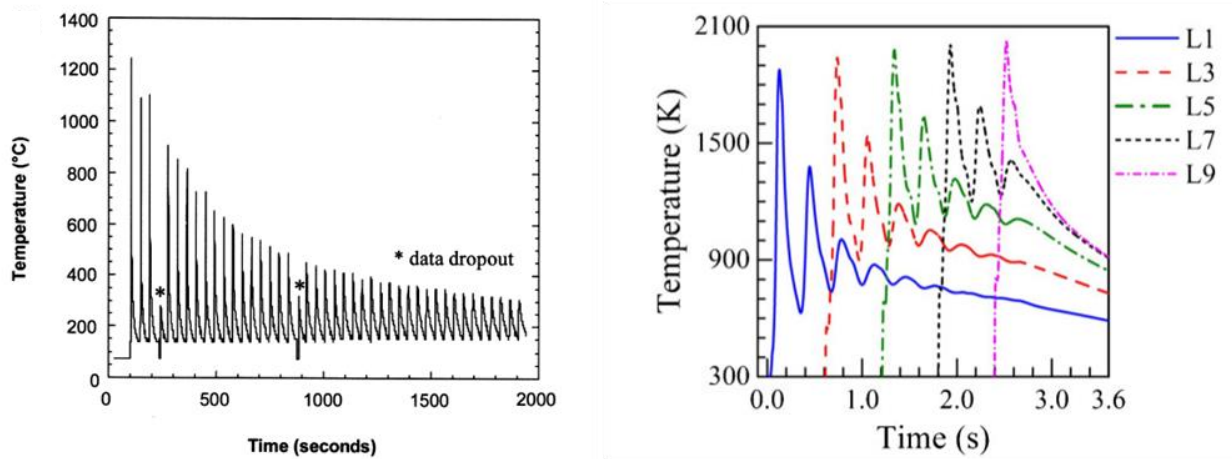
Figure 2-9: Thermal history of additive manufacturing processes [40,41]

Zhong Y. et al. [42] observed the particular "arc-shaped" microstructure of the cladded 316L. In that study, the presence of an intergranular cellular segregation network structure was noticed and that can be well seen in Figure 2-10. This hierarchical microstructure of the laser processed 316L leads to an enhancement of the yield strength in comparison to the 316L fabricated by traditional methods [42].

Moreover, it was observed from the XRD analysis that the solid sample processed through laser fabrication consist of pure austenite (FCC) [42].

a)   b)   c)
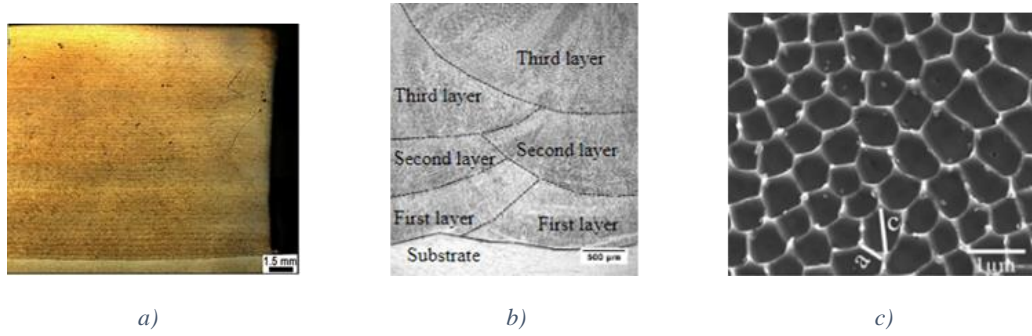
Figure 2-10: a) Lateral surface of a 316L stainless steel sample produced by LC; b) Cross section of a 308L stainless steel produced by LC; c) Intergranular cellular segregation network [42–44]

The solidification microstructure resulting from the LC is epitaxial and grains growth in the same direction of the heat flow [12]. The solidified layer continues the crystallization in accordance with the deposition of the previous layer [43]. The solidification starts from the edges of the melt pool and proceeds towards the center of the pool. The advance of the deposition leads a relatively lower cooling rate due to the heat accumulation from the previously deposed layers, thus leading to a grain coarsening. Furthermore, the stronger heat fluxes between the layer being deposited and the previously deposited layers lead to the formation of the heat affected zone (HAZ) and several reheated zones, but at different temperatures [45,46]. Those reheating modify the microstructure and the cell size.

a)   b)
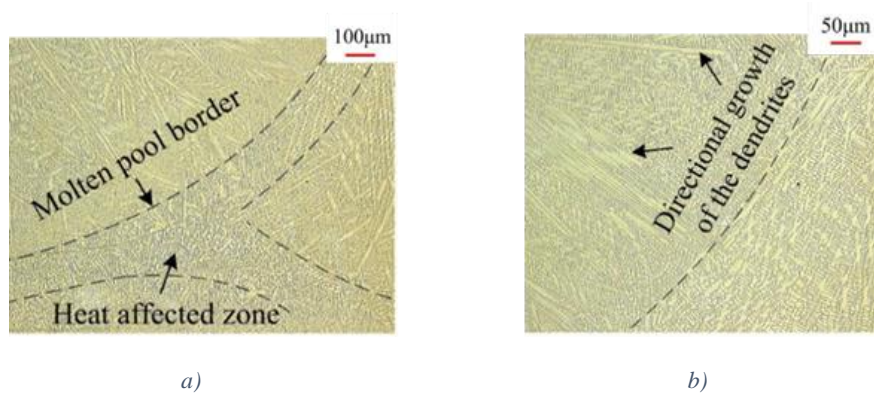
Figure 2-11: Micrographs of the laser processed stainless steel at 90° with the respect of the building direction. a) Different microstructure in the melt pool and in the Heat affected zone; b) Solidification microstructure inside the melt pool. [44]

The increase of the distance from the substrate leads to a coarsening of the microstructure due the heat accumulation from the previously deposited layers [40,47]. The coarser microstructure exhibits lower mechanical properties, as in the case of the microhardness of the deposit [46].
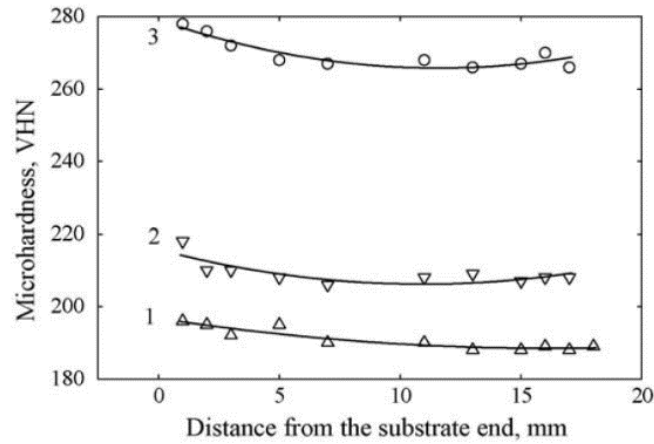
Figure 2-12: Microhardness evolution along the distance from the substrate using three different laser power [46].

2.4.2 Phases formed in the 316L austenitic stainless steel with the addition of Tungsten carbide

The metal matrix composites own exceptional mechanical properties due to their complex microstructure. The presence of hard carbides is a common way to create the wear resistant MMCs. In the classical manufacturing processes three main type of carbides have been distinguished depending on the moment of their solidification:

1. Primary carbides, formed directly from the liquid phase;
2. Eutectic carbides, formed again from the liquid but together with the matrix at the last stage of solidification;
3. Secondary carbides, precipitated at solid state [17].

They will be briefly described in the subchapter 2.4.3 with some examples. Those carbides are being considered as a reference considering the lattice structure and the composition, even if in the AM processes the different cooling rates lead to new carbides morphologies and compositions.

The addition of the tungsten carbides during the fabrication by LC changes the chemical composition of the 316L stainless steel. Indeed, a percentage of every carbide is dissolved by the contact between the original WC powders and the liquid metal, enriching the composition of the original 316L. This phenomenon leads to the solidification of a new metal matrix composite (MMC), around partially dissolved WC. In addition to the classical solidification from the melt pool sides, during the track solidification the remaining and partially dissolved WC act as nuclei for the solidification [17].

16
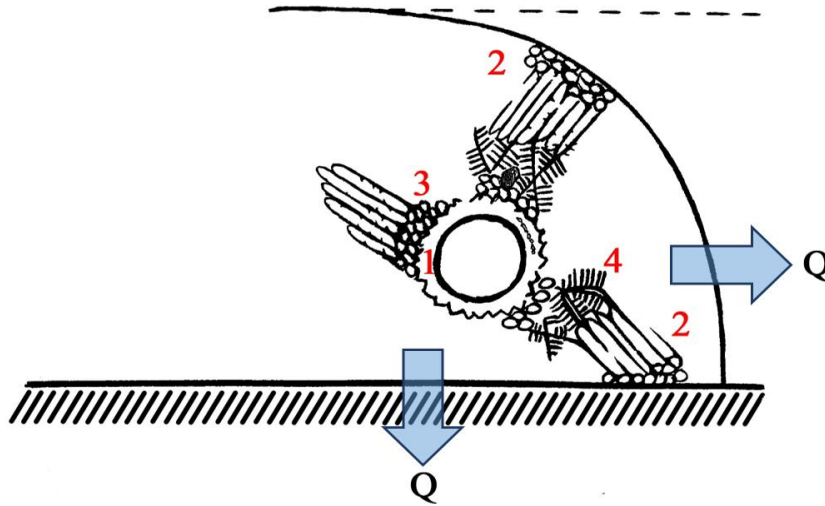
Figure 2-13: Schematic representation of the 316L+WC solidification [17].

The microstructural characterization of this material is part of the Tommaso Maurizi Enrici's PhD thesis and it is described in his work. The carbides formed in this complex microstructure depends on the position in the track and on the distance from the WC carbides. In the track the microstructure is composed of austenite and a complex regular eutectic carbides, meanwhile in the HAZ it is composed by austenite, $M_{23}C_6$ and M_6C eutectic carbides. The solidification from the WC carbides leads to the formation of slightly larger and purer $M_{23}C_6$ and M_6C eutectic carbides due to the particularly high concentration of W around the reinforcements.

2.4.3 Carbides in classical manufacturing processes

Now a brief description of the carbides morphologies is given:

MC: Three different types of MC eutectic are noticed:
- Divorced that occurs as isolated massive crystals;
- Irregular that is poorly coupled eutectic and has a "petallike" morphology;
- Complex-regular that is coupled eutectic and has a branched "petallike" morphology.

The MC carbide exhibits a FCC structure and a hardness of 3000HV [48].
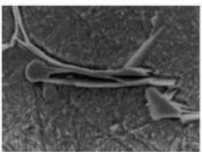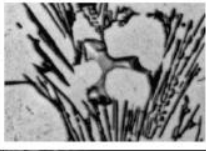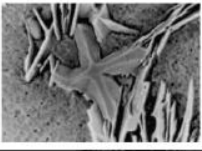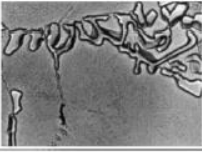
Optical	SEM	Carbide morphology	Eutectic classification
MC		Idiomorphic	Divorced
		Petallike	Irregular
		Branched petallike	Complex regular

Figure 2-14: Different types of MC eutectic [48].

M₂C: The chemical composition and the cooling rate influence the eutectic M_2C morphology. There two types of M_2C: irregular and complex regular. The crystalline structure of both is hexagonal and their hardness is between ~1580-2500 HV [48].
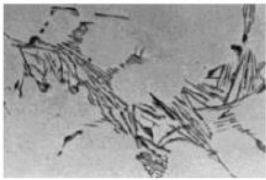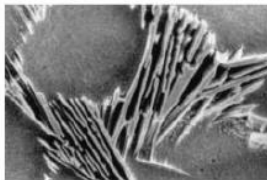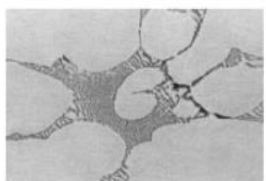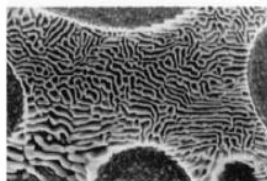
Optical	SEM	Boccalini[45]
		Irregular
		Complex regular

Figure 2-15: Different types of M2C eutectic [48]

M₆C: Characterized by a central platelet of M_6C carbide, from which secondary platelets arise. The platelets are separated by austenite (γ). Faster cooling rates lead to the decrease of the distance between the platelets. W, Mo, V, Cr and also Fe are M6C formers. The crystalline structure is FCC and it has a hardness of ~1500HV [48].

d)   *e)*
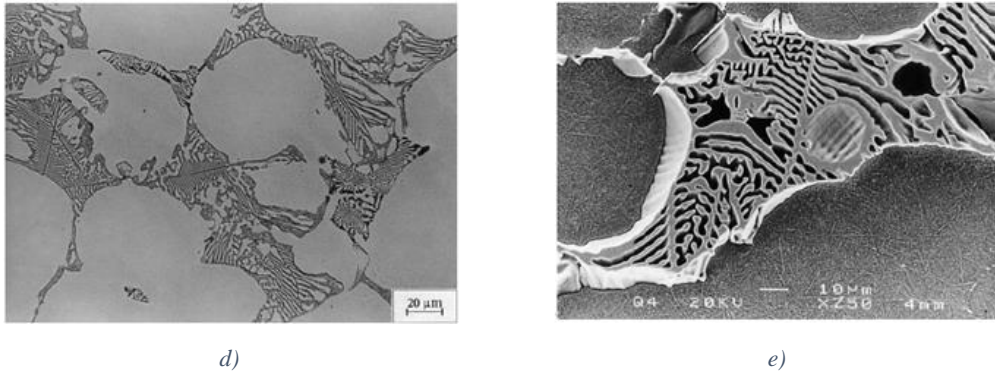
Figure 2-16: Morphology of M6C eutectic. a) Optical microscope image; b) SEM image [48].

M₇C₃: The morphology of this carbide is mostly hexagonal and rod-like. The formation of this carbide is led by rapid solidification and high amount of Chromium.
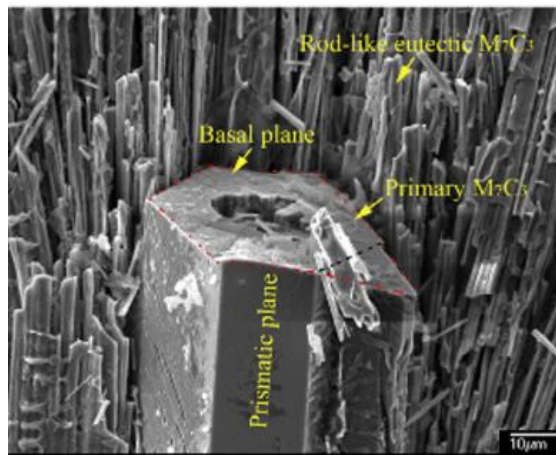
Figure 2-17: SEM image of the morphology of M7C3 in chromium cast iron [49].

M₂₃C₆: In stainless steels, it is mainly a secondary carbide and it provokes sensitization. Indeed, the sensitization is primarily caused by the chromium depletion that takes place during the formation of $M_{23}C_6$ [50]. This process causes a lower corrosion resistance [33].
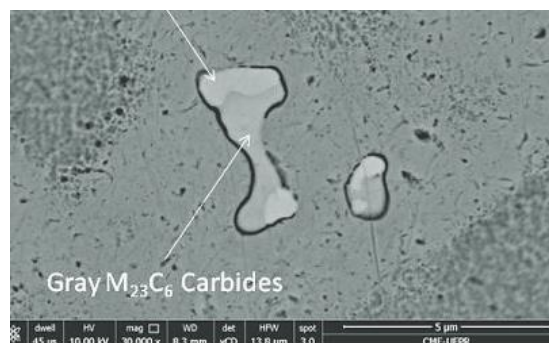
Figure 2-18: SEM image of a M23C6 in Nickel-based C276 alloy coating [51].

19

2.5   Tribology review

As mentioned in section 2.2, technological evolutions in engineering sectors acted in this age. More complex challenges need to be met by production systems and finished products. Robustness, quality and performance rise as consequence of the technology's advancement. This advancement induces that the products and the systems to manufacture them must work in extreme conditions. Thus, the parts are subjected to high thermal and mechanical dynamic loads. Corrosion environments and high temperatures are very critical for i.e. metal forming or aerospace sectors. A temperature working range between 500°C and 1000°C can be achieved and it can cause a reduction of the mechanical properties of the material and a modification in its surface. The change in surface influences the production. The quality of the finished product decreases. The replacement of the damaged piece is required. This leads to the increase in the production cost. Friction, wear and lubrication characteristics of materials are involved, and they need to be studied to avoid the problems that might take place during the production [52]. Many researches had been conducted in order to protect the objects.

2.5.1 Common techniques and materials to improve of the surface properties

Conventionally, one efficient method to protect the mechanical parts from surface damaging, is to apply thin wear resistant coating [52]. The improvement in corrosion and wear resistance can be achieved also by laser surface modification that provides a finer and more homogenous microstructure, and/or the formation of new alloys on the surface [7]. The classical used techniques used to deposit the wear resistant layer are the chemical vapor deposition (CVD), plasma assisted physical vapor deposition (PA-PVD) and pulsed laser deposition [53].

In the last years, the laser-based additive manufacturing (LBAM) has revolutionized the sector of the surface protection. The laser melting deposition (LMD), especially, is a very good option for industrial applications. T. Schopphoven et al. [54] noticed in his study that the thermal spraying exhibits poor mechanical bonding with the substrate, in the contrary of LMD.

Many different potential coatings materials had been studied; like different alloys, steels and metal matrix composites (MMCs). Usually the processing of the wear resistant materials is costly and difficult. Thus, in most of the cases, the laser deposition of these alloys is made on low alloy steel that act as substrate and they are cheaper. Hence, the solubility, the affinity, the thermal and mechanical stress, need to be considered, since they could be generated during the deposition and the consequential cooling of the deposit.

M. Pellizzari et al. [55,56] reports that the high-speed steel is the most versatile material for the metal forming processes thanks to the great mechanical properties that do not change too much even at high temperatures. The materials tested by his group are high speed steels and cast irons with different composition that are characterized by a tempered martensitic matrix surrounded by an interconnected network of primary and eutectic carbides (MC and M_7C_3).

H. Torres et al [57] performed high temperature sliding tests in order to find a substitution for the high strip mill steel. The wear behavior of low alloyed structural steel, gray cast iron, martensitic grade iron and Fe-Cr-V hard facing material were studied. The Fe-Cr-V, that was deposited by LMD, showed the lower wear among the material investigated. The better wear resistance was attributed to the retention of high hardness at high temperatures.

S. Lester et al. [58] evaluated the wear through tests conducted on LMD WC reinforced roll steel and high carbon alloy cast iron roll steel. The experiments were conducted by sliding tribological machine at room and at high temperature. The LMD WC reinforced roll steel shows a better wear resistance than the cast alloy.

A. D'Oliveira et al. [59] made a comparison between the plasma transferred arc (PTA) and LMD Stellite 6 (Co-Cr-W-C) on a stainless steel (AISI 304) substrate. In this study, the material processed by two different techniques was thermal treated at a temperature above the 1000°C and the hardness was tested. It was shown that the LMD met a significantly drop. This result suggests that for LMD Stellite 6 it is needed to be post-heat treated or the PTA has to be chosen in order to maintain a stable wear behavior.

Y. Yang et al. [60] focus their work on the production of globular Ni- based alloy precursor reinforced with WC. Other studies had been conducted on Ni alloys. L. da S. Ferreira et al. [51] investigated the role of the substrate in the PTA Ni- based C276 alloy coating deposition. K. Van Acker et al. [61] noticed that the influence on the wear of the size and distribution of WC reinforcement in laser clad WC/Ni depends on the wear test performed.

CoMoCrSi alloys, called triballoy are materials that exhibit excellent wear resistance. In these compounds the great strength, and in general the mechanical properties, come from the alloying elements like Mo and Si. Indeed they promote the formation of a particular microstructure that is very hard [62]. Studies on this material were conducted also by others C. Navas et al. [63] and M.J. Tobar et al. [64].

M. H. Staia et al. [65] made a study of the wear resistance of laser alloyed A-356 aluminum alloy/WC composite in which the substrate is the un-reinforced A-356 alloy. The tests were conducted to compare the influence of different laser traversing velocities in order to find the optimum processing conditions. The A-356/WC and the substrate were examined. The research

shows that there is not a beneficial effect to incorporated WC in the base alloy. It is also reported that studies performed with a different counterpart, show another wear behavior. Therefore, it is important to take in account the effect of the contact between the aluminum alloy and the counterpart.

D. Gu et al. [66] produce a nanocrystalline TiC reinforced Ti matrix bulk-form nanocomposites using Selective Laser Melting (SLM) technique. They observed the microstructure resulting, making varying the "volumetric energy density". Moreover, the mechanical properties were analyzed. Concerning the wear, they attributed the relative low friction coefficient and wear rate to the formation of a tribolayer on the worn surface.

AISI 304 stainless steel and metal matrix composites (MMCs) are reported to be produced by hot-isostatic pressing. In the S. Tjong et al. [22] work the MMCs are produced with varying amount of TiB_2 particles, that act as reinforcement. These particles enhance the wear resistance of the SS304. This improvement is given by the greater hardness of the TiB_2 in comparison with the counterpart used for the wear test. Electronic microscope observations reveal that the hard-ceramic particles are situated close to the top surface of the specimen providing the protective effect.

The use of solid lubricant materials is another used technique to increase the wear performance of materials [67]. It can happen that the material acting as lubricant is not homogenously distributed [68]. The LBAM overcame this problem because it ensures homogenization by tailoring the processing parameters. A lot of solid lubricants can be mixed in form of powder like Ag [69].

2.5.2 Wear studying methods

As shown in the previous section, many materials were tested to wear. Nevertheless, the tests were performed using different types of apparatus in order to try to recreate the working condition that specific material must sustain. Following, some of the most diffuse machines are briefly described:

Ball-on-disk/ Pin-on-disk: It is the most commonly used test machine. Many configurations exist. The classical version consists by the specimen that acts as the disk, which turns under a fixed ball. The ball is pressed on the disk by a certain load. Many materials may be used as ball like WC, SiC, Al_2O_3 and steels. In general, the counter body material is chosen if it is supposed to have a better wear behavior in comparison to the test material.

L.J. Yang et al. [70] utilized a different configuration of the Pin-on-disk machine. They used as a pin the material that they wanted to test, and three different disks of different materials are utilized.
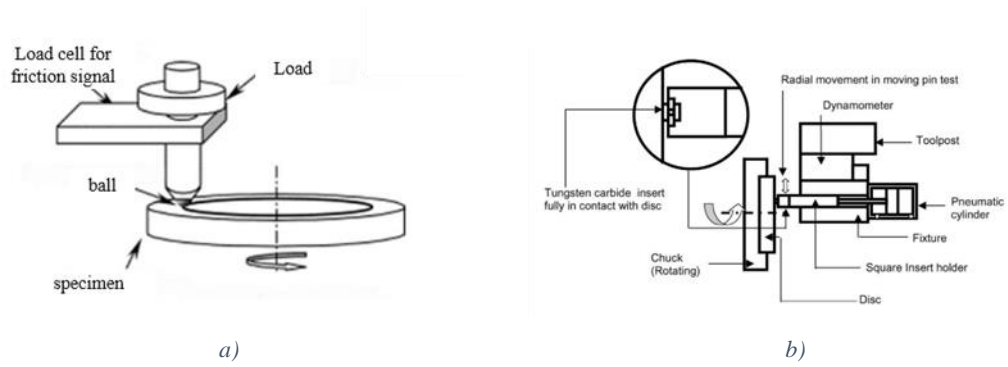
Figure 2-19: a) Schematic illustration of classic Pin-on-disk tester [63].b) Schematic illustration of the "reverse" Pin-on-disk tester [70].

Cameron-Plint machine [71,72]***:*** In this test a disc, the material that is being evaluated, run against a crowned profile. Moreover, it is possible to modify the machine by providing heat in order to perform high temperature tests.
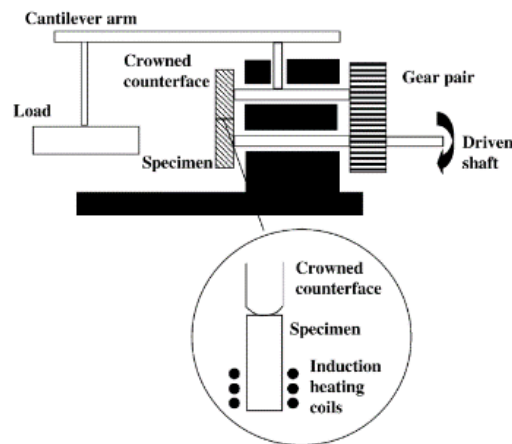
Figure 2-20: Schematic illustration of the Cameron-Plint tester [72].

Block-on-ring [73]***:*** The blocks are made with the material that needs to be tested. They are pressed under a specific load against a ring. The ring is rotating, and the wear is evaluated after tot meters in dry conditions.
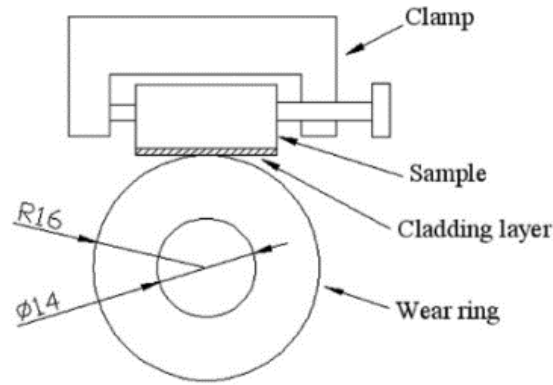
Figure 2-21: Schematic illustration of the Block-on-ring tester [73].

Ball-cratering [61,74]*:* L.M. Vilhena et al. utilized the apparatus illustrated in Figure 2-22. It consists of a bearing steel ball directly connected to the driven shaft of a variable speed motor that is rotating against the specimens. Moreover, SiC abrasive particles were used as abrasive slurry. This slurry is stirred continuously and fed at the interface between the ball and the samples.
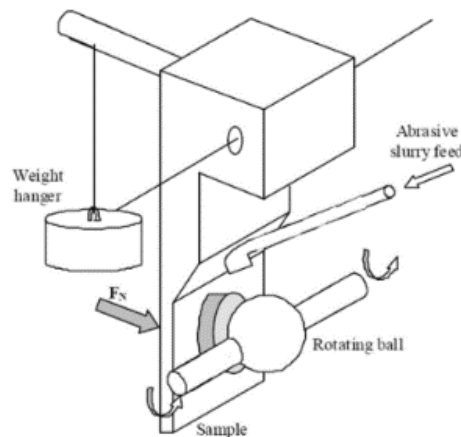
Figure 2-22: Schematic illustration of the Ball-cratering [74].

Reciprocating friction [75]*:* In this test the ball is pressed under a certain load applied against the surface of the specimen. The reciprocating motion causes the wear.
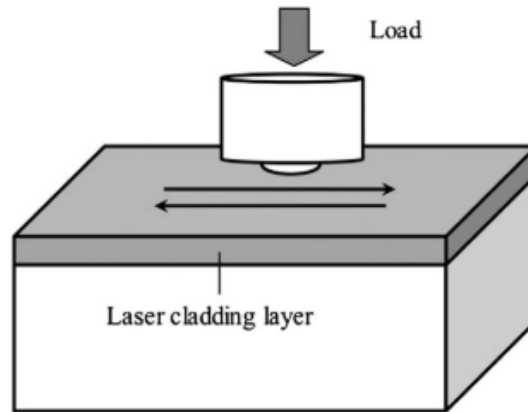
Figure 2-23: Schematic illustration of the Ball-cratering [75].

Rolling-sliding testing [76,77]***:*** This configuration test is actually a variant of the Cameron-Plint machine. It consists in two rollers disposed as in Figure 2-24. They are connected to a DC motor that allows the rotation.
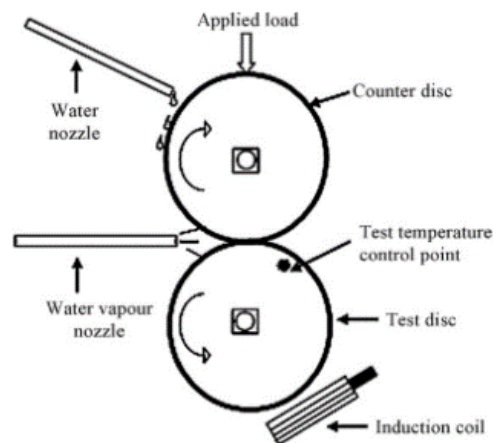
Figure 2-24: Schematic illustration of the Ball-cratering [77].

Typically, the samples own many peaks and valleys even if the roughness is very low. The peaks are commonly referred as asperities. These asperities are the parts of the material that enter directly in contact with a second material put on the surface. Thus, the contact force is distributed among the contacting asperity areas. The resulting effect is a plastic deformation of the peaks. B. Bhushan [78] illustrates the concept of real surfaces in contact, reported in Figure 2-25. This concept is very important in the friction and wear behavior of materials [79] .
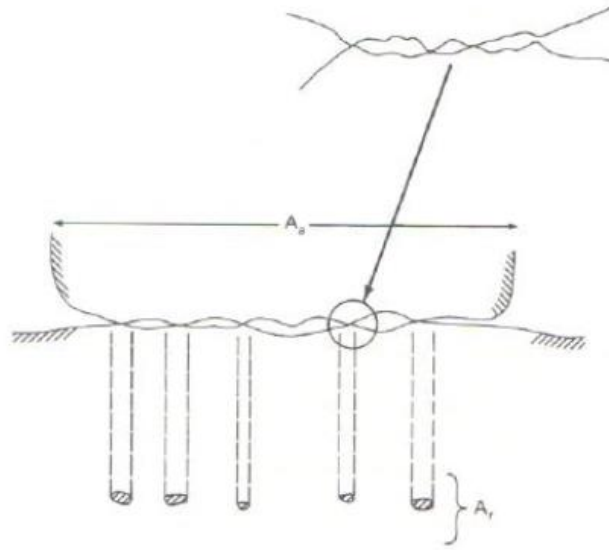
Figure 2-25: Area contact between two surfaces. Aa is the apparent area of contact and Ar is the real area of contact [78].

When two surfaces are in contact and they slide against each other, they generate a frictional force and heat is generated by work dissipation. Thus, it is important to define the Coefficient of friction. It is the ratio of the frictional force to the applied normal force at the interface of the two sliding surfaces [78]. The friction force is considered to be perpendicular to the direction of the applied load and parallel to the direction of sliding. As the friction increases, the maximum shear stress moves closer to the sliding interface. When the coefficient of friction becomes 0.3, the maximum shear stress will be at the interface plane of the sliding surfaces. The first plastic yield will be located at that interface [80].

At least one of the sliding surfaces in contact will experience wear. In order to describe the wear due to the sliding of two surfaces, Archard simple theoretical equation can be used. Archard relates the volume of material lost by wear to the total distance of sliding, the applied load, the contacting area, and the hardness of the softer material of the pair. The theory is showed by the following equation: $Q = KW/H$. Q is the material volume worn away per unit sliding distance (mm^3/m), K is a constant called "Archard wear coefficient", W is the normal load applied to the contacting interface (N), and H is the hardness of the softer material (Pa). Archard wear equation does not describe a sharp transition in wear once a certain load is reached. Whereby several more complex model have been developed in order to try to obtain a more complete model of sliding wear that consider multiply wear mechanisms [81].

2.5.3 Wear types

In the following, the different wear types that occur in extreme conditions and leading friction, are briefly described.

Adhesive Wear

Adhesion occurs when two solids are in contact and the relative surfaces are completely free of contaminations. Passive films, oxidation, lubricants and adsorbed gases reduce the adhesion between the two surfaces. This decreasing is due to the creation of a shield provided by these contaminations that decreases the real contact area. The adhesive mechanism is the electron transfer between the two materials and consequentially formation of adhesive bonds [82].
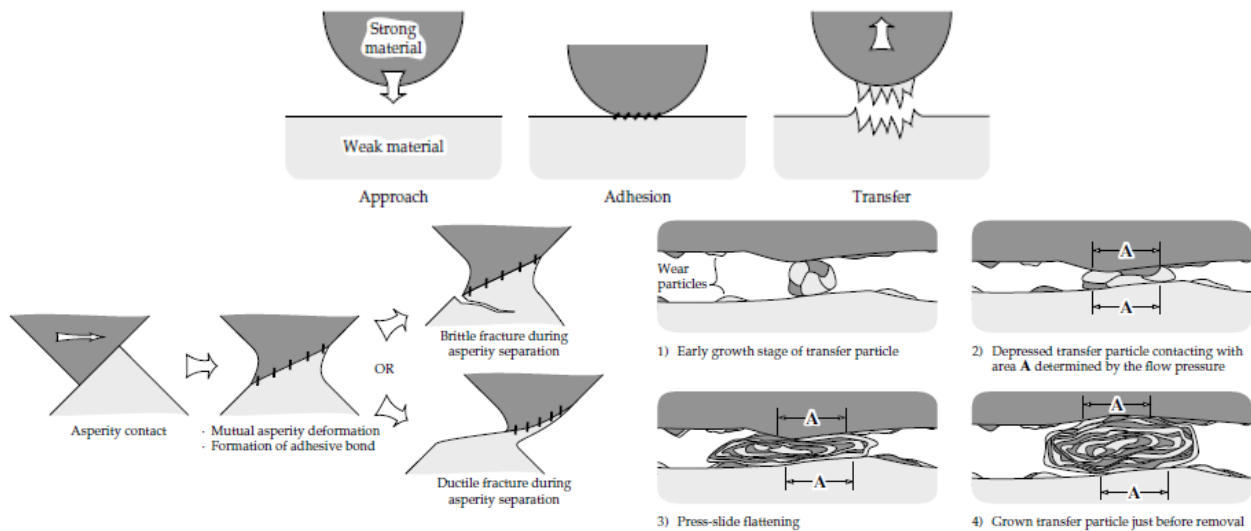
Figure 2-26 Schematic illustration of the adhesive wear process. Bond formation, alternative model for the adhesive contact, possible mechanism of wear debris formation due to adhesive wear [82].

Adhesion between ceramic and metallic materials may occur, particularly for oxygen-rich ceramics, such as alumina. Adhesive bonding between the oxygen atoms of the alumina and metallic surfaces may occur, usually resulting in transfer of the metallic material to the ceramic interface [82].

G. W. Stachowiak [82] proposes a general adhesive mechanism explanation. Firstly, the sliding starts, and the friction is low due to the surface contamination. The friction continuously increases depending on the time that the surface contamination is removed from the contact interface. Once the contamination is completely eliminated, adhesion will occur leading a high friction provided force, without oxidation. After the adhesive contact, fractures and consequent transfers of the weaker material to the stronger material may occur. This results in the formation of a layer or film. It can be

possible that the transferring of material is not the only mechanism that occurs. Indeed, asperities fracture may occur by fragile fracture of the weaker asperity, or strain to failure.

From this process, plate-like wear debris particles may form. At the beginning, the shape of these particles is spherical. If the particles grow, they may become flat thought plastic deformation. Adhesive processes continue to grow till the transferred particle reaches a critical thickness and the two-contact surface detaches.

Oxidative wear

This mechanism is referred to as a formation of an oxide film on the sliding metallic surface. In order to observe this phenomenon, an environment which favorites oxidation is required, i.e. in contact with air. The oxide layer formation begins with the direct contact of the sliding surface. Once the oxide layer reaches a critical thickness, the direct contact is reduced or eliminated. Thus, the shear strength is reduced too by the lower adhesive forces. In dry sliding conditions the maximus applied shear strength is at the interface of the sliding material. If the oxide layer reduced the interfacial shear stress, this is traduced in a consequently reducing wear.

The oxidative wear is a thermally driven process, so the rate of oxide film growth can be described by Arrhenius relationship:

$$k = Aexp(-\frac{Q}{RT}) \, .$$

k is the rate constant for tribochemically induced oxide film growth, Q is the activation energy, R is the universal gas constant, and T is the interface temperature [81].

It can be seen from this model that every phenomenon that increases the temperature will result to increase the oxide growth. Indeed, frictional heating and/or increased ambient environment temperature can raise the rate of the oxide layer growth. The rate at which the tribochemical oxidation occurs depends on the difference in material properties. This difference affects the diffusion near the surface under sliding conditions. Moreover, the sliding conditions are altered by defects, stress, and deformation leading a possible acceleration of the oxide growing.
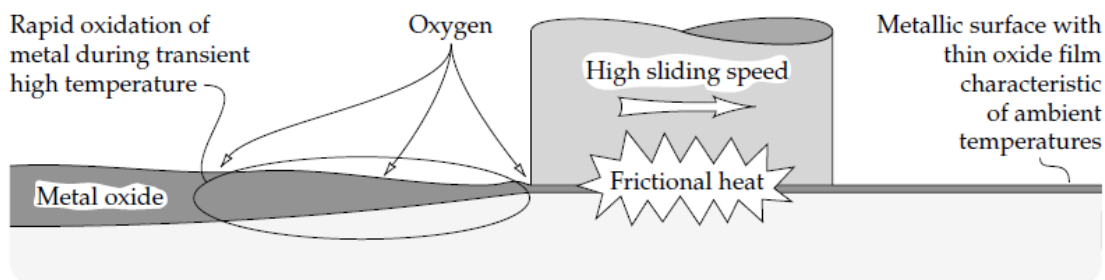
Figure 2-27: Schematic illustration of the oxidative wear process [82].

Oxidative wear can take place at high speeds when a high level of frictional heating occurs, and also at low sliding speeds when the contacting force is sufficiently low.

At high sliding speeds, a severe wear occurs, and it eliminates the native oxide film. Afterwards, there is a period of mild wear and re-growth of the oxide layer. Frictional heating could be so high that thick oxide films are rapidly generated. Since only sliding surface asperities experience this frictional heating, oxide grows preferentially at contacting asperities. The oxide run out when it reaches a critical thickness. Indeed, it cannot stand anymore the frictional shear stresses or the applied load. At sufficiently high sliding speeds, oxidative wear can become detrimental if significant material loss occurs through the repetitive growth and removal of oxide layers.
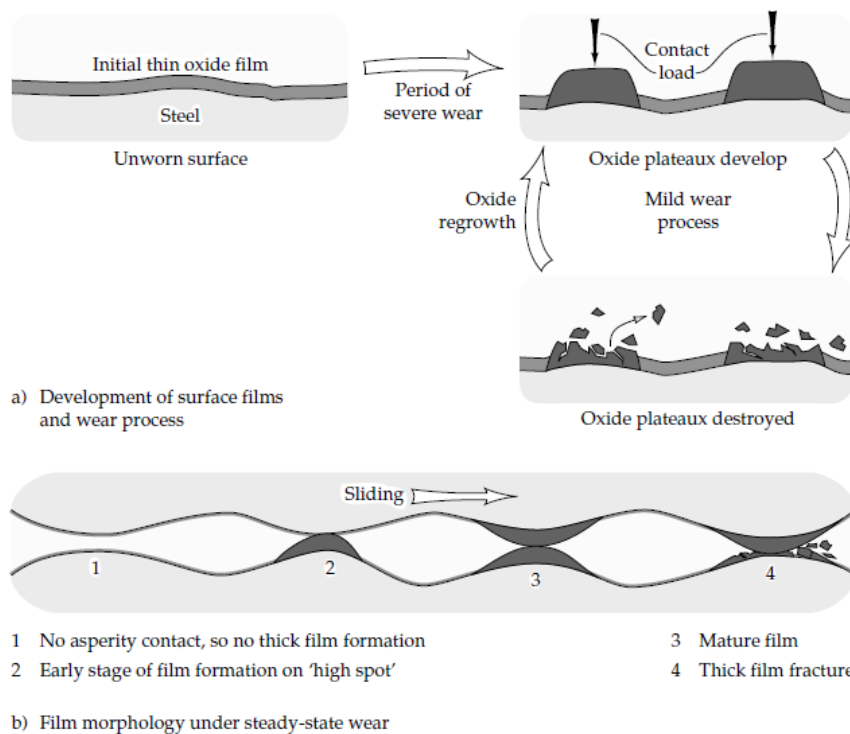
Figure 2-28: Schematic illustration of the oxidative wear process at high sliding speed [82].

The oxidative wear takes place by a different mechanism if under low sliding speed. In this case the heating is not sufficiently high, thus a thin oxide layer forms on the surface, but its growth is limited by slow diffusion. With the proceeding of the sliding, the thin layer fractures and the metallic wear debris oxidize while rolling between the sliding contacts. This leads to the formation of a compact layer of mixed wear debris. The mixed layer often reduces the friction and the wear.
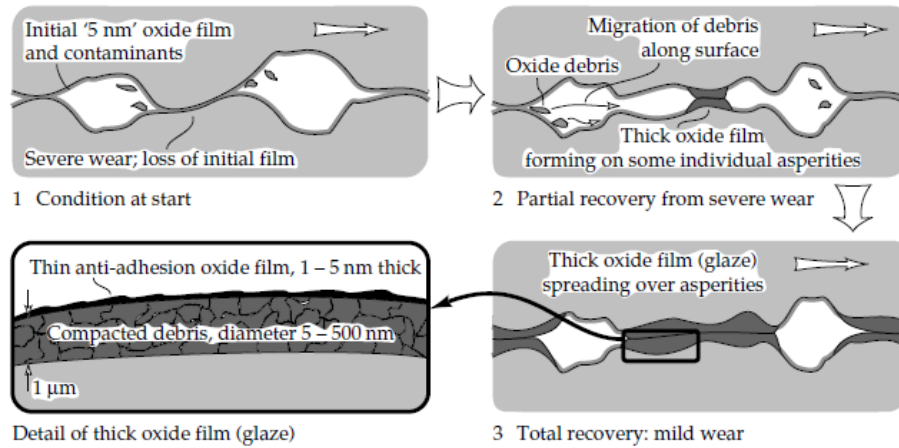
Figure 2-29: Schematic illustration of the oxidative wear process at slow sliding speed [82].

Moreover, M. Vardavoulias [83] studied the role of second phases of a heterogeneous microstructure of high-speed steels in the oxidational wear. He settled that an oxide layer of a-Fe_2O_3 forms by anion diffusion. It breaks up after reaching a critical thickness forming wear debris. The hard second-phase particles dispersed in the material play a significant role in the wear behavior. Their size is the most important parameter, which determines the possibility of the particles providing protection against oxidational wear of the matrix.
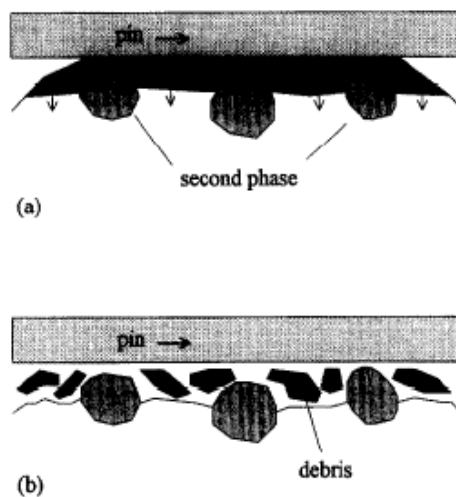
Figure 2-30: Oxidative wear in presence of second hard phase. a) Film formation; b) film break-down. [83].

Fatigue Wear and Delamination

During mild wear conditions, cycling contact stresses cause the fatigue wear. This results in cycling crack growth and failure of the regions near the surface. Several theories describe the details by which this process occurs during sliding of metals. The delamination wear is perhaps the most

recognized. A. Kapoor et al. [84] proposed a complete delamination wear model that takes in account the crack growth (Mode I - the opening mode in which the tensile stress is normal to the plane of the crack [85]) within heavily deformed plastic region. This model settles that delamination wear is a competitive fracture process between two different mechanisms: 1) low cycle fatigue (LCF); 2) ratcheting failure (RF). In the LCF the cyclic crack growth is drastically shortened due to high plastic deformation and high stresses. In the RF the strain accumulation due to plastic deformation from cyclic stresses, growing until a critical threshold. When this threshold is reached, ductile failure happens by exceeding the strain to failure limit. A. Kapoor addresses that the LCF and RF processes occur independently, but simultaneously. They occur under tribological contact until the critical level of crack growth or strain accumulation is reached, causing the fracture of the surface.

A. Kapoor considers the surface region of the sliding contact made of several layers. The strain accumulation occurs in each layer during cyclic stressing if the applied shear stress exceeds the effective shear strength of the material within the layer. When strain accumulation and/or crack growth reach a critical level, the closest layer to the surface of the material will pull out due to delamination. Hence the next layer is exposed, and the process is cyclically repeated, causing subsurface layers to move towards the surface [84].
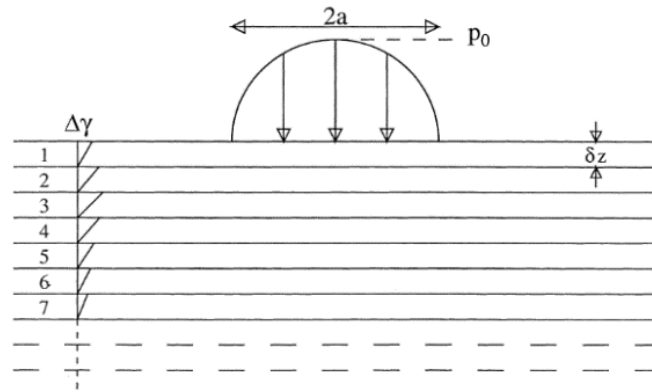
Figure 2-31: Schematic illustration of the layers of strain accumulation in the delamination wear. Δγ is the strain accumulation increment, δz is the thickness of each tribolayer, a is the radius of circular contact area for sliding contact of a sphere on a flat surface, p₀ is the Hertzian contact pressure [84].

Abrasive wear

This mechanism concerns the sliding or rolling of hard particles on the surface of a softer material. Hard particles cause deformation and result in wear when moving in contact with the surface of a softer material. This is abrasive wear and it can be produced by several mechanisms like: cutting, ploughing, grain pull out, fatigue, and brittle fracture. A common example is during cutting, where a

hard particle is embedded in the softer material and it is dragged causing plastic deformation. Ploughing is a similar phenomenon as shown in Figure 2-32, but plastic displacement of material occurs around the abrasive edges. At the same time, some material is built up in front of the particle.

Grain pull out is a relatively rare form of wear. It is more common in ceramics, but it may occur also in metallic materials if brittle phases form at the grain boundaries.
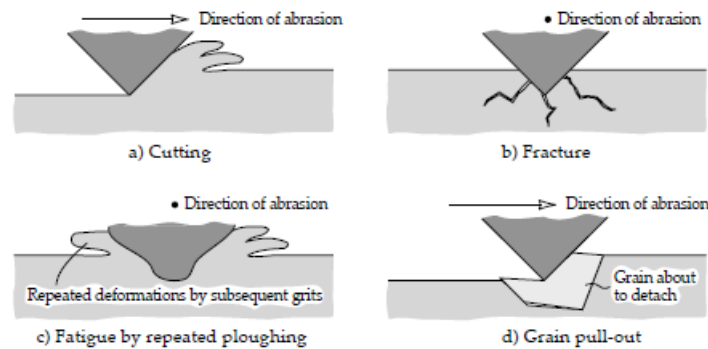
Figure 2-32: Schematic of mechanisms of abrasive wear [82].

Abrasive wear may occur by two-body or three-body abrasion. During wear, the grains could be fixed in a rigid setting and they are sliding against a softer material. This is the two-body abrasion. Unlike, the three-body abrasive wear refers to hard particles that are freely moving between the two sliding surfaces. The particles of wear debris may be generated by the sliding of hard materials, causing the three-body abrasive wear.
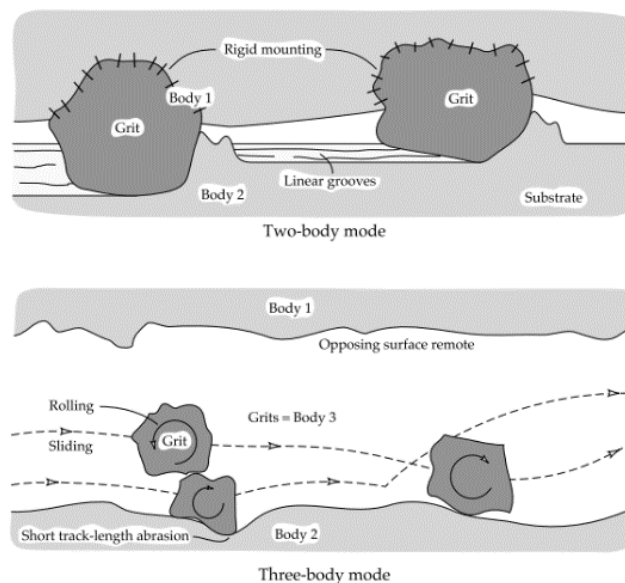
Figure 2-33: Schematic of mechanisms of abrasive wear in the two-body and three-body configuration [82].

3.   *Experimental methods*

The samples used for this work are showed in Figure 3-1 and the relative characteristics are resumed in Table 3-1.

They had been produced utilizing the Laser Cladding technique (LC), starting from two different types of powders (1-2). One of these samples (W20.24) was utilized for the microstructural characterization (3), while the others were used for the wear tests (5). After the wear tests, profilometer observations were carried out on the post-mortem samples (6).
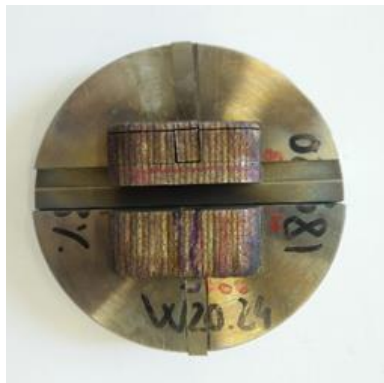
a)
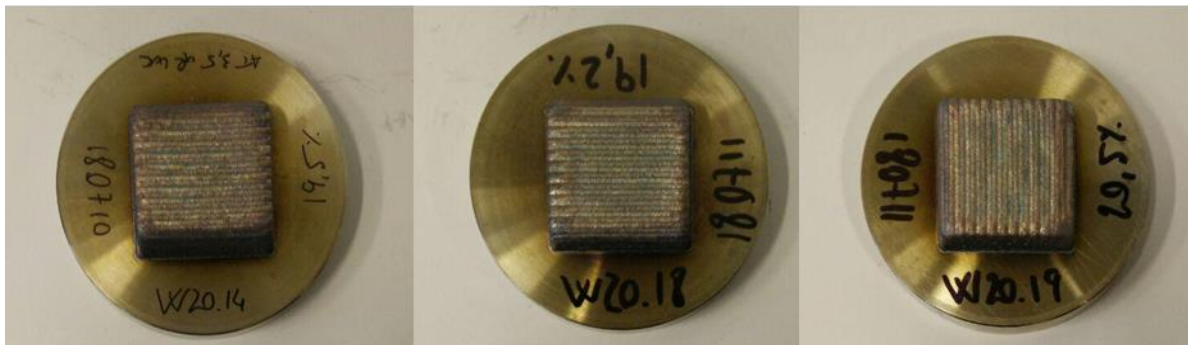
| *b)* | *c)* | *d)* |

Figure 3-1: Samples used in this work. a) sample for the microstructural characterization; b), c), d) samples for the wear tests.

The deposits have a parallelepiped shape. The base is a square with sides of 35mm. The height is close to 15mm. This variation is due to a punctual unstable material feeding of the LC machine. The samples were produced in order to have a composition of 20% of WC with a max tolerance of $\pm 2\%$.

33

Table 3-1: General characteristics of the samples.

Name	316L [g/min]	WC [g/min]	Total weight feed [g/min]	Volumetric percentage of WC in SS316L	Height [mm]
W20.14	15.2	7.6	22.8	19.5	14.6
W20.18	14.9	7.3	22.2	19.2	14.6
W20.19	14.8	7.9	22.7	20.5	14.5
W20.24	16	7.3	23.3	18	15

3.1 Powders

The powders used to create the samples in the Metal Matrix Composite coating SS316L+WC are SS316L powder and WC powder. They were provided by Höganäs [86], a Swedish company. In the Table 3-2 and Table 3-3 the chemical compositions of the powders are shown:

Table 3-2: Chemical composition of the SS316L powder (item name 316L-5520) (Annex 10.1)

%wt	C	Fe	Mo	Ni	Cr	Mn	Si
	<0.03	Bal.	2,0-3,0	10,0-14,0	16,0-18,0	1,0-2,0	<1,0

Table 3-3: Chemical composition of the WC powder (item name "4590") (Annex 10.2)..

%wt	C	Fe	W
	3,5-4,0	<0,5	Bal.

The particles size in the SS316L powder varies from 45 to 150 µm while for the WC powder it varies from 45 to 180 µm. The particles must be small but not too much otherwise they could create clusters, agglomerates and great local pressures on the pipes. Moreover, they cannot be too big otherwise they will cause obstructions in the pipes. In addition, the particles have a well-rounded shape. Indeed, that shape is required in order to avoid the possibility of damaging of the pipes and the nozzle of the LC machine. Abrasion can occur when the particles have irregular edge-shape.

3.2 Samples fabrication

The samples are produced by Sirris [1]. The machine used for the fabrication of the samples is a Cladding machine DUOCLAD VI LF 2000 shown in   *a)*   *b)*

Figure 3-2.

a)   b)
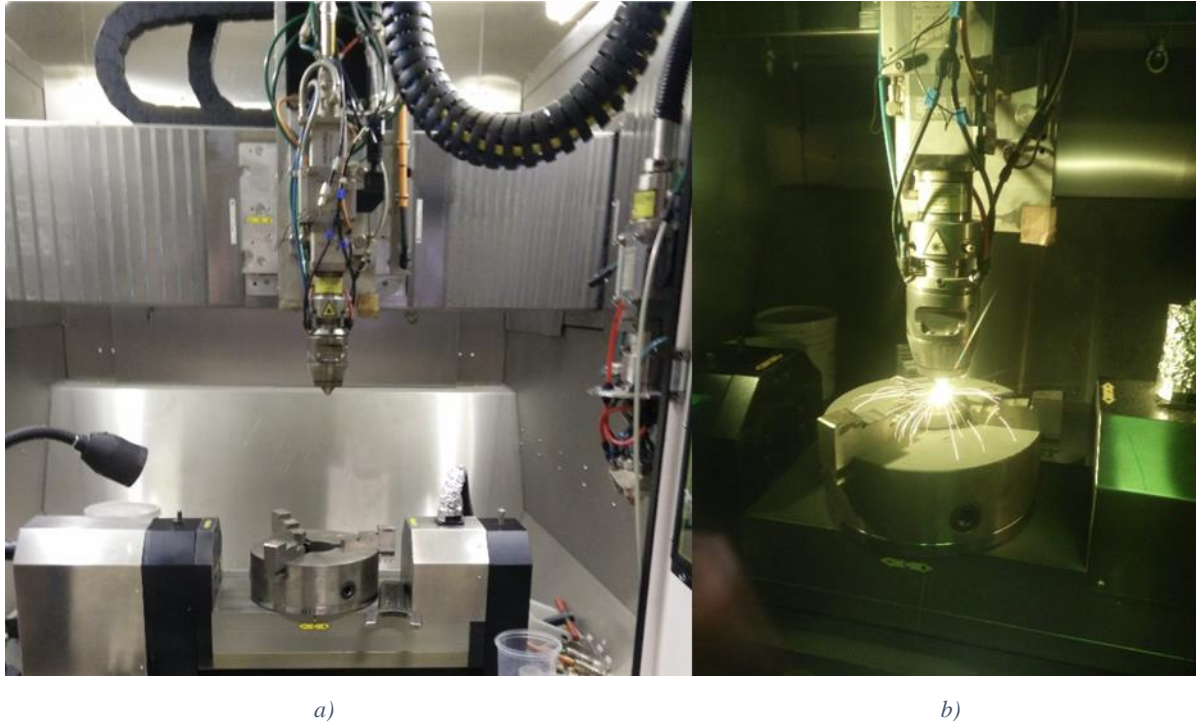
Figure 3-2: a) Internal view of the Cladding machine; b) DUOCLAD VI LF 2000 while it is working.

The powder is stored in a dispenser that has two cylinders giving the possibility to use two different types of powder. The continuous feed is provided by a turntable. The tuning of the speed of this object allows to decide the volumetric quantity of powder (cm^3/min) or, using the bulk density of the powder, the weight feed rate of powder (g/min). The two materials powders are mixed in the pipes and they are projected through a nozzle in a coaxial position. The nozzle and the laser are controlled digitally. The transport of the powder is provided by a gas. Argon is the utilized gas and it has also the additional functions of protecting the deposit from the oxidation during the production. Another function of the gas is the shaping of the powder flux. The energy source is a solid-state fibers laser.

The production of the sample that had been tested is not part of this work thus more details and the explanation of the parameters of the LC process can be found in the Elena Mancini's Master thesis [16]. An important difference respect that previous work is the deposition strategy. Indeed, in this work the bi-directional deposition strategy was chosen, instead for the raster one.
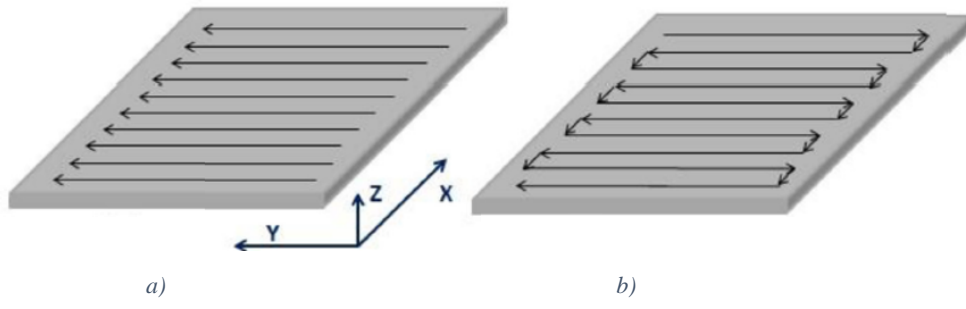
Figure 3-3: a) Raster strategy deposition; b) bi-directional strategy deposition.

3.3 Microstructural characterization

One sample was utilized for the microstructural characterization. The sample was cut with a Spark Erosion machine, and different sections of the deposit were obtained, in order to have an overall idea about the microstructure of the SS316L+ 20%WC.
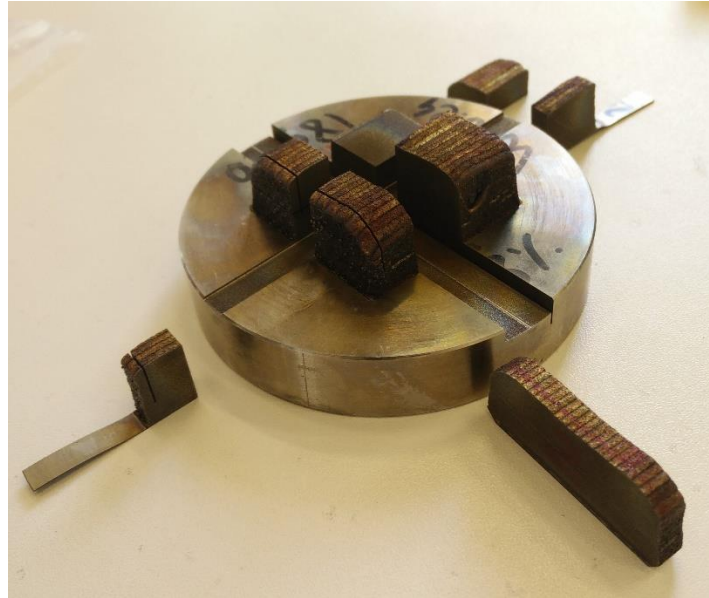
Figure 3-4: W20.24 after cutting process

The choice to cut this specific sample was due to a little defect present on the side of the deposit. Indeed, it can happen that the overlapping of the different tracks is not perfect and this imperfect overlapping causes that particular defect. In any case, it is a very rare scenario. The sample was cut using an electrical discharger machine. Three sections were considered and examined. An additional one was obtained, and it was sent to vibrometer preparation by PRESI. The samples needed a preliminary preparation in order to make easier the observations at the optical and electron microscope. Firstly, they were embedded in a Bakelite cylinder using a STRUERS Citopress-1. The Bakelite cylinder is obtained by pressing at high temperature the Bakelite powder, which then allows the polymerization. After that, the samples surface in the Bakelite was polished using a STRUERS Tegramin-30. This latest process is required to obtain a clean and plane surface. Indeed, a plane surface is necessary for the microscope analysis. The STRUERS Tergamin-30 owns a disc of 300mm of diameter. The polishing process consists in circular movements of the samples on a wear paper using also lubricant liquid. There are many wear papers in the market with different grain size, and the relative liquids needed [87].

a)   *b)*

Figure 3-5: STRUERS Citopress-1(a) and STRUERS Tegramin-30 (b) [87].
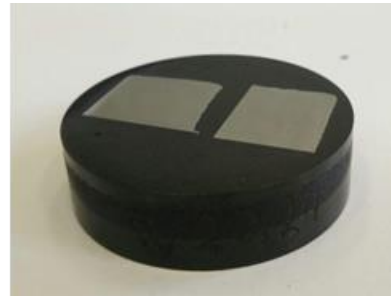
a)   *b)*

Figure 3-6: W20.24 surfaces after cutting process. a) Surface of the cross-section (on the plane XZ); b) Surfaces on the plane YZ (on the left side), and on the plane XY (on the right side).

3.3.1 Optical microscope and Stream Motion software

The two samples obtained from the W20.24 deposit, were observed using an Olympus BX60 Microscope. This machine was used to have a preliminary idea about the microstructure present in the deposit. The 2.5x, 5x and 10x of magnitude had been utilized, but the microscope has objectives with higher magnification up to 200x. A general overview of the three sections was taken, after that some other images were carried out using higher magnifications. These latest images were necessary to have a better look of the carbides and the phases formed in the deposit.

Figure 3-7: Olympus BX60 Microscope [88].

The Stream Analysis Software was used to analyze the pictures taken with the Olympus BX60 Microscope. Stream is an advanced software that allows acquiring, process and measuring images. The detection of the particles is possible thanks the recognition of the colors of the manually set scale. Thus, sophisticated results can be obtained thanks an easy customization. In this work it was used to investigate the dimensions and the distribution of the carbides present in the samples observed with the Olympus BX60. Preliminarily, general overviews of the three sections were taken, then also some pictures of some particulars were carried out.

At first Stream detected too many elements so it was impossible to process that amount of data. A more manageable set of data was obtained just adjusting the detecting color scale.

3.3.2 Scanning Electron Microscope

Further observations were carried out using the Phillips XL30 FEG-ESEM for a better understanding of the reactions between the WC and the SS316L thanks to the higher definition owned. The direct observation was made in the Secondary Electrons mode (SEM) and many images had been taken. The electron microscope also allows to take different composition profiles using EDS (Energy Dispersive Spectrometry). This technique was used to have a general idea about the chemical composition of the elements present inside the deposit. The Phillips XL30 FEG-ESEM in the EBSD mode (Electron BackScattered Diffraction) can recognize the different crystallographic lattices, and it was utilized too in this work.

The sample preparation for the Electron microscope is like the one used for the Optical observations, with a couple of additional steps. The samples embedded in the Bakelite are fixed in a metallic support to ensure that they do not move when they are tilted for carrying the EBSD images. Moreover, a silver painting is used to make easier the evacuation of electrical charges.
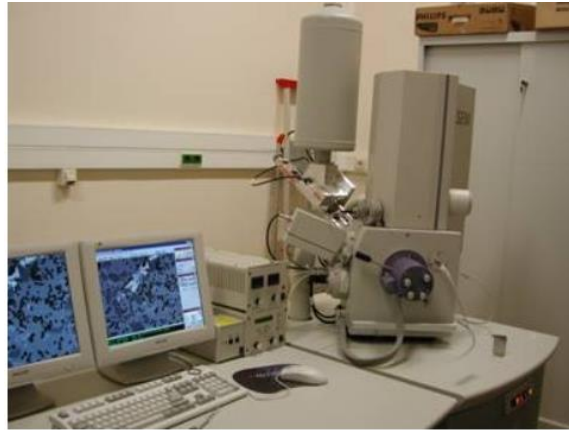
Figure 3-8: Phillips XL30 FEG-ESEM [89].

The SEM was used also for analyze the samples after the wear tests. This allowed to see if different phases were generated and if there was the presence of the counter-body used for the test on the wear track. Moreover, even the debris produced by the wear were observed. A final observation was performed on the cross section of the worn surface. One of the post-mortem samples was cut with the electrical discharger machine; the sections obtained were prepared for the SEM observation, and one of them was observed.

3.4 Macro-hardness

Hardness tests were performed on the section XZ, section XY and on pure SS316L as reference. The machine used is the EMCO M1C 010. It is a digital low-load hardness machine testing machine. Vickers, Brinell, Knoop and Rockwell tests can be performed using different weights. In this work it was utilized ASTM E-92 HV10. The machine is equipped of an automatic exchange of lens/indenter, fully automatic test cycle, automatic lens focusing, leading-edge high-resolution CCD camera, fully automatic image evaluation and manual cross slide.

The test was conducted manually moving by 1mm after each indentation. After each indentation the software measures the dimensions of it and gives a hardness value in the Vickers scale. It was obtained an indentation grid that gives a complete hardness characterization of the sample tested.

Figure 3-9: EMCO M1C 010 [90].

Hardness tests were performed in order to have a general idea about the evolution of the hardness of the deposit.

3.5   Tribometer

The wear tests were been performed with the High Temperature Tribometer 01-04611 provided by CSM Instruments SA. Since the acquisition of the machine to this work, CSM Instruments SA has been acquired by Anton Paar GmbH and its name changed in "CSM Instruments SA | A company of Anton Paar" [91].

1. Adjustable weight;	4. Sample;
2. Pin or ball holder;	5. Tribometer arm;
3. Locker ring;	6. Crank-handle for the adjustment of the friction radius.
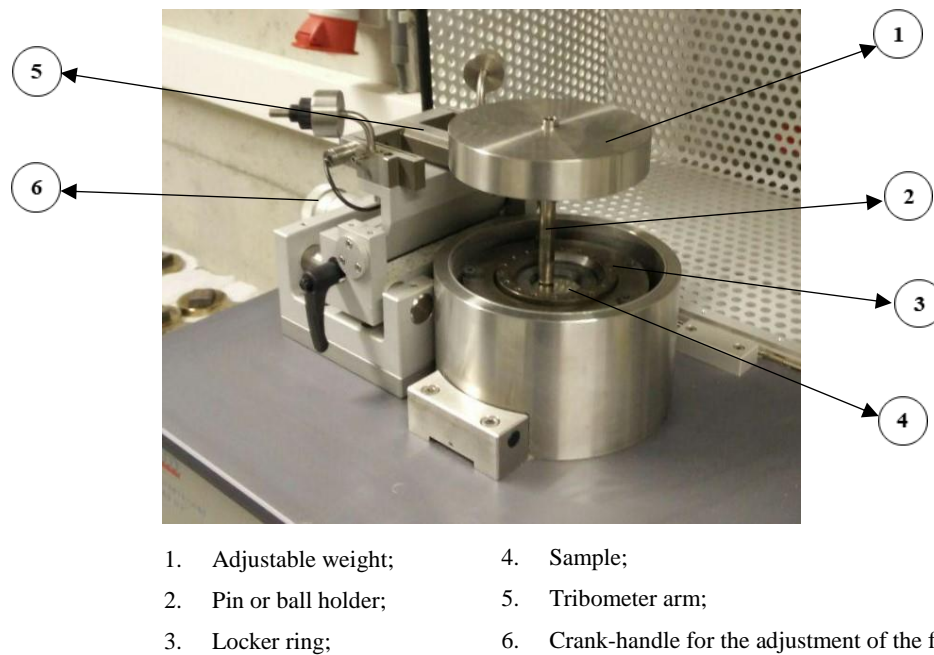
Figure 3-10: High Temperature Tribometer.

The CSM Tribometers are used to determine the sliding life of self-lubricant coatings, the friction behavior and wear of solid-state materials or hard coatings with varying time, contact pressure, velocity, temperature, humidity and lubricants [92]. The general description of the pin-on-disk test was already given on the section 2.5.2.

As the disk rotates, the resulting frictional forces acting between the pin and the disk are measured by very small deflections of the lever using a LVDT sensor. Wear coefficient for the pin and the sample is calculated. Indeed, after this test, the graph of the friction force, the graph of the penetration depth of the pin and the graph of the friction force are obtained.

The deposits needed to be cut and polished in order to obtain the samples suitable for the tests. The samples preparation was made in Leuven in collaboration with Prof. Sylvie Castagne (KU Leuven – Mechanical Engineering). The cutting was performed with a Spark Erosion machine and after that the samples were grinding polished. Moreover, additional deposits were sent for future wear tests.
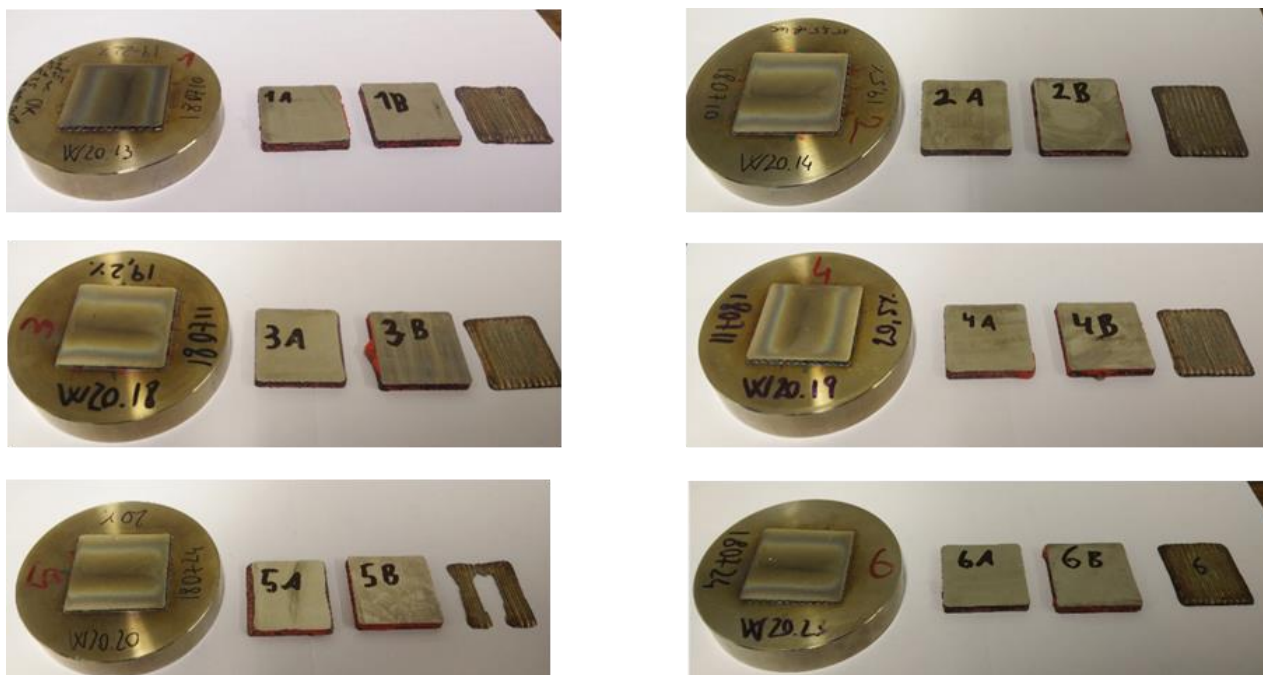
Figure 3-11: Samples cut and polished.
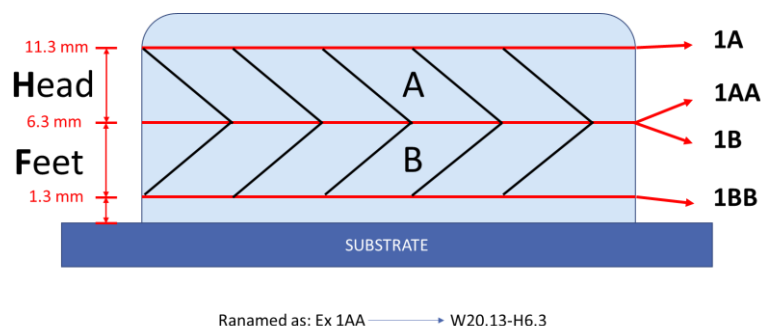
Figure 3-12: Cutting positions and sample designation.

In Leuven they gave to each sample a specific name, but we decided to change the designation. The new designation of each sample includes the name of the deposit from which it was obtained and if it corresponds to the lower or to the upper part (Feet and Head respectively). Moreover, each face has in its name the addition of the height at which it was cut. I.e. the face 1AA became the face W20.13-H6.3. Before each test the surface of the sample was cleaned using a methanol solution. The flat surface of the sample was held in a chuck attached to a variable speed drive.

In this work an alumina (Al_2O_3) with 3mm of radius was utilized as counter body for the pin. The pin holder is made of a base of stainless steel with the extreme part in Inconel 600 [92]. It was fixed perpendicularly to the sample surface by the arm.

The instrument was used for room temperature pin-on-disk tests in dry condition. Some preliminary trials were done in order to decide the set of parameters for the tribometer. It was decided to start using the parameters reported in the work of M. Vardavoulias and N. Hashemi on the High-Speed Steels [83,93].

Table 3-4: Initial parameters sets [83,93].

	Linear speed [m/s]	Load [N]	Stop condition [m]
Test 1	0.5	5	1400
Test 2	0.5	20	1400

The two preliminary tests were performed setting the position of the arm at 5mm and 8mm to the center of the sample. For them, a deposit with 15% of tungsten carbide was used. Since it was noticed that the damages of the ball were quite high with the two sets of parameters (Table 3-4) it was decided to change them.

Firstly, the deposit W20.19 was tested with the parameters shown in Table 3-5.

Table 3-5: Initial parameters sets.

		Radius [mm]	Linear speed [m/s]	Load [N]	Stop condition [m]
W20.19 F6.3	Test 3	8	0.1	5	1500
	Test 4	11	0.1	5	1500
W20.19 H6.3	Test 5	8	0.1	10	1500
	Test 6	11	0.1	10	1500

Considering the results obtained that are reported in the Chapter 4, the setup of the machine was decided.

This last setup was decided in order to understand the evolution of the friction coefficient and the wear mechanisms. Whereby the following tests were performed with the final parameters in Table 3-6. Moreover, in order to have two different tests on the same surface (sample), the tests were expressed in cycles. Unlike the previous cases, in meters.

Table 3-6: Final Tribometer setup

Radius [mm]	Linear speed [m/s]	Load [N]	Stop condition [cycles]
8	0.1	10	Up to 22000
11	0.1	10	

Indeed, the cycles consideration showed a higher reproducibility, even changing the radius of the tests.

In order to deeply understand the phenomena occurring during the sliding, a GoPro Hero7 was used to record the audio and video of the wear tests performed.

3.6   *Profilometer*

The Alicona InfiniteFocus G5 was used to analyze the samples and even the Al_2O_3 balls after each test. This machine uses a non-contact, optical, three-dimensional measurement principle based on Focus-Variation. Focus-Variation combines the small depth of focus of an optical system with vertical scanning to provide topographical and color information from the variation of focus itself. The main component of the system is a precision optics containing various lens systems that can be equipped with different objectives, allowing measurements with different resolution [94]. The instrument objectives magnification is up to 100x. For the analyzes made in this work the 5x, the 10x and the 20x were used.

Figure 3-13: Alicona InfiniteFocus G5 profilometer [94].

The software of the machine allows to verify if the sample almost flat. Moreover, after the tests, several measurements were carried out. In this way it is possible characterize every different test and its relative effect on the 316L Stainless Steel + WC wear behavior. Using different measurement options, it was possible to evaluate the depth of the whole wear track and of a section chosen as representative for each test. The width of this representative section was also evaluated. Finally, the dimensions of the ball were measured too. The color of the alumina ball is white. This made the measurements quite complicated. Indeed, the profilometer projects light on the object to perform the analyses. The not-consumed ball surface is highly reflective, and this inhibits the image acquisitions.

In addition to these general analyses, some deeper observations were made. Using higher magnification some images of the carbides inside the track were taken. They were processed in order

to check the variation of the depth before and after the encounter with the second hard phase dispersed on the material tested.

4. Results

4.1 Microstructural Characterization

4.1.1 Optical microscopy

Several microscope observations were performed in order to have a general idea about the microstructure of the material in examination. The four sections analyzed are:

- Section 1 on the XZ plane (it is the cross section to the respect of the building direction);
- Section 2 on the XZ plane;
- Section 3 on the YZ plane (parallel to the building direction);
- Section 4 on the XY plane.

The building direction is along the Y axis.

As mentioned in the paragraph 3.3, the section 2 was sent in France for vibrometer polishing preparation by PRESI. Some SEM images were carried out on it.
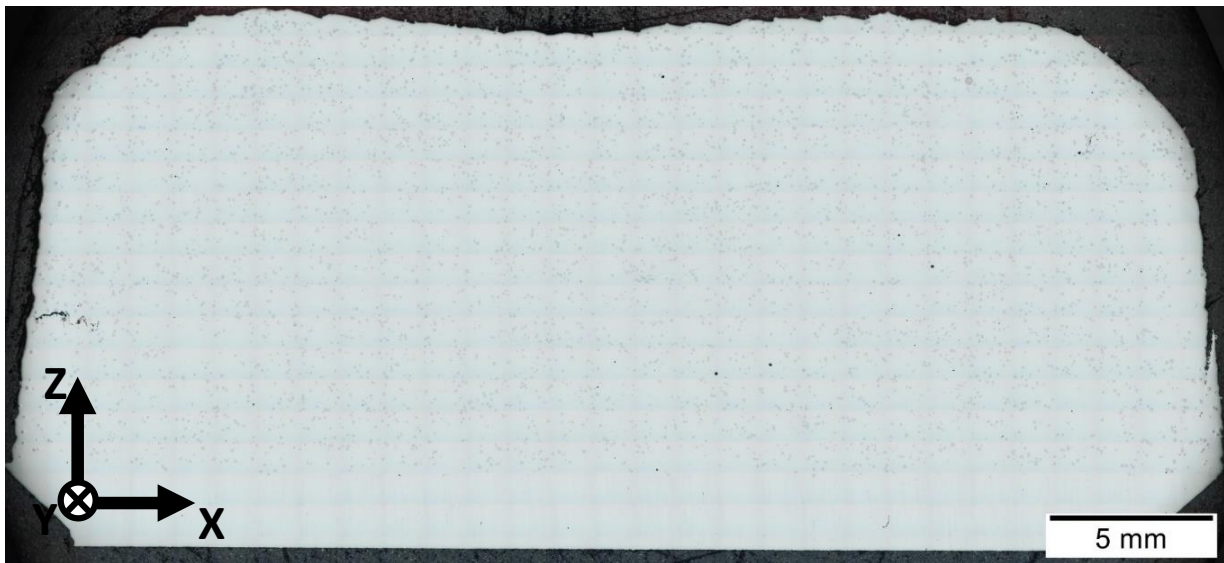
Figure 4-1: General overview of the section 1 (XZ) with the relative system of reference.
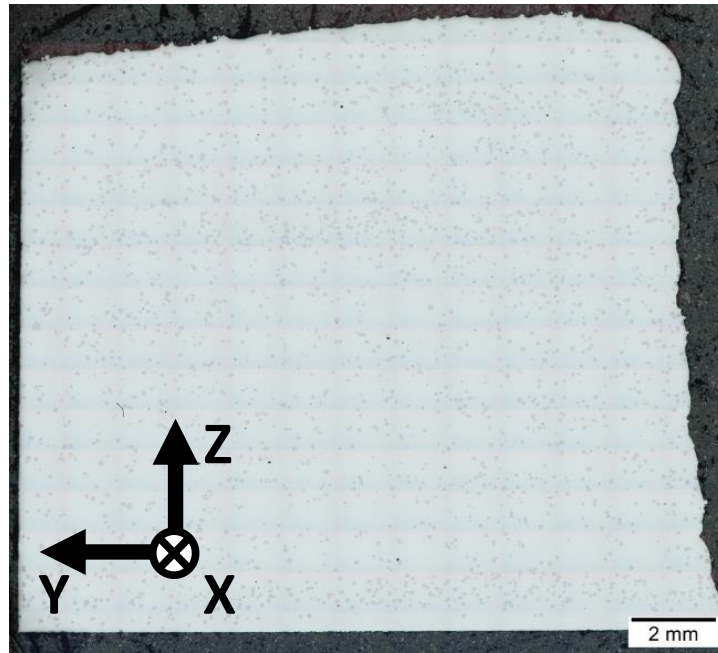
Figure 4-2: General overview of the section 3 (YZ) with the relative system of reference.
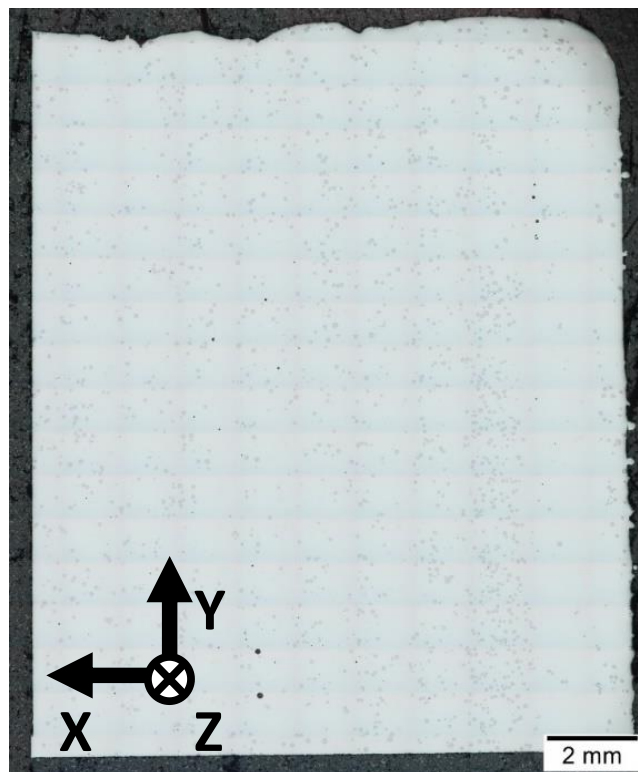
Figure 4-3: General overview of the section 4 (XY) with the relative system of reference.

The starting point of this analysis is the general overview of the sections in exam. The distribution of the carbides was evaluated for each of the section 1, 3 and 4 of the deposit W20.24.

An estimation of the carbides position and dimension was obtained using the Stream Motion Software by Olympus.
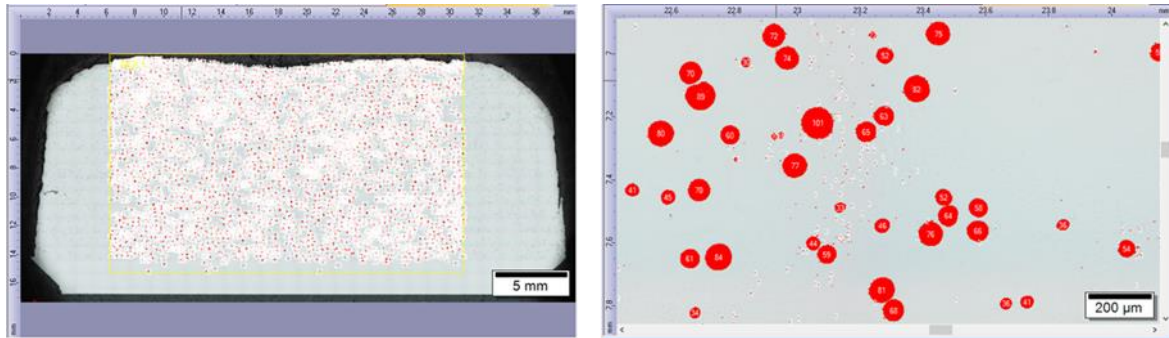
Figure 4-4: Stream motion analysis of the section XZ. The sides were not considered because they are quite different respect the bulk, moreover this sample had a crack on the left side.
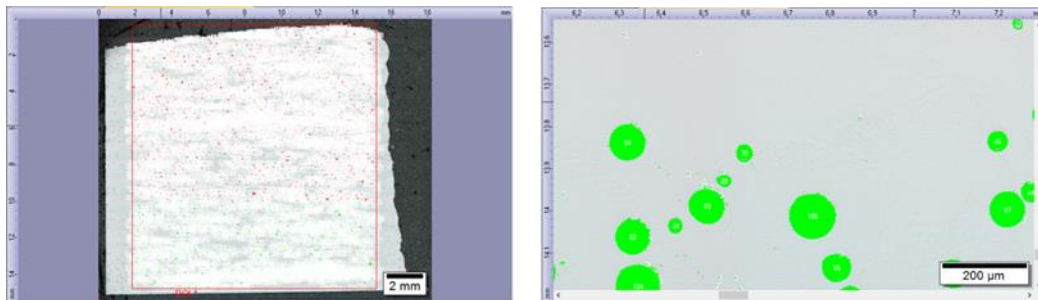
Figure 4-5: Stream motion analysis of the section YZ.
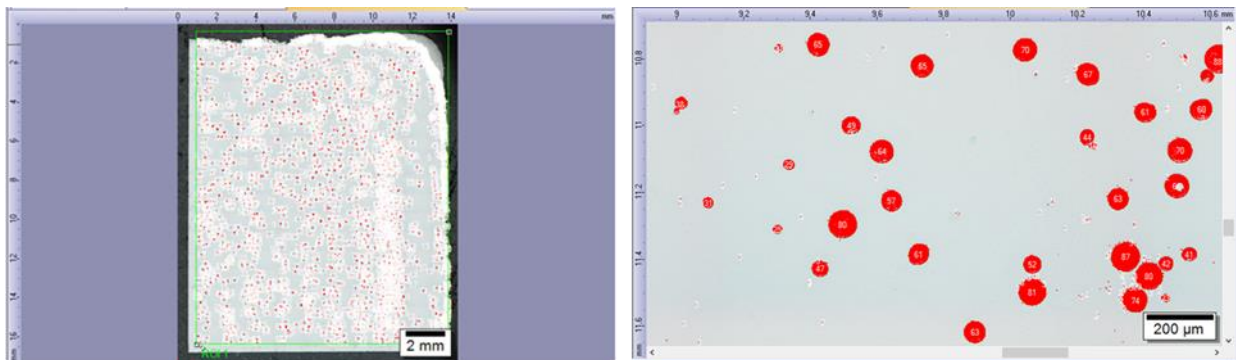
Figure 4-6: Stream motion analysis of the section XY.

On the right side of the Figure 4-4, Figure 4-5 and Figure 4-6 is reported a zoom of the analyzed zone. These images were used to filter the data obtained considering the size of the elements. In this way the carbides were detected with the greatest precision possible. Only the elements with a dimension between the 20µm and the 150µm were considered.

Thanks to this software and a data elaboration using Microsoft Excel and MATLAB, it was possible to obtain a distribution map of the carbides. Moreover, it was possible to have an estimation of the dimension of the carbides.
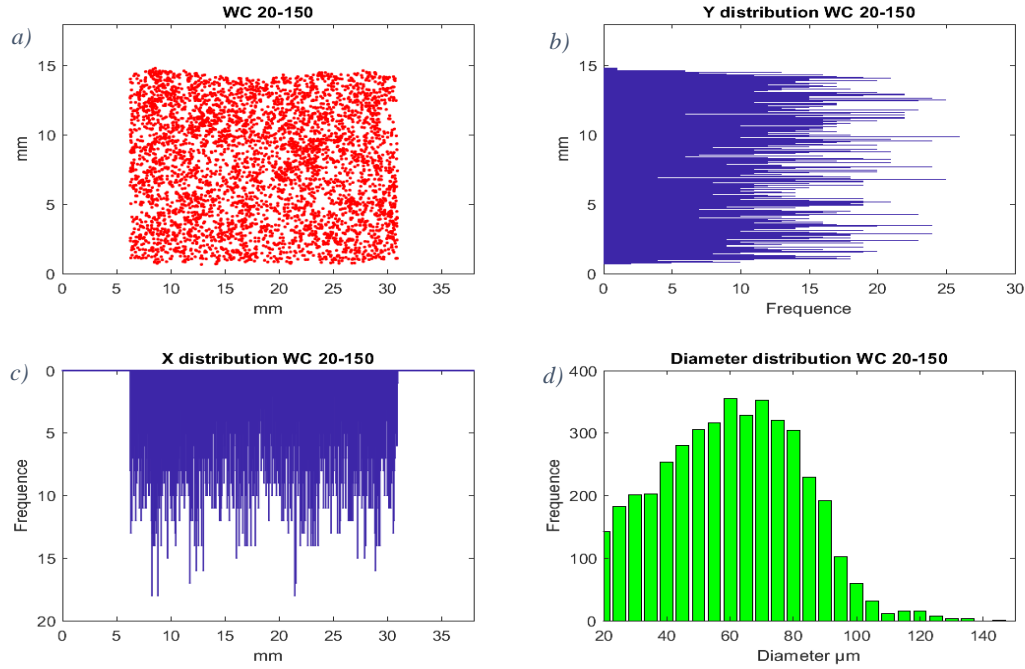
Figure 4-7: Section XZ a) Carbides distribution map; b) carbides distribution frequency in Y direction; c) carbides distribution frequency in X direction and d) carbide dimension frequency. The value of the frequency can be explained as the number of elements detected every 50µm.

Figure 4-7 shows the section on the XZ plane, perpendicular to the building direction. On the Y direction the carbides distribution is almost constant as on the X direction.

In the Figure 4-7 d) the max frequency of the elements detected dimension is at around 70µm.
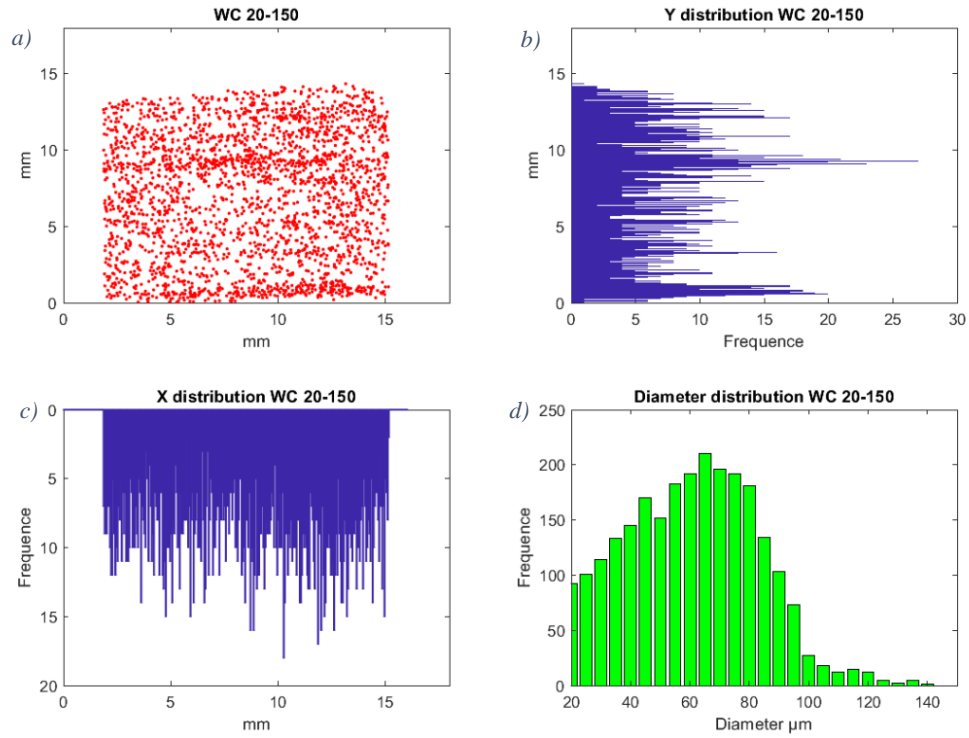
Figure 4-8: Section YZ a) Carbides distribution map; b) carbides distribution frequency in Y direction; c) carbides distribution frequency in X direction and d) carbide dimension frequency.

Figure 4-8 shows the section on the YZ plane, parallel to the building direction. In the Y direction the frequency of the carbides amount has two peaks.

As for the section on the XZ plane, there is a peak in the diameter frequency at around 70µm.
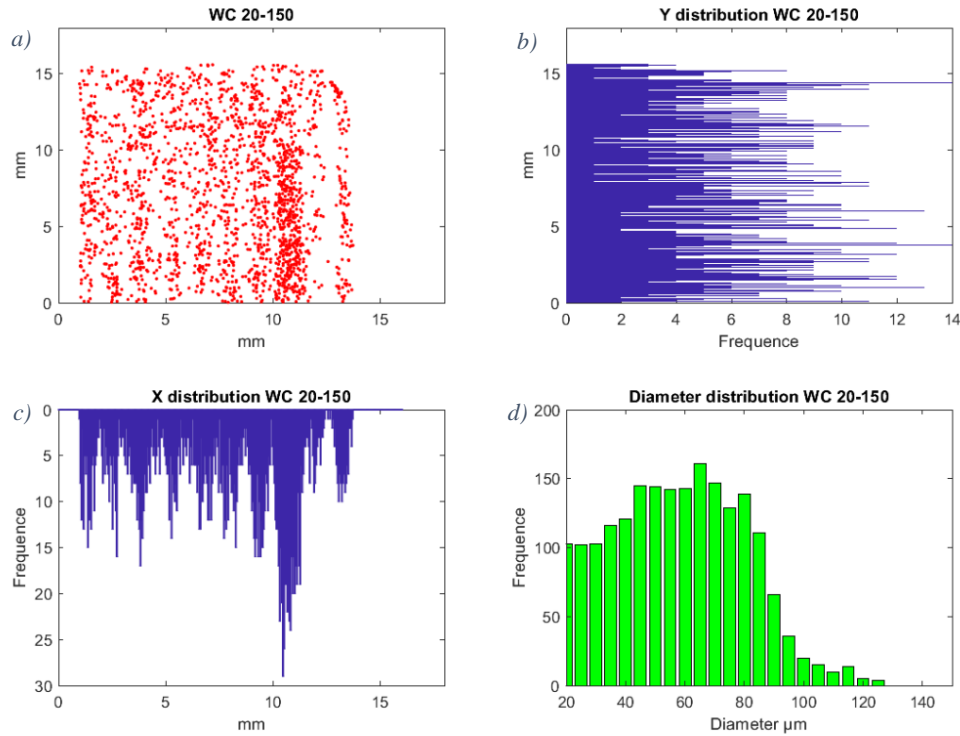
Figure 4-9: Section XY a) Carbides distribution map; b) carbides distribution frequency in Y direction; c) carbides distribution frequency in X direction and d) carbide dimension frequency.

Figure 4-9 shows the section on the XY plane. Here in Y direction the distribution is quite homogeneous. There are discontinuities. Looking at the scale of the frequency considered, it can be said that those discontinuities are very small. On the contrary, on the X direction a big change in the frequency is noticed. A constant trend is present in the bulk material.

Likewise, the two previous sections, the max frequency of the diameter of the carbides is at around 70µm.

From the general overview, it was interesting to make additional observations at higher magnifications in order to characterize the microstructure. Moreover, some particular zones where detected, i.e. big tungsten carbides from the original powder, austenitic matrix and dispersed complex regular carbides had been observed.

a)   *b)*
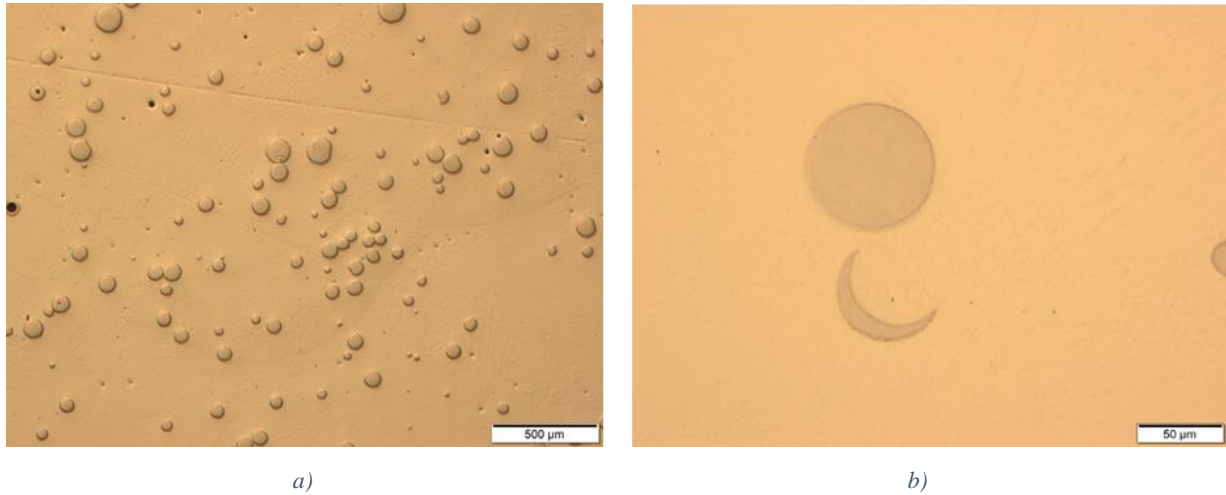
Figure 4-10: a) Different tracks detected in the XZ section. b) Spherical big tungsten carbide and a very particular "moon"-shaped tungsten carbide in the XZ section. Here it is also possible to notice the presence of the cellular dendrite microstructure.
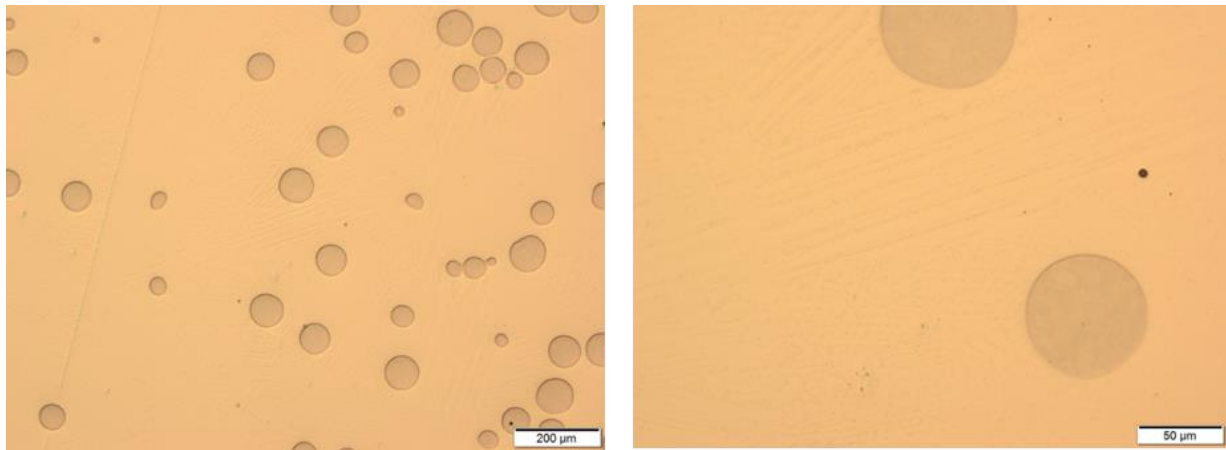
Figure 4-11:Dendrite across the track and the Heat Affected Zone detected in the XY section.

4.1.2 Scanning Electron Microscopy

A deeper observation of the microstructure was performed using the Scanning Electron Microscope (SEM). The same zone observed with the optical microscope and additional zones (HAZ and surroundings) where analyzed with the SEM. Moreover, different EBSD analyses were carried out, but with uncompleted results. The only good results (Figure 4-27, Figure 4-29) were obtained on the section XZ, after Vibrometer preparation.

Figure 4-12 is the equivalent SEM image of Figure 4-10a, captured with the optical microscope. In the SEM micrograph the observation of same track shapes is easier.
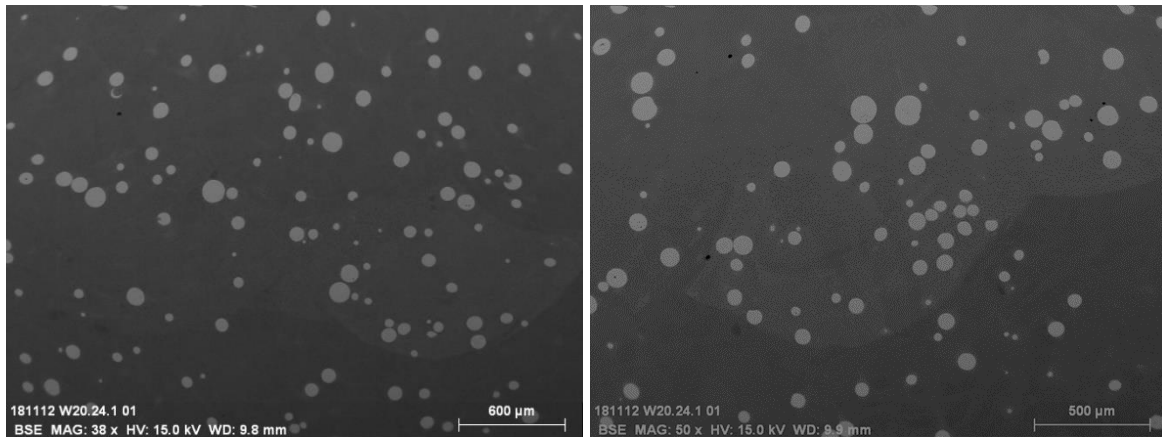
Figure 4-12: Large SEM images detected on the XZ section. It is possible to distinguish the different tracks

Figure 4-13 allows seeing the different phases that were formed during the solidification near the big tungsten carbides due to a really peculiar composition enriched in W and the complex regular carbides that form in the track. The carbides in the intercellular spaces appear of larger size and brighter in the surrounding of the WC carbides in comparison with the carbides solidified far from them (Figure 4-14).
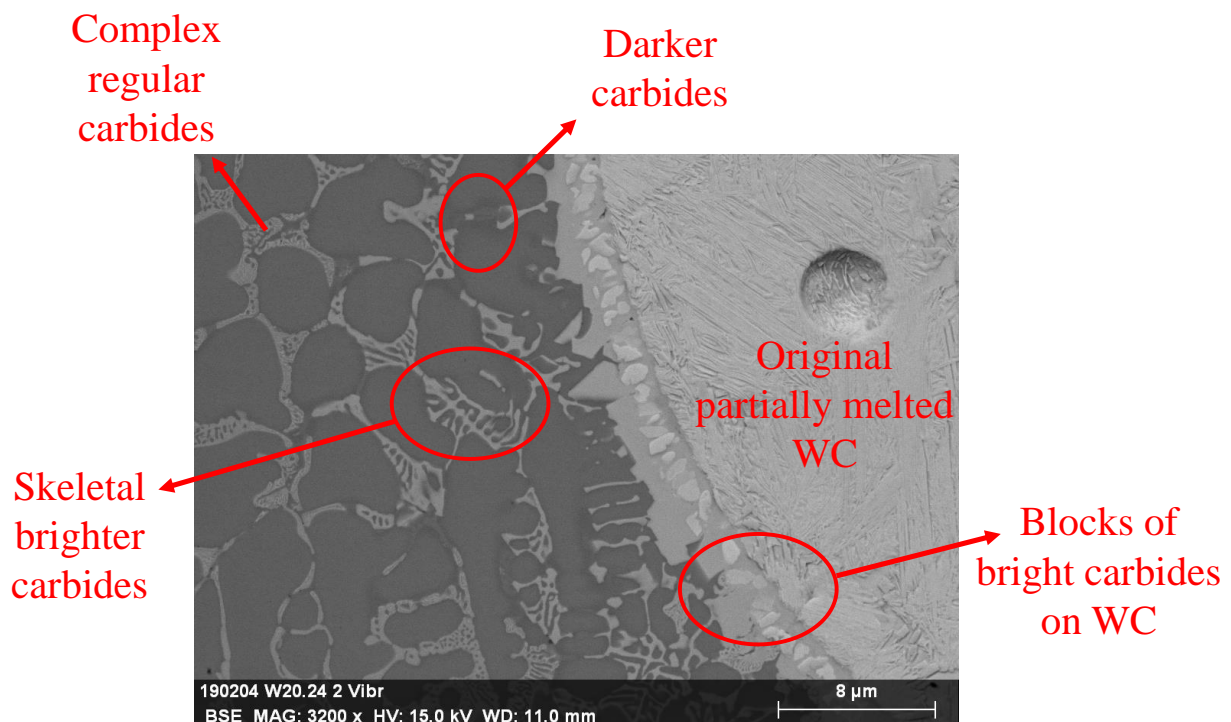
Figure 4-13: Different phases detected.
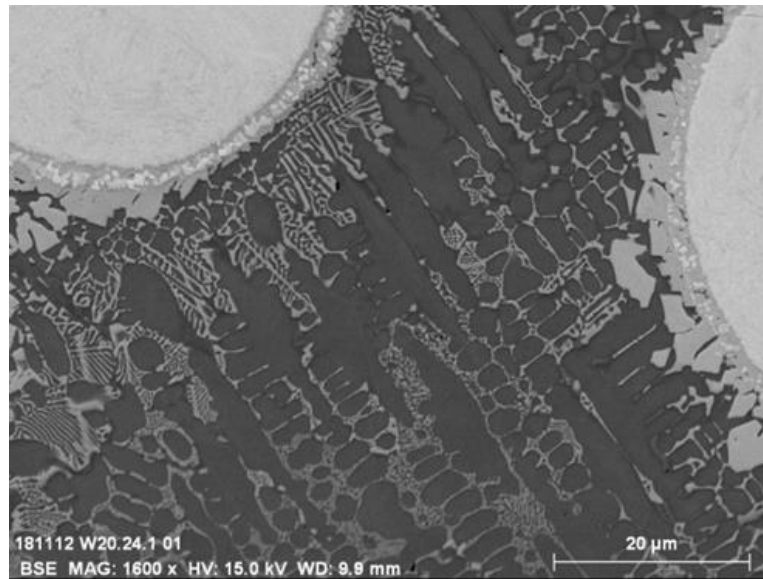
Figure 4-14: SEM images of a zone near the WC.

Observing the previous micrographs (Figure 4-13 and Figure 4-15), the carbides appear with a completely different morphology. Indeed, in the HAZ two different carbides are observed, meanwhile in the track only the complex regular carbide is observed. The brighter carbide in Figure 4-15 has a brighter color than the complex regular carbide in Figure 4-13 because it is richer in "heavy" atoms. Consequently, the darker carbide has lighter atoms.
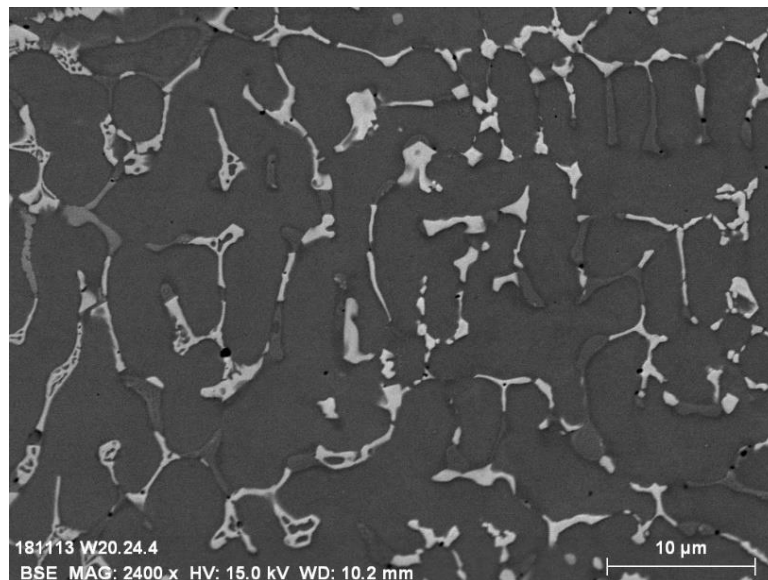
Figure 4-15: High magnification SEM image in the Heat Affected Zone.

The HAZ was well detected on the section XY, as it is shown in the following figures.

a)

b)

| *c)* | *d)* | *e)* |
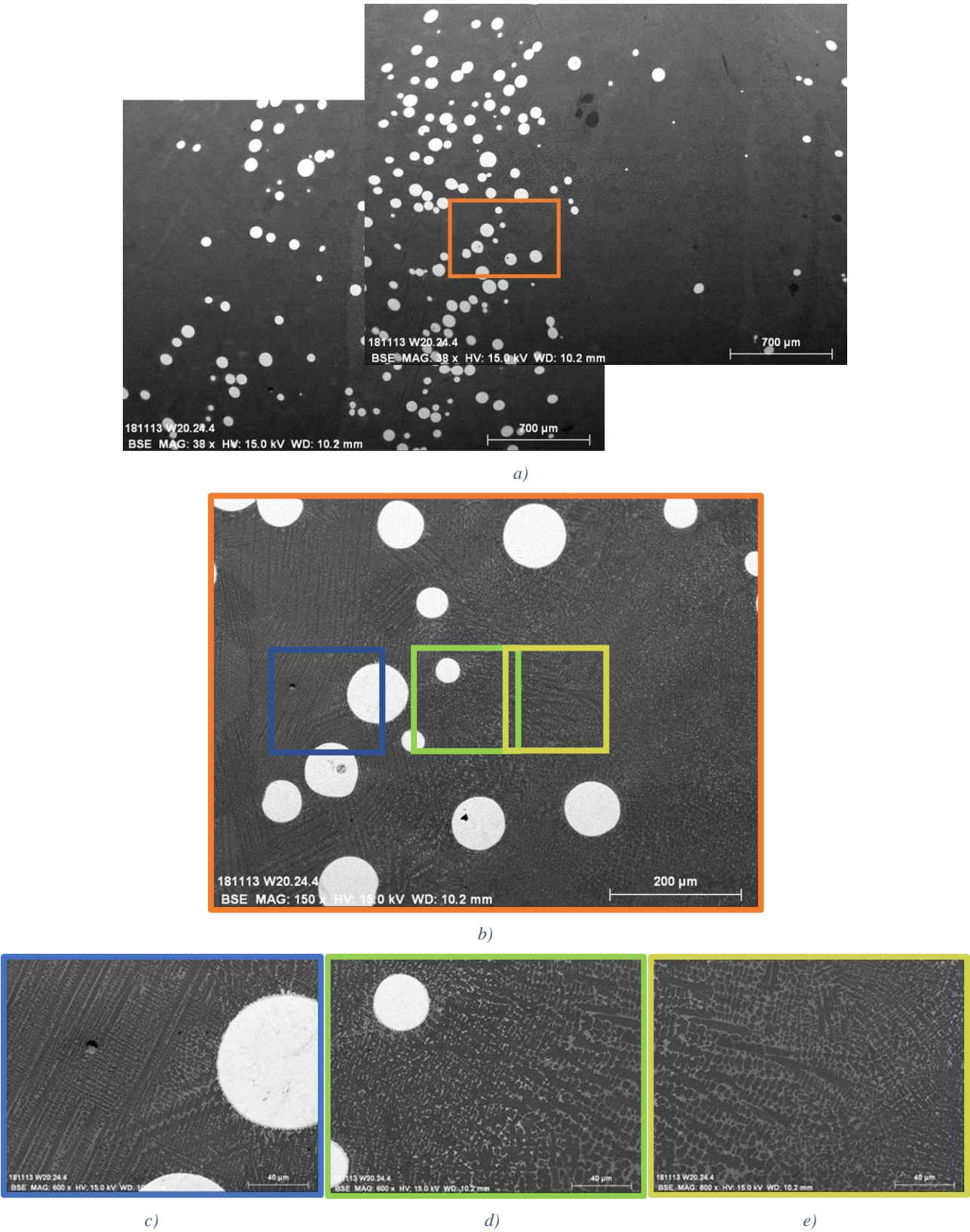
Figure 4-16: SEM images from XY section. a) General overview close to the side; b) zoom from the zone in a); c), d), e) zoom of different zones in b).

A different microstructure can be noticed in the Figure 4-16d. The heat affected zone (HAZ) is characterized by the presence of two carbides in the intercellular spaces.
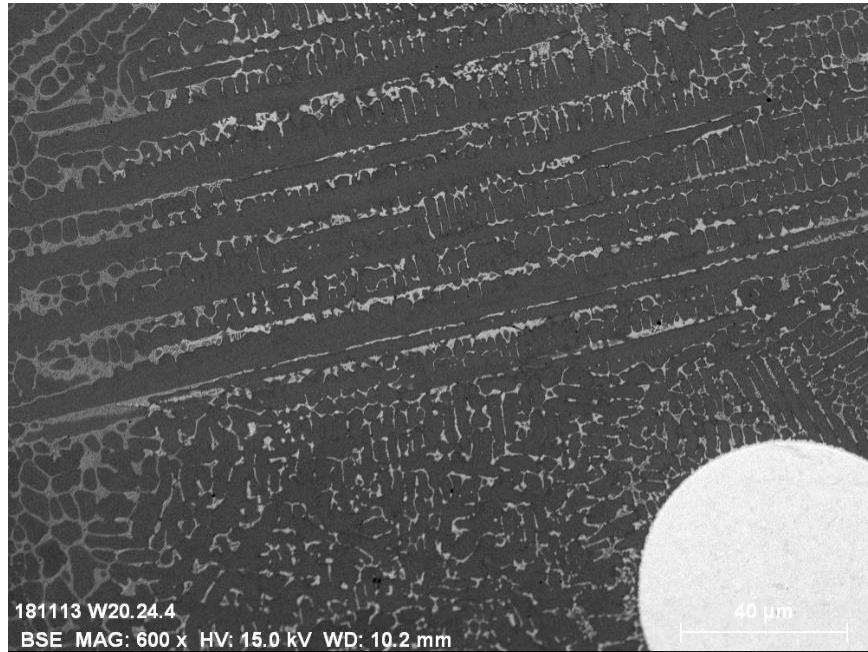
Figure 4-17: SEM image of the HAZ zone. The dendrite continues his growth in the HAZ.

In order to investigate the chemical composition of the carbides present in the HAZ, two different profiles were drawn using the EDS mode of the SEM. The elements and their amounts have been analyzed and quantified.

.
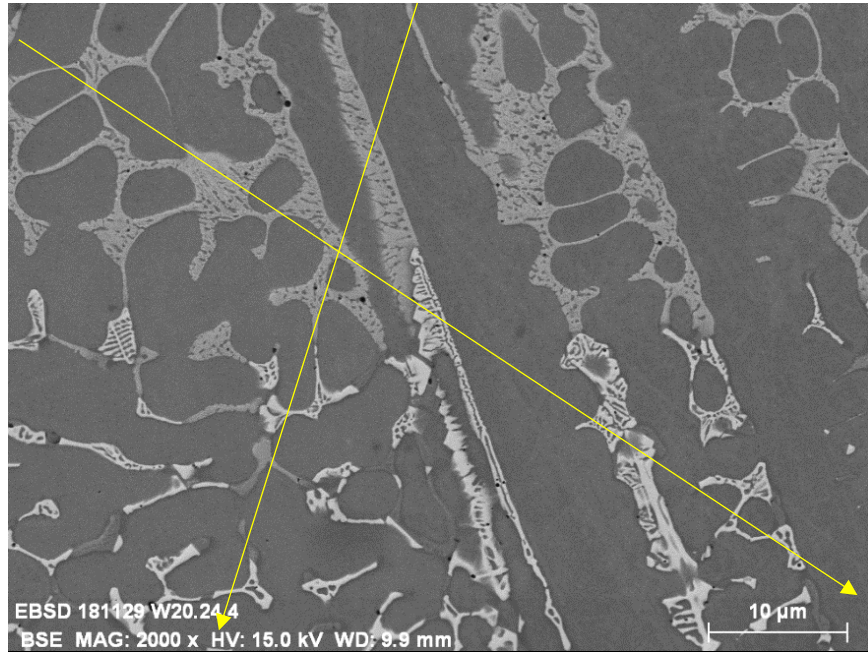
Figure 4-18: SEM images of a detail in the HAZ with profile 1 and profile 2 for EDS analysis.
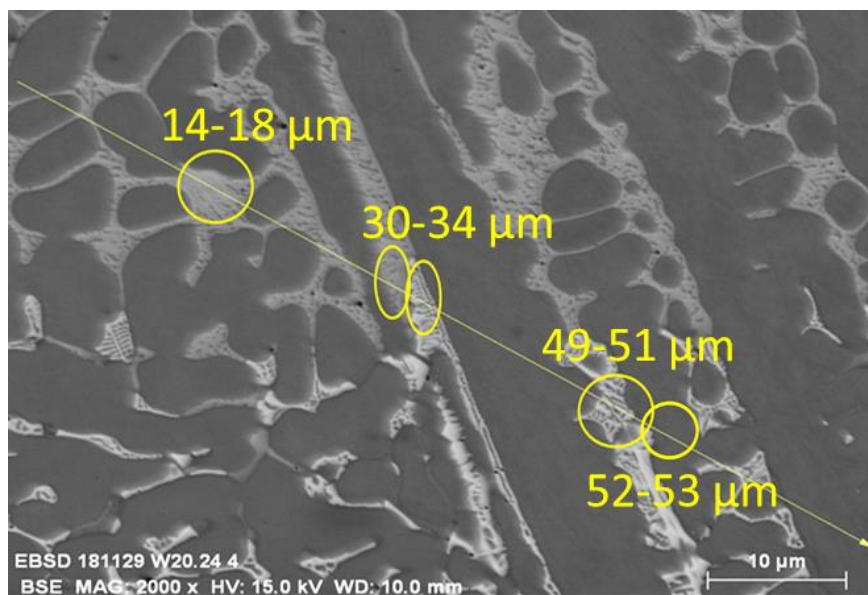
Figure 4-19: Zones considered along profile 1.
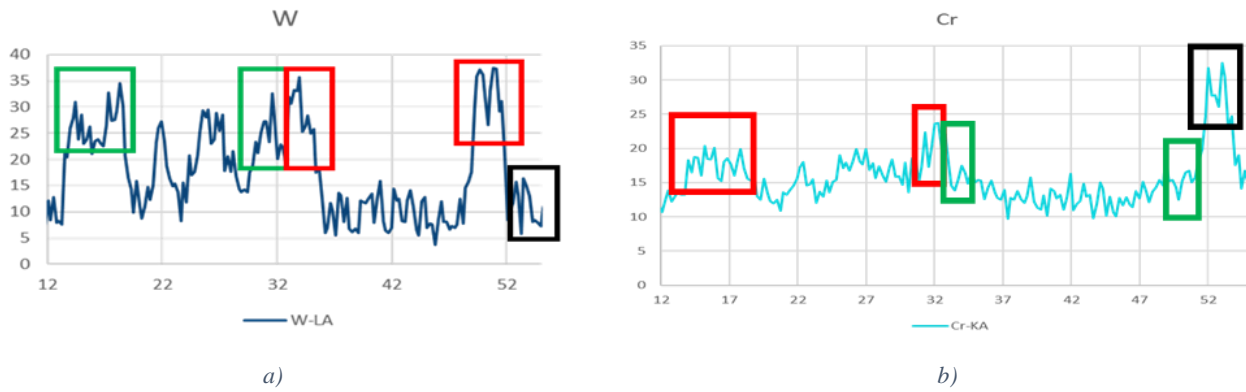
Figure 4-20: a), b) tungsten and chromium spectrum respectively.

Peaks and valleys were noticed in the tungsten (W) and chromium (Cr) spectra. Thus, the amount in mass of different elements was quantified and analyzed. The results are shown in Table 4-1.

Table 4-1: Mass amount of the elements within the zones considered along profile 1.

Mass%	C	Cr	Fe	Ni	W	Mo	Si	Mn
Tungsten carbide 14-18 µm	4.215	17.88	42.16	5.81	25.96	3.38	0	0.56
Tungsten carbide 30-32 µm	4.27	20.28	40.84	5.34	24.74	3.96	0	0.53
Tungsten carbide 33-34 µm	4.23	15.79	37.45	4.83	32.86	4.40	0	0.42
Tungsten carbide 49-51 µm	4.50	15.16	35.32	5.48	33.90	4.69	0	0.93
Cromium carbide 52-53 µm	4.75	29.38	45.71	5.19	10.84	3.46	0	0.63

In the brighter zones, that belong to the HAZ, a higher amount of W and a slighter amount of Cr can be noticed, except in the last range between 52 and 53 µm. Indeed, that zone is not as bright as the others, but it is darker.

The atomic composition of the elements in the same zones was also considered. The atomic amount of the elements detected can give an indication for identify the exact type carbides. Peaks and valleys are present also in this spectrum.
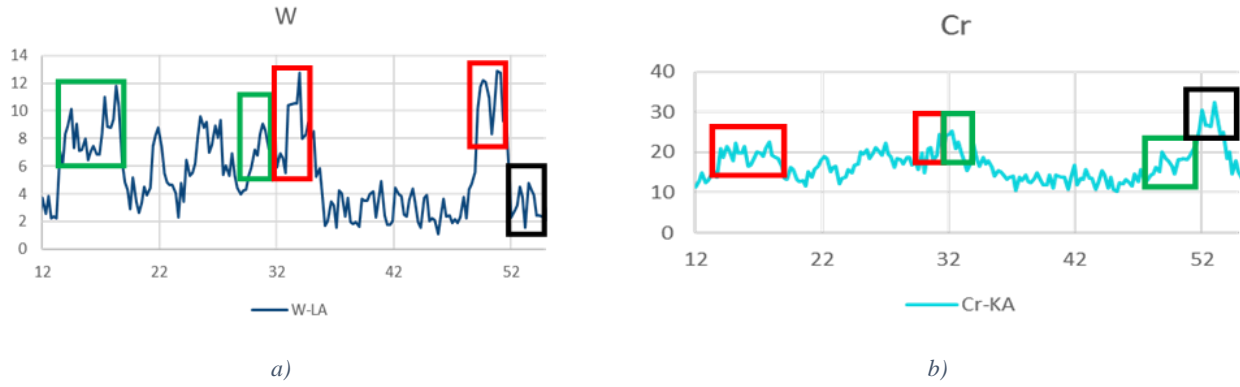
Figure 4-21: a), b) tungsten and chromium spectrum respectively.

Table 4-2: Atomic amount of the elements within the zones considered along profile 1.

Atom%	C	Cr	Fe	Ni	W	Mo	Si	Mn
Tungsten carbide (W6C) 14-18 μm	20.18	19.82	43.47	5.70	8.17	2.03	0	0.60
Tungsten carbide (W6C) 30-32 μm	18.50	21.27	41.95	6.02	8.98	2.54	0	0.70
Tungsten carbide (W6C) 33-34 μm	21.26	18.58	40.89	5.05	10.92	2.80	0	0.47
Tungsten carbide (W6C) 49-51 μm	22.75	17.75	38.51	5.71	11.25	2.97	0	1.03
Cromium carbide (Cr23C6) 52-53 μm	20.03	28.62	41.43	4.48	3.00	1.82	0	0.58

The same trend noticed in Table 4-1 is present in Table 4-2. Inside the track the darker carbides own both Cr and W. In the HAZ the amount of Cr decreases and the amount of W increases. In the last zone, that is the darkest one, the amount of W is very low instead of the Cr that is the highest.
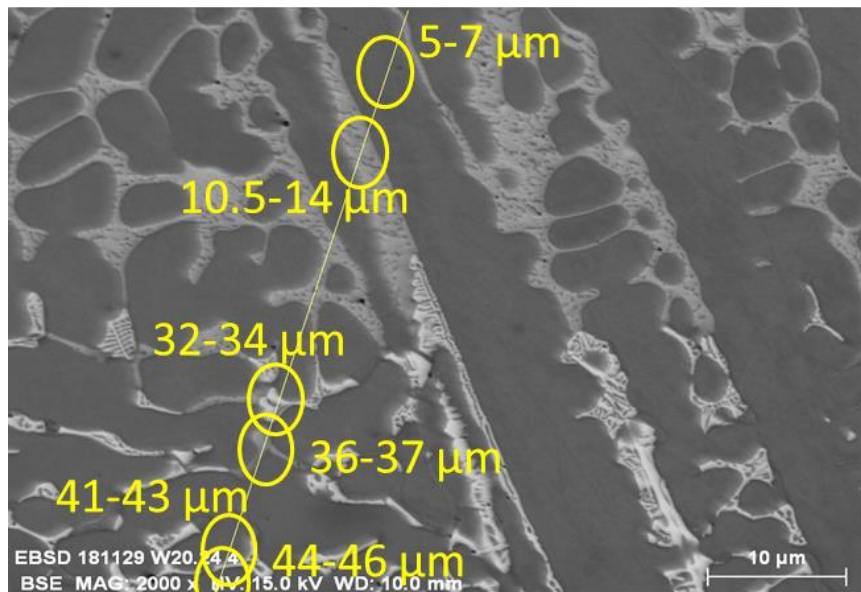
Figure 4-22: Zones considered along profile 2.

Like profile 1, profile 2 crosses the track and the HAZ. Profile 2 was divided in zones too, in order to check the evolution of the chemical composition of the carbides. Moreover, in this second case the matrix in the track and in the HAZ was analyzed. In Figure 4-23 a darker carbide in the HAZ is highlighted.
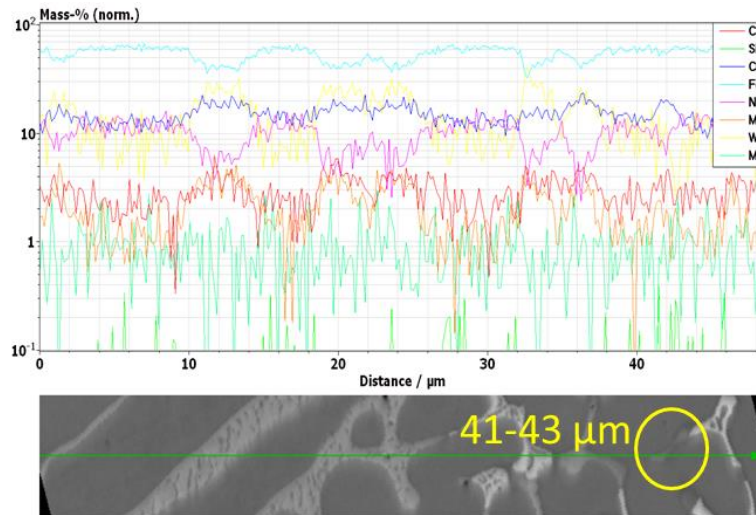
Figure 4-23: Global elements spectrum

a)   *b)*
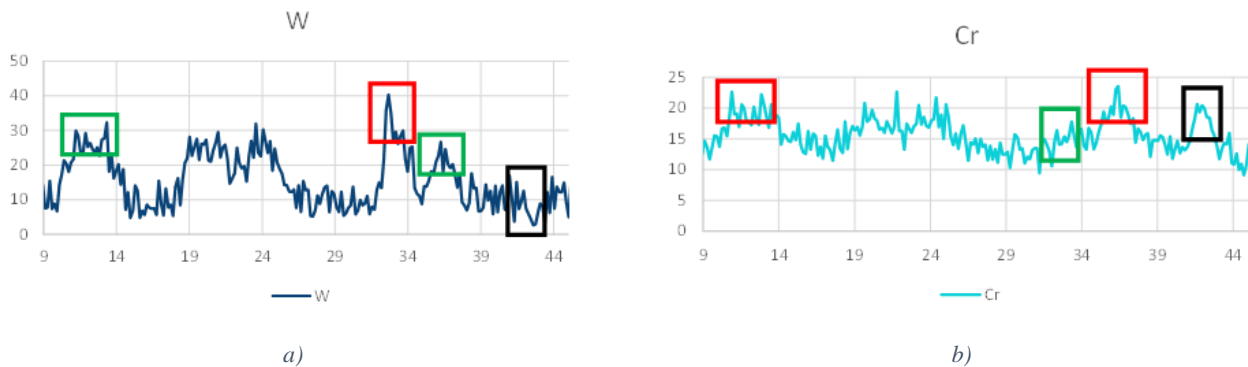
Figure 4-24: a), b) tungsten and chromium spectrum respectively.

Sharp variations are noticed in tungsten (W) and chromium (Cr) spectra.

Table 4-3: Mass amount of the elements within the zones considered along profile 2.

Mass%	C	Cr	Fe	Ni	W	Mo	Si	Mn
Matrix 5-7 μm	2.04	12.21	62.36	12.13	9.12	1.09	0.03	0.98
Tungsten carbide 10-14 μm	3.66	18.71	42.50	6.41	24.10	3.75	0	0.83
Tungsten carbide 32-34 μm	3.90	15.28	39.79	5.60	31.64	3.32	0	0.42
Tungsten carbide 35-37 μm	4.26	20.45	44.88	4.84	21.55	3.18	0	0.81
Cromium carbide 41-43 μm	3.30	18.42	58.49	9.71	7.17	1.81	0.11	0.96
Matrix 44-46 μm	2.48	11.95	59.35	12.97	10.98	1.22	0.06	0.95

62

Inside the track the composition of the carbide is similar to profile 1. The local average amount of Cr is close to 20%, instead the amount of W is close 25%. In the HAZ the tungsten amount is higher up to ~30%, on the contrary, the chromium amount decreases down to ~15%. In Figure 4-23 the presence of darker carbides can also be seen in the HAZ. The respectively analyzes show a higher amount of Cr and a lower amount of W in respect of the zone between 32µm and 34µm.

The matrix owns the lowest amount of C and the highest of Fe. No significantly variations are noticed in the composition of the matrix inside the track and the matrix inside the HAZ.
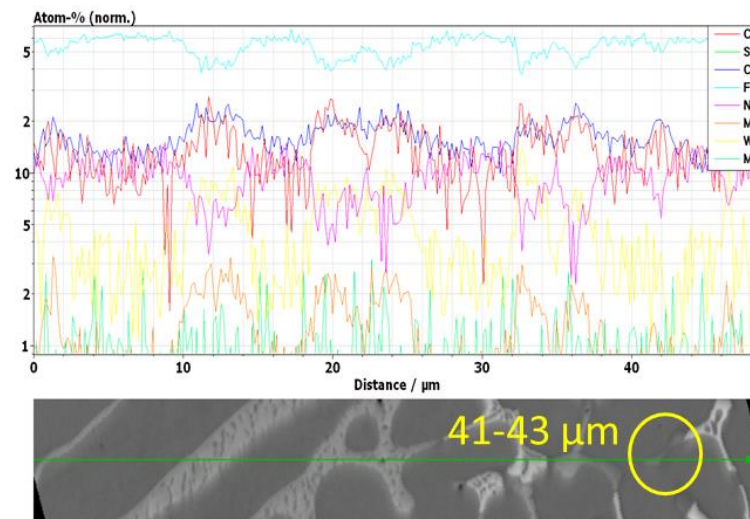
Figure 4-25: Global elements spectrum.

a)   *b)*
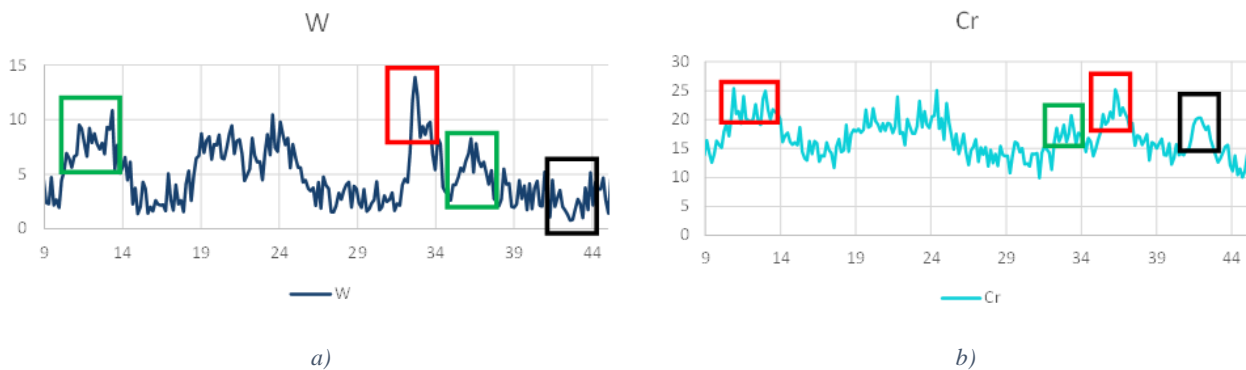
Figure 4-26: a), b) tungsten and chromium spectrum respectively.

Atom%	C	Cr	Fe	Ni	W	Mo	Si	Mn
Matrix 5-7 µm	9.32	12.98	61.75	11.46	2.79	0.62	0.06	0.98
Tungsten carbide(W6C) 10-14 µm	17.65	20.93	44.24	6.36	7.65	2.26	0	0.88
Tungsten carbide(W6C) 32-34 µm	19.76	17.93	43.38	5.79	10.53	2.11	0	0.47
Tungsten carbide(W6C) 35-37 µm	19.69	21.85	44.66	4.59	6.53	1.84	0	0.82
Cromium carbide (Cr23C6) 41-43 µm	14.25	18.44	54.53	8.60	2.04	0.98	0.21	0.91
Matrix 44-46 µm	11.36	12.69	58.62	12.20	3.32	0.70	0.12	0.96

Even along the profile 2, the atomic amount follows the trend of the mass amount.

4.1.3 EBSD

The Electron Back-Scattered Diffraction mode did not give good results when it was used in order to identify the phases of the carbides dispersed in the matrix, far from the "giant" tungsten carbides (WC). On the section polished using the vibrometer it was possible to have good indexation and identification of the phases. Figure 4-27 shows the zone chosen before the test and the pattern quality, meanwhile in Figure 4-29 the different colors represent the phases identified.

a)   b)
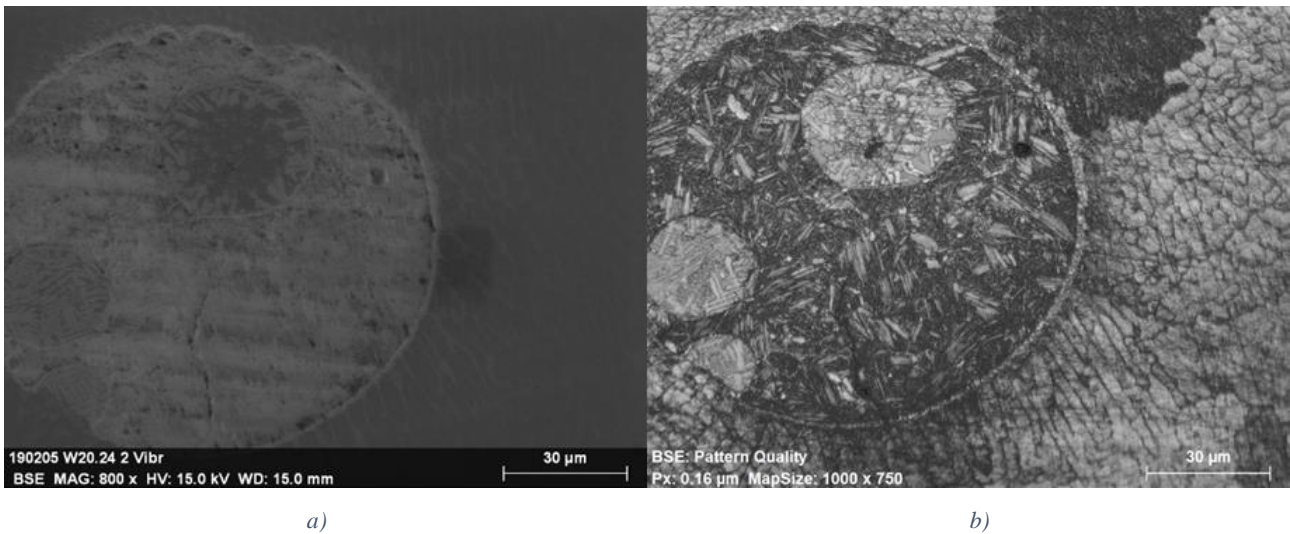
Figure 4-27: a) SEM image of the particular "giant" carbide; b) Pattern quality of the EBSD analysis.

The pattern quality indicates the quality of the indexation. The brighter zones indicate the crystal lattice is well indexed, meanwhile the darker zones mean the indexation was not possible. In general, the reasons can be bad sample preparation, supersaturation, peculiar texture of a growing direction and distortion [95]. The result obtained was very good since the matrix is completely well

indexed, except a grain in the higher part of the image, and around and into the giant WC carbide many crystals are well indexed (Figure 4-27b).
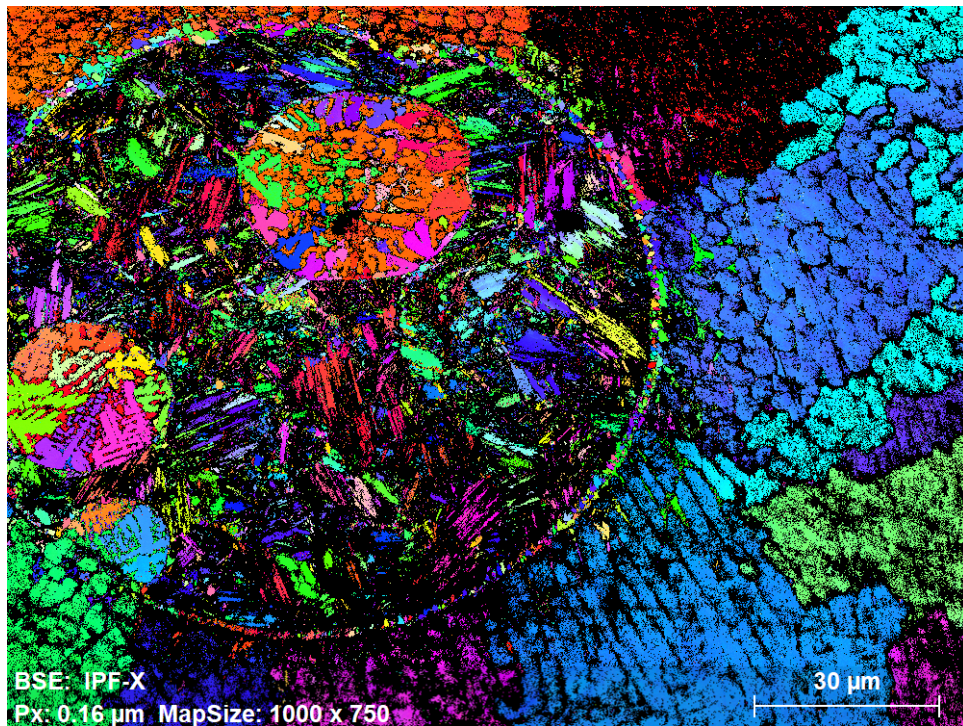
Figure 4-28:Different orientation of the phases detected.

The phases recognized are enumerated in

Table 4-5. From this analysis it can be noticed the beginning of the solidification takes place on the WC since some crystals nucleate and grow from it (Figure 4-28).
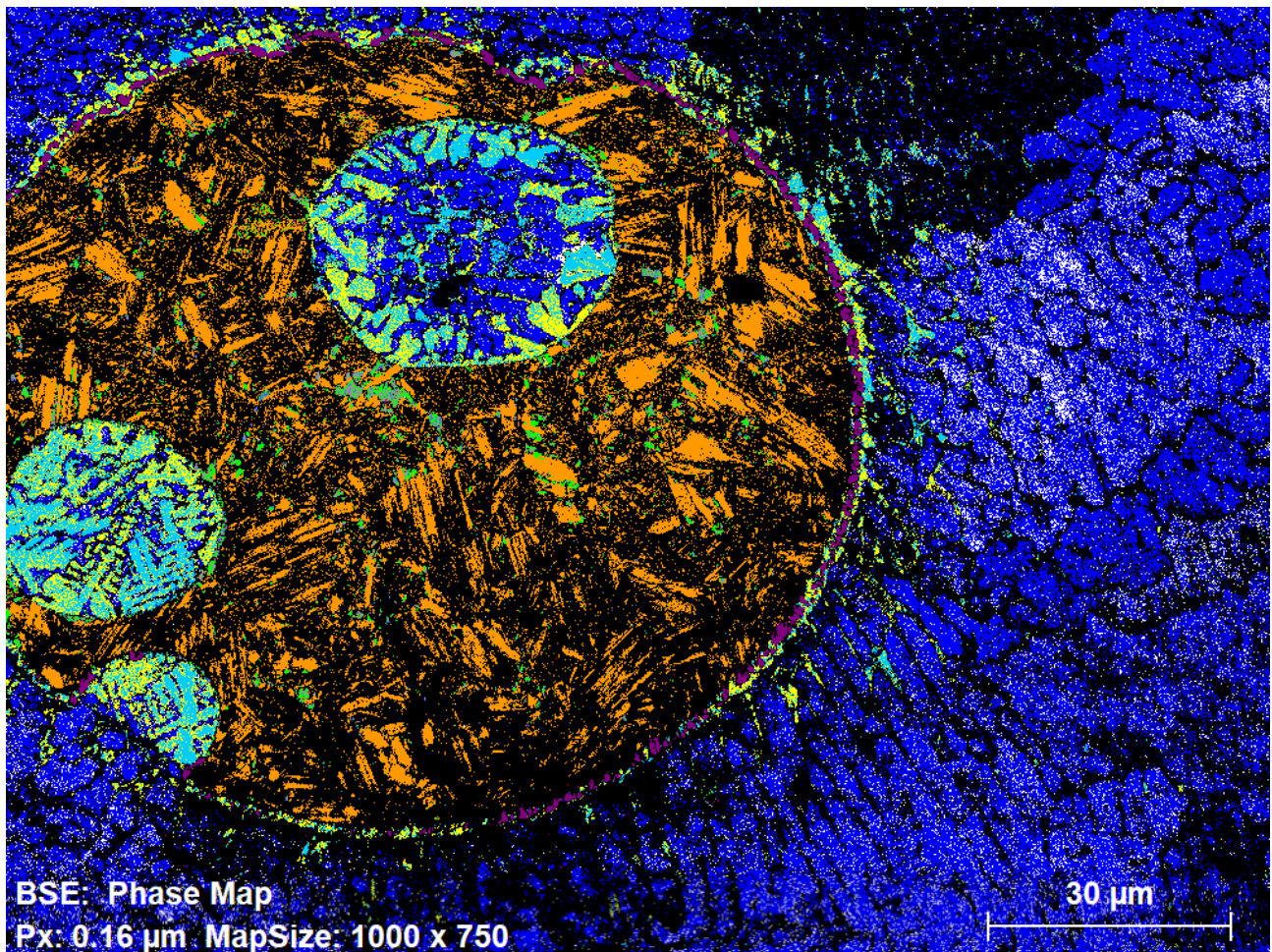
Figure 4-29: EBSD result. Phase map

Table 4-5: Phases detected.

Phases	
	Matrix (Austenite)
	Tungsten carbide (Qusongite MC)
	Tungsten
	Iron tungsten carbide
	Molybdenum carbide (tungsten carb M6C/M23C6)

The giant WC is identified as MC (Hexagonal crystal lattice) and M2C carbide (Trigonal and Orthorombic crystal lattice). A narrow layer of pure tungsten (BCC) is observed around it from the interaction with the liquid metal [95]. The solidification carbides formed around the carbide are identified as cubic crystal lattice, meanwhile the complex regular carbides are well indexed, but they were not identified. In the case of the cubic carbides around the WC, they were associated to M6C

and M23C6 carbides depending on the W and Cr amount. Indeed, their lattice structure is similar and the EBSD is not able to distinguish them completely [96].

4.2 Macro hardness
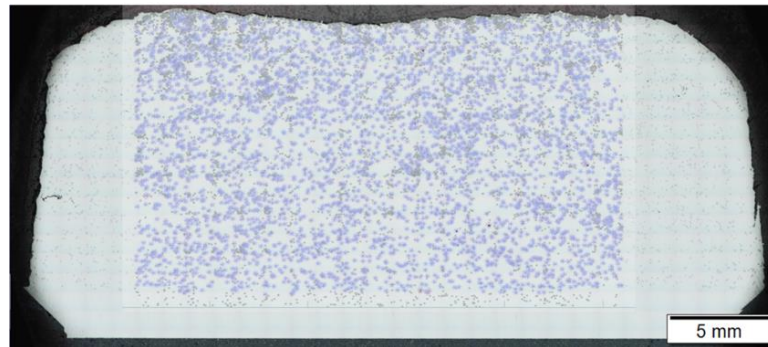
Figure 4-30: Projection of carbides distribution on the section on XZ plane overview.

Hardness tests were performed using as reference the overview taken with the optical microscope.
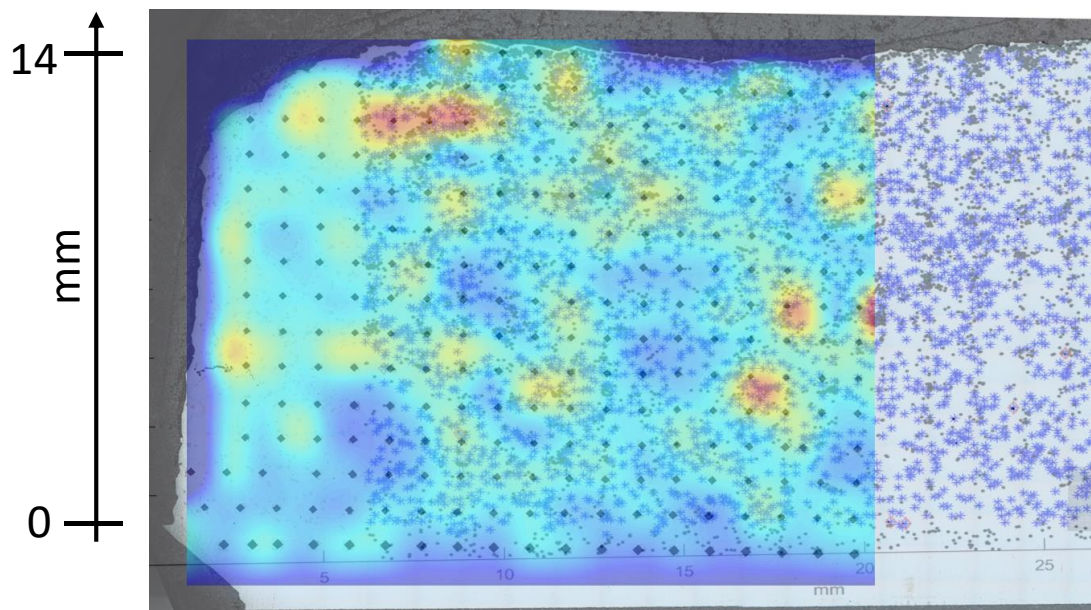
Figure 4-31: Overlaying of the carbides distribution and hardness map on the indentation grid overview.

The macrohardness grid obtained is shown in Figure 4 31. The elaboration of the data of the HV10 values using MATLAB, allows creating a hardness map where harder zones can be well distinguished. In Figure 4-32a) the average value of every height is plotted. It is possible to observe a maximum at 7 mm from the substrate and a slightly decrease of the hardness at higher distances from the substrate.

The same hardness test was performed on the pure SS316L in order to have a reference (Figure 4-32b)). A linear trend can be noticed on the SS316L. The hardness decreases with the distance from the substrate.

The average hardness value (320 HV10) given by the test on the SS316L+WC is higher respect the one obtained on the pure SS316L (200 HV10).
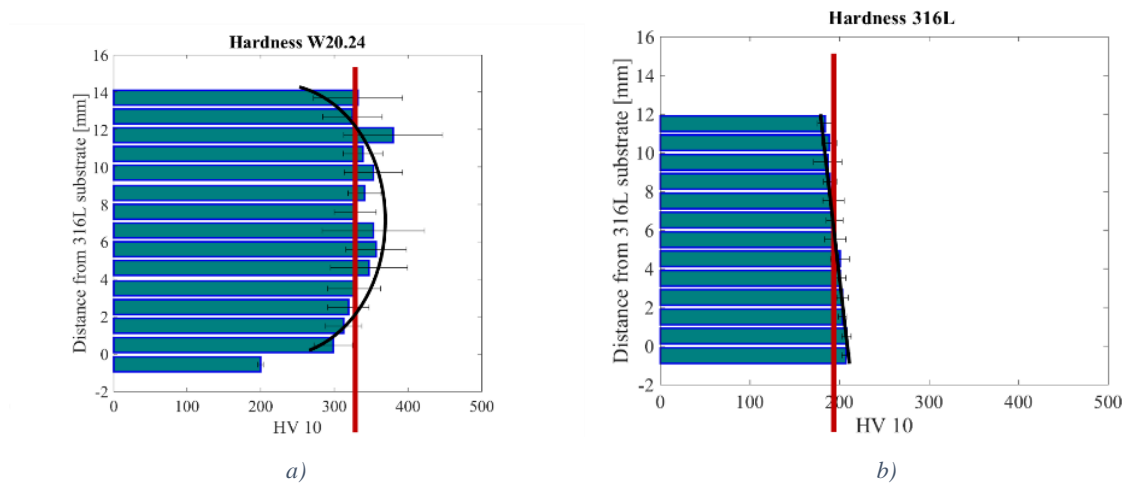
Figure 4-32: Hardness evolution of the pure SS316L on XZ plane (a),and of the section on XZ plane (b)

Moreover, it was performed on the section on the XY plane as well.
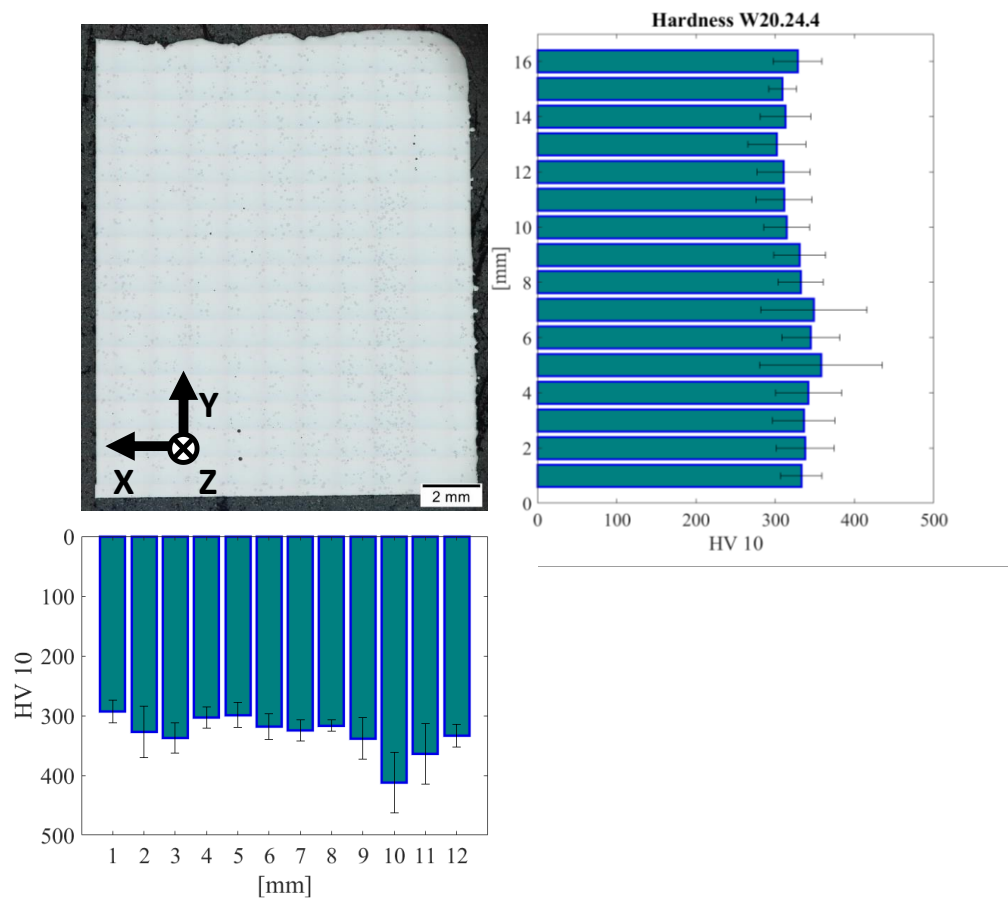
Figure 4-33: Hardness evolution of the section on the XY plane.

In general, the average values of the XY section correspond to the previous XZ section. The values on the Y direction consider 10 different tracks in the layer and are quite homogeneous. On the X direction the average value consider 1 or 2 tracks and it is possible to observe a maximum at 400 HV on the side of the deposit. Nevertheless, considering the first 9 mm fronm the center of the deposit, the average value of the macrohardness is homogeneous here as well.

4.3   Wear tests

4.3.1 Choice of parameters and first tests performed

As said in section 3.5 a couple of tests were performed in order to find the right setup for the tribometer. A sample containing the 15% of WC was used for these preliminary tests. The same parameters used in the past of the High Speed Steels were used (Table 3-4) [93]. The resulting Al_2O_3 ball after these tests was very consumed so it was decided to decrease the sliding speed.

The sample with the 20% of reinforcement tested with the pin-on-disk were the W20.19, W20.14 and the W20.18 (Figure 3-11). It was decided to use the two faces at 6.3mm from the substrate (Figure 3-12) because it was seen (section 4.2) that at that in the middle of the deposit the hardness reaches its maximum value. The tests on different heights are not part of this work.

The first sample analyzed was the W20.19. At 6.3mm it was found a defect in the middle. It was decided to start from these defected faces because the setting of the load and the stop condition had not been decided yet.
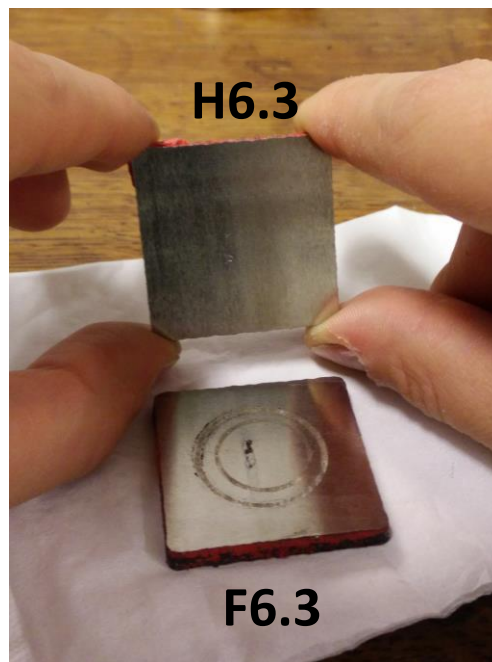
Figure 4-34: W20.19. F6.3 after the wear test, H6.3 before the wear test.

In the following figures are reported the evolution of the friction coefficient (COF) and the penetration depth for the four tests which the parameters are described in Table 3-5. The penetration depth is value that represents how much the pin goes inside the disk.

71

In all the tests show the same development of the friction coefficient and of the penetration depth. Indeed, the graphs can be divided in zones corresponding to different "wear stages". The first stage is characterized by a sudden increase of the friction coefficient. In the second stage the COF increases very slowly. The second stage can be assumed as "stable stage". A certain point, the COF shows a sharp drop. In this phenomenon consists the third stage. Finally, another "stable stage" take place. In the test on W20.19-H6.3 at 8mm shows a second drop of COF. A variation of the penetration depth happens every time the COF shows a sharp modification.
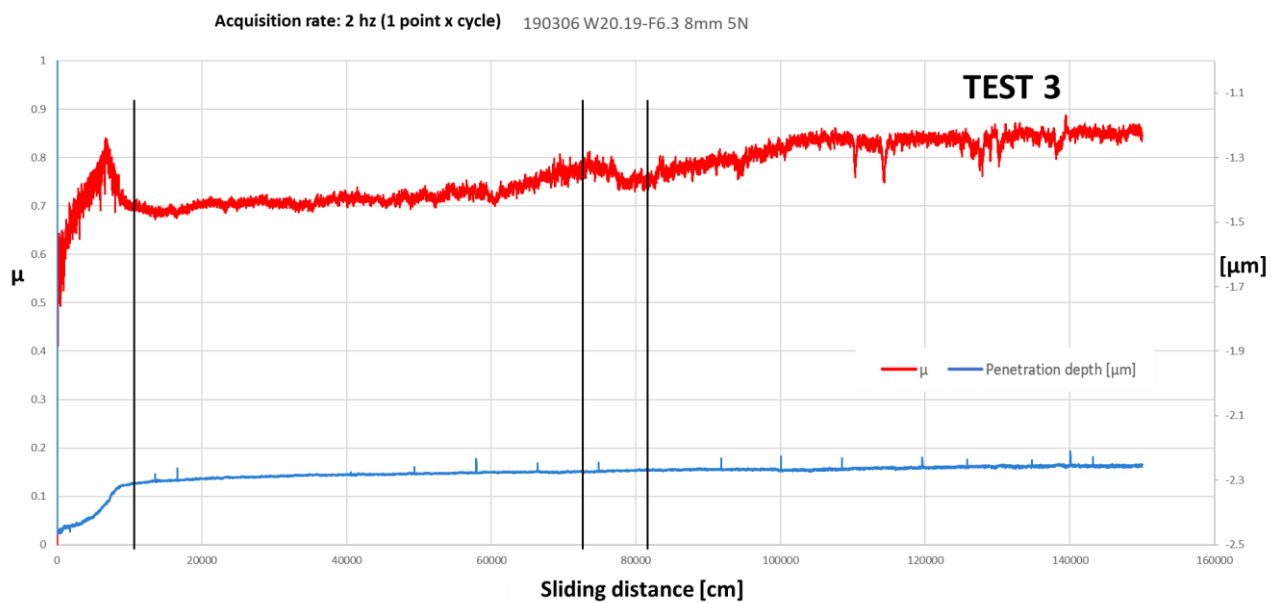
Figure 4-35: Friction coefficient and penetration depth evolution for the W20.19-F6.3 at 8mm..
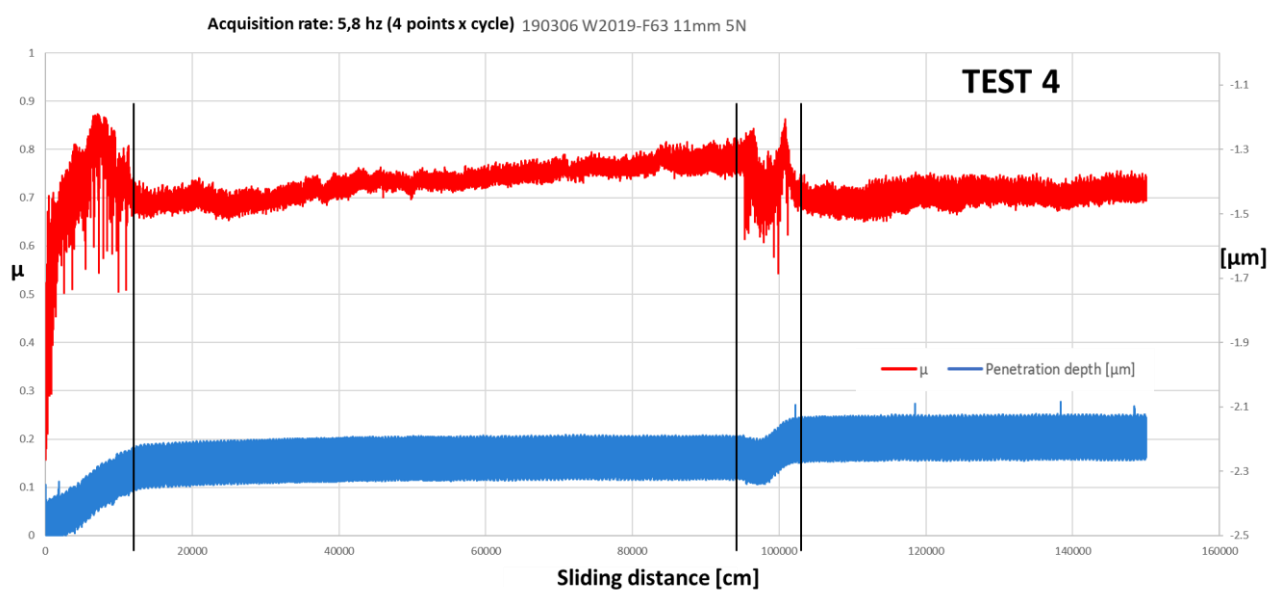
Figure 4-36: Friction coefficient and penetration depth evolution for the W20.19-F6.3 at 11mm.
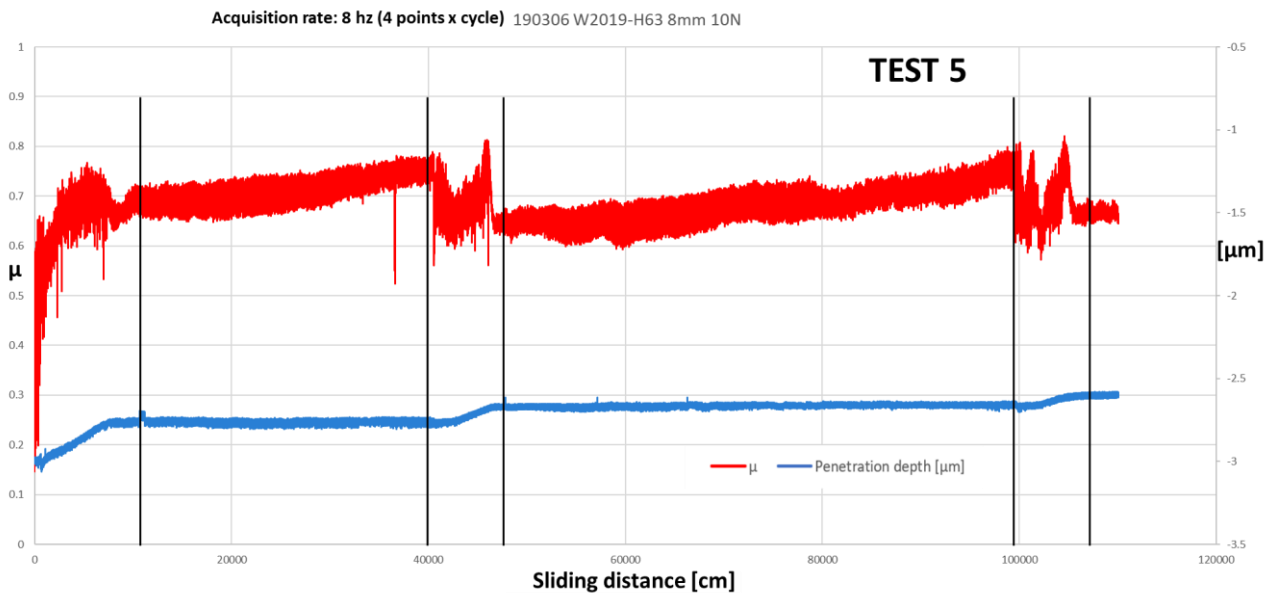
Figure 4-37: Friction coefficient and penetration depth evolution for the W20.19-H6.3 at 8mm.
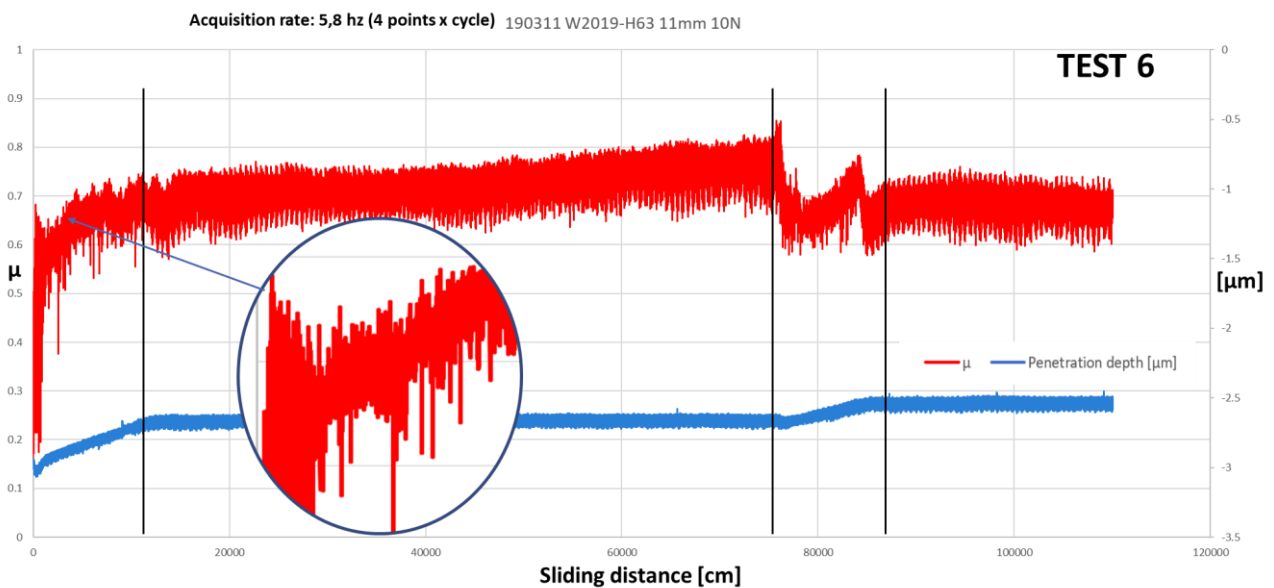
Figure 4-38: Friction coefficient and penetration depth evolution for the W20.19-H6.3 at 11mm.

Considering these results, it was decided to use a load of 10N. Indeed, the two tests performed with this parameter settled show the most similar behavior of the COF. Moreover, the stop condition in meters was changed taking in account the number of the cycles. This way, the different radius does not influence the reproducibility of the results.

All the following results were obtained with the final parameters shown in Table 3-6. Hence, wear tests on the W20.14 F6.3 were carried out.
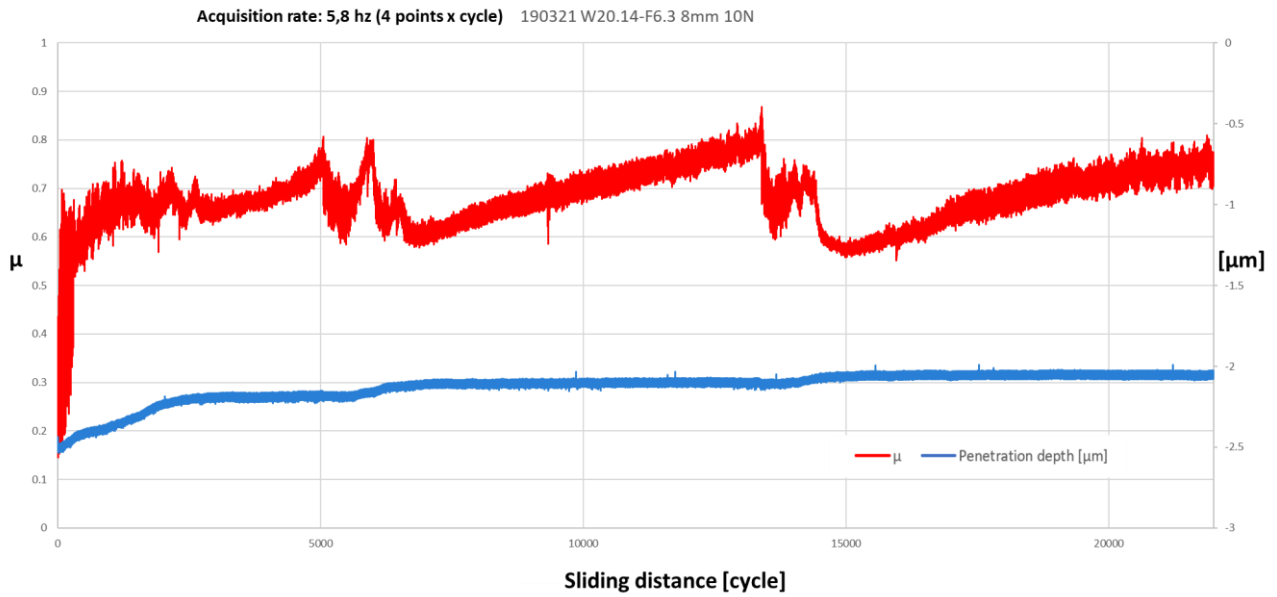
Figure 4-39: Friction coefficient and penetration depth evolution for the W20.14-F6.3 at 8mm.
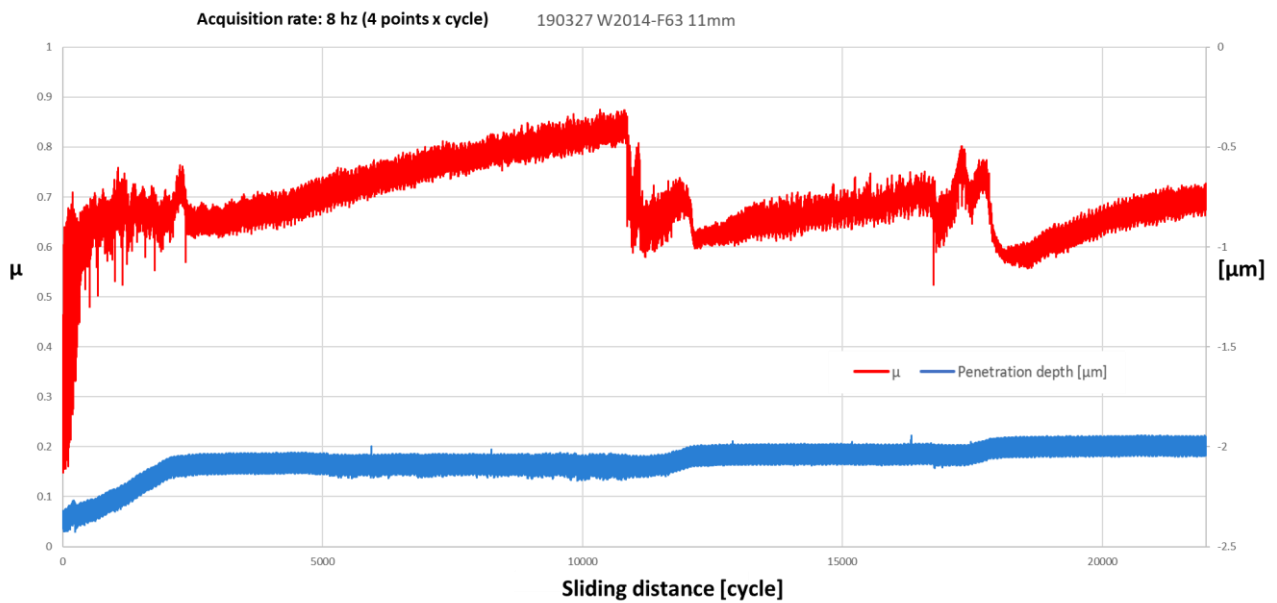
Figure 4-40: Friction coefficient and penetration depth evolution for the W20.14-F6.3 at 11mm.

These two tests performed on a distinct sample shows a slightly different COF evolution in comparison to the previous tests. Nevertheless, they are similar enough to confirm the presence of the stages described previously. Moreover, because the differences are not so big, it can be said that the experiments have a quite high grade of repeatability.

4.3.2 Interrupted tests

The aim of this work is to understand the wear behavior of the material in examination. In order to do that, it was necessary to analyze the samples as best as possible. The observation of the different stages leads the investigation of the phases formed after each one. Indeed, to achieve this purpose some tests were performed. Every test was stopped at the end of each stage of COF evolution (Figure 4-41).
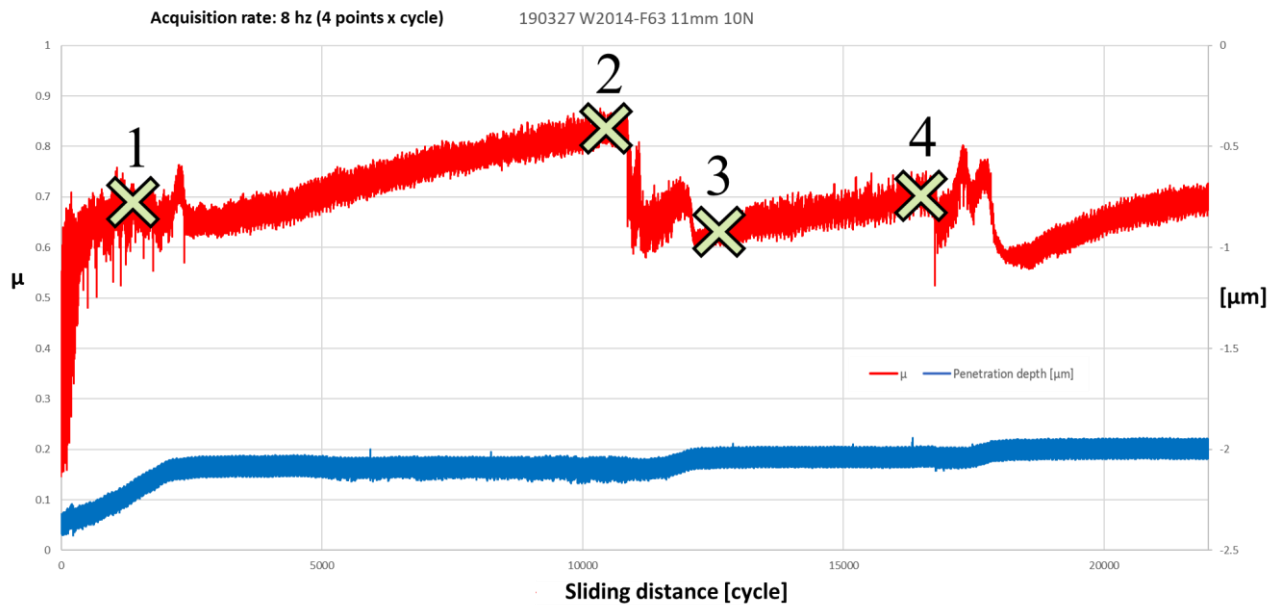
Figure 4-41: Position of the fourth interrupted tests.

Hence, the stop condition in number of cycles, was decided using as references the charts of the previous tests performed. The first two tests were performed on the sample W20.18-F surface, while the other two on the W20.14-H surface. In the following the COF and the penetration depth evolution for each interrupted test, are shown.
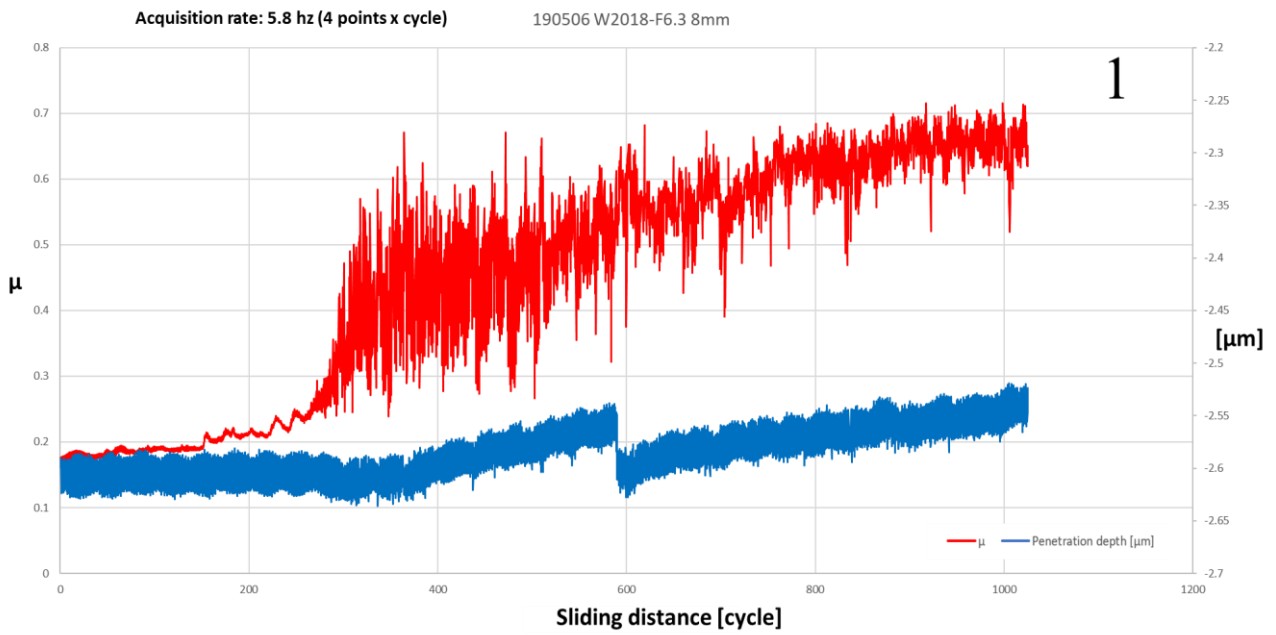
Figure 4-42: First (shortest) interrupted test.
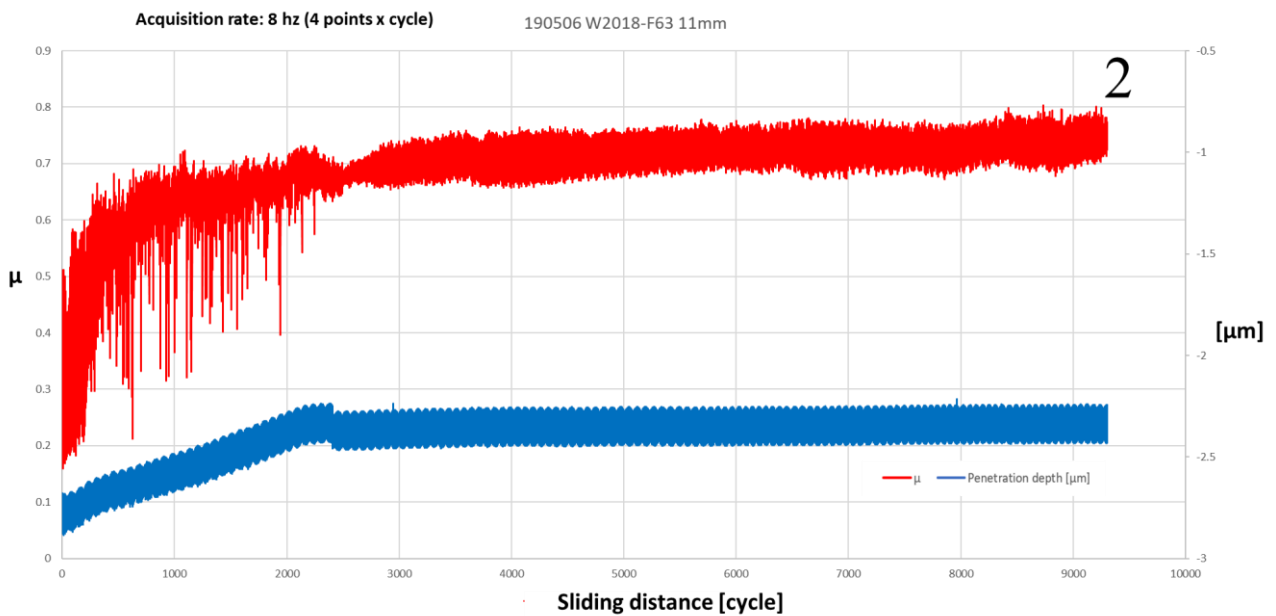
Figure 4-43: Second interrupted test.
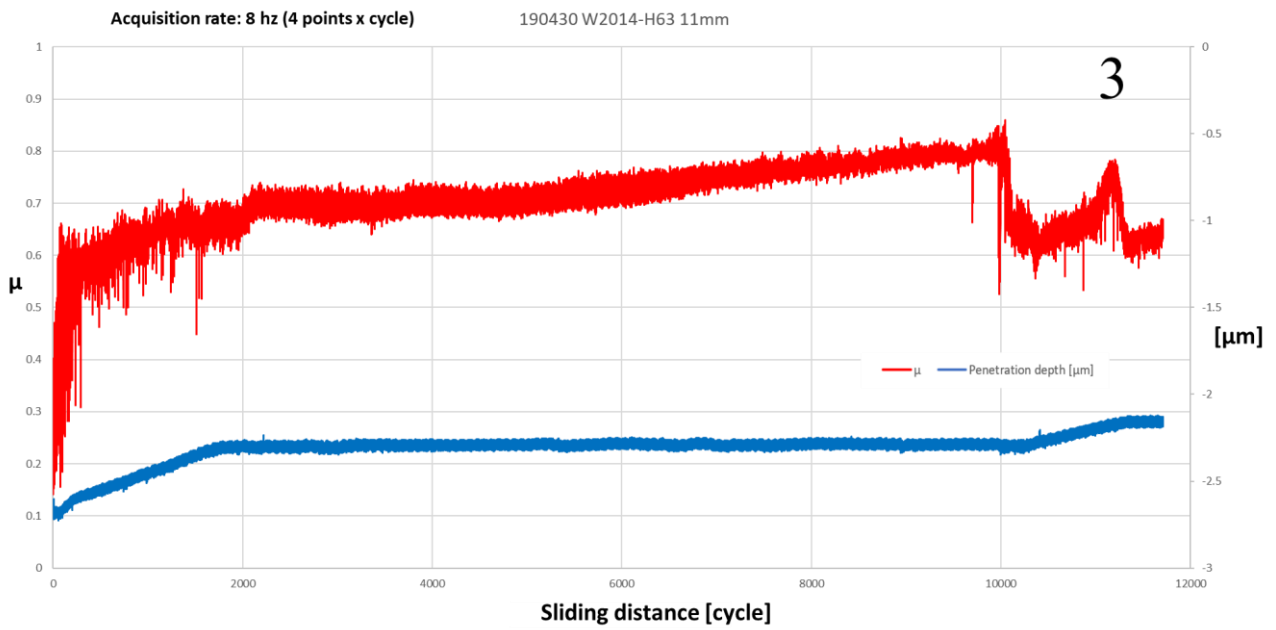
Figure 4-44: Third interrupted test.
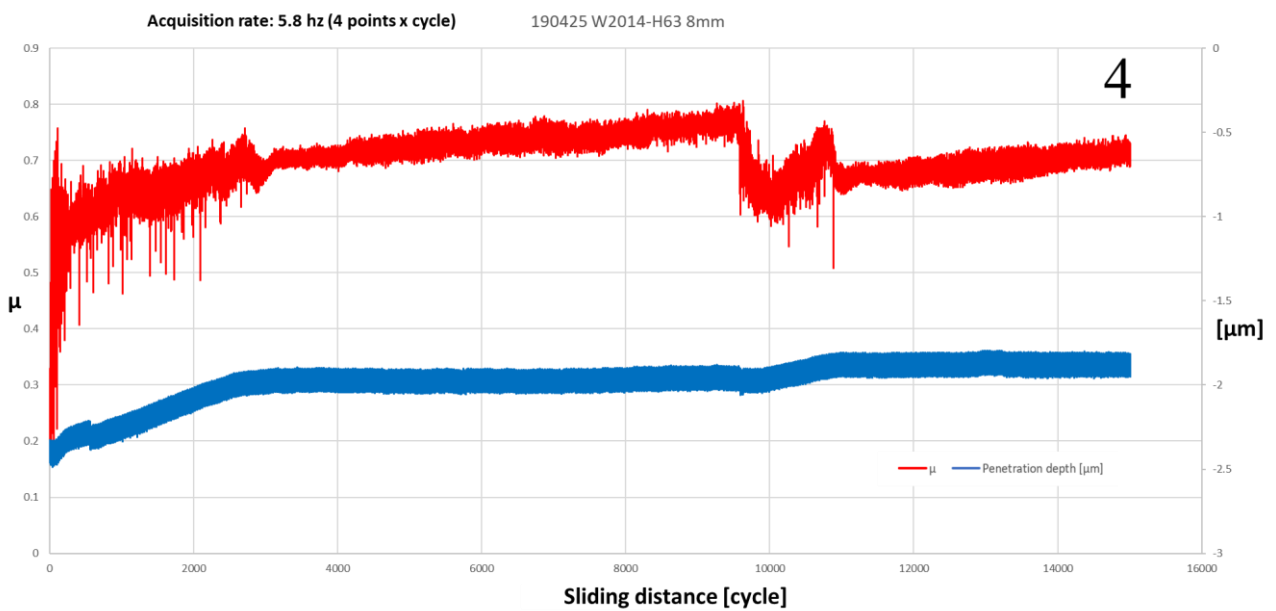
Figure 4-45: Forth interrupted test.

4.3.3 Worn track's analysis

After each test the wear track was evaluated using the profilometer (section 3.6). The overview of each wear track was obtained.
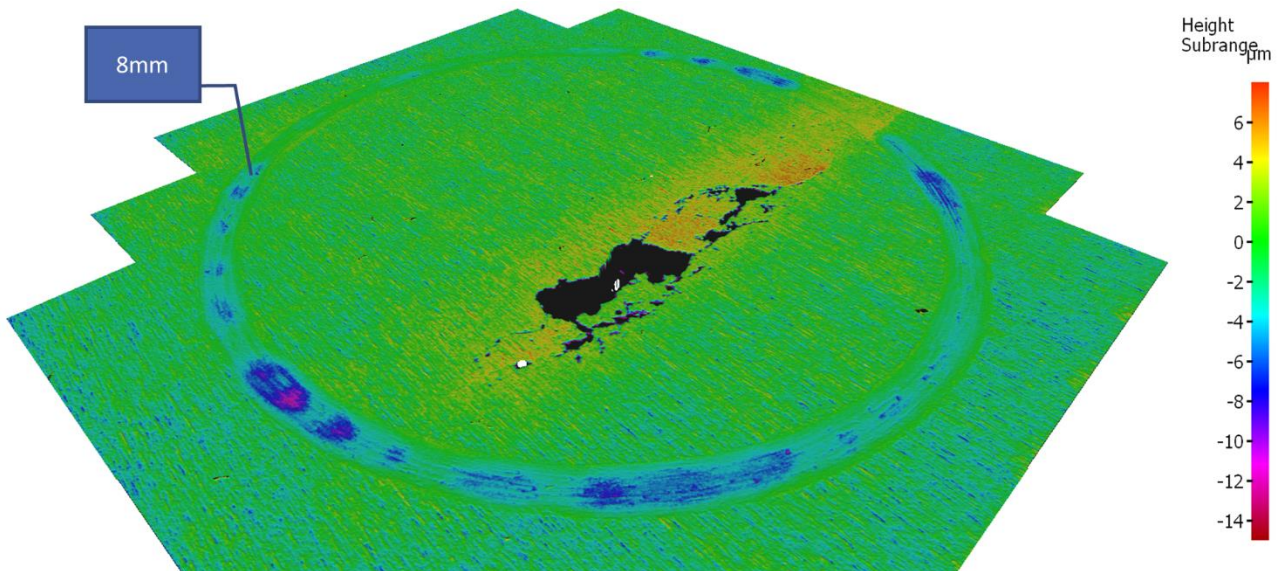
Figure 4-46: W20.19-F6.3 8mm radius 5N force worn track profilometer overview.
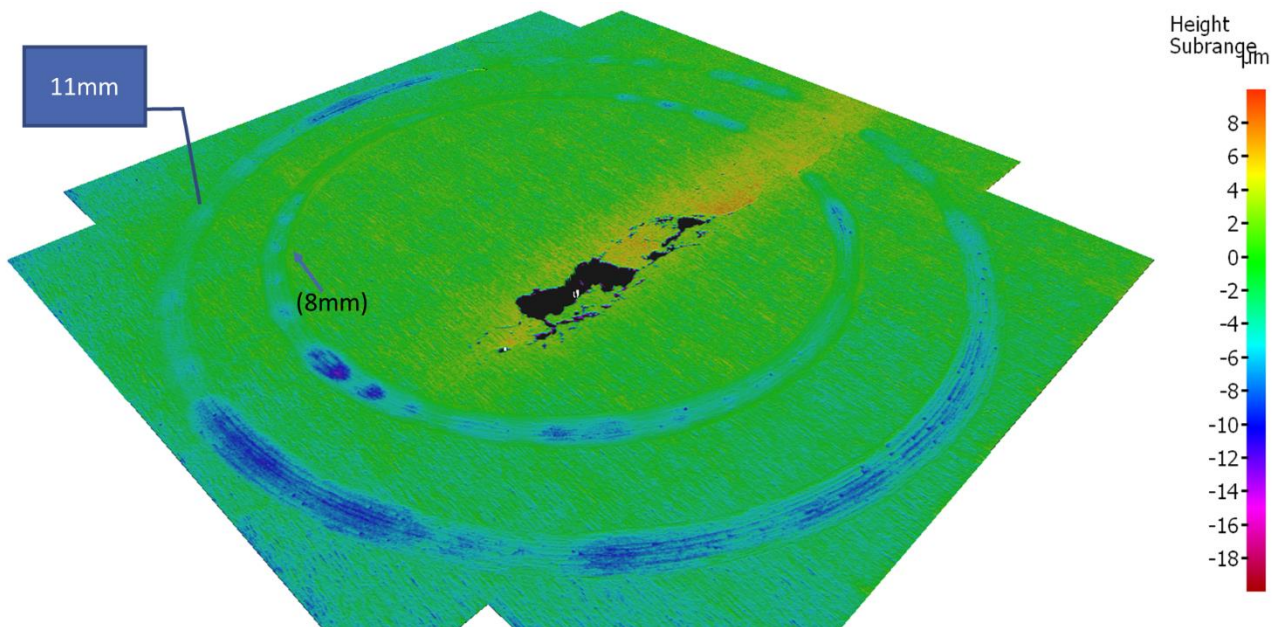
Figure 4-47: W20.19-F6.3 11mm radius 5N force worn track profilometer overview.

In the first two wear tests performed on the same surface, it can be noticed that the samples are not perfectly flat. Indeed, the defect also mentioned in section 4.3.1 is present in the middle of this sample. The following two pictures were obtained from the same height but on the upper surface.

Even here the defect can be noticed but it is less evident. Moreover, the side is slightly higher bringing a less definite track on that zone. The tests were performed with a load of 10N; indeed, the track is more pronounced both on the 8mm radius that on the 11mm radius compared to the two made on the lower surface.
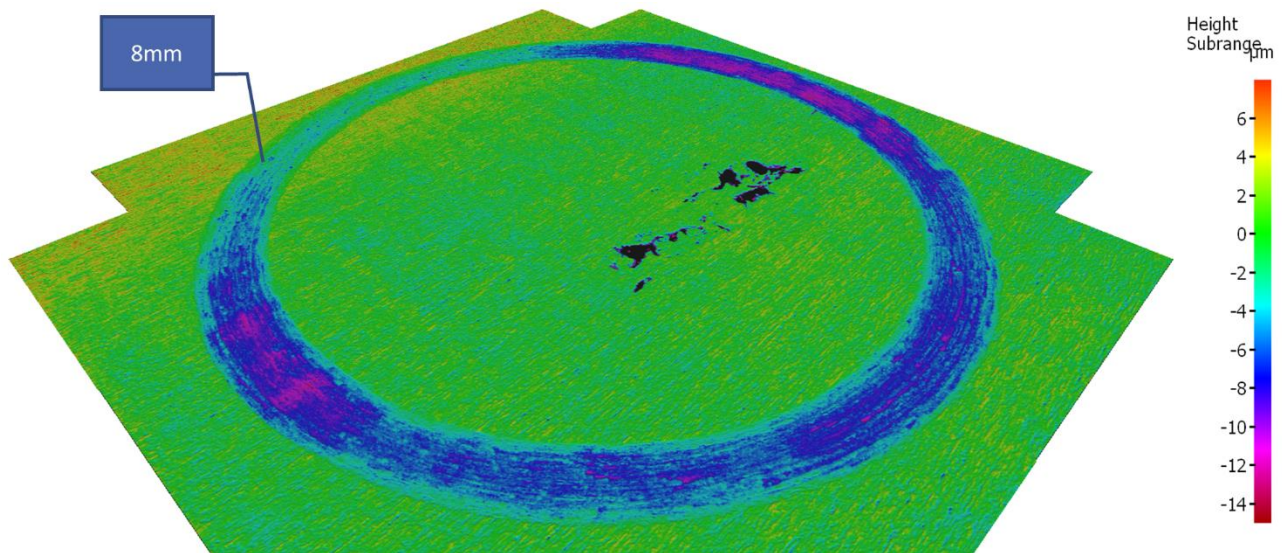
Figure 4-48: W20.19-H6.3 8mm radius 10N force worn track profilometer overview.
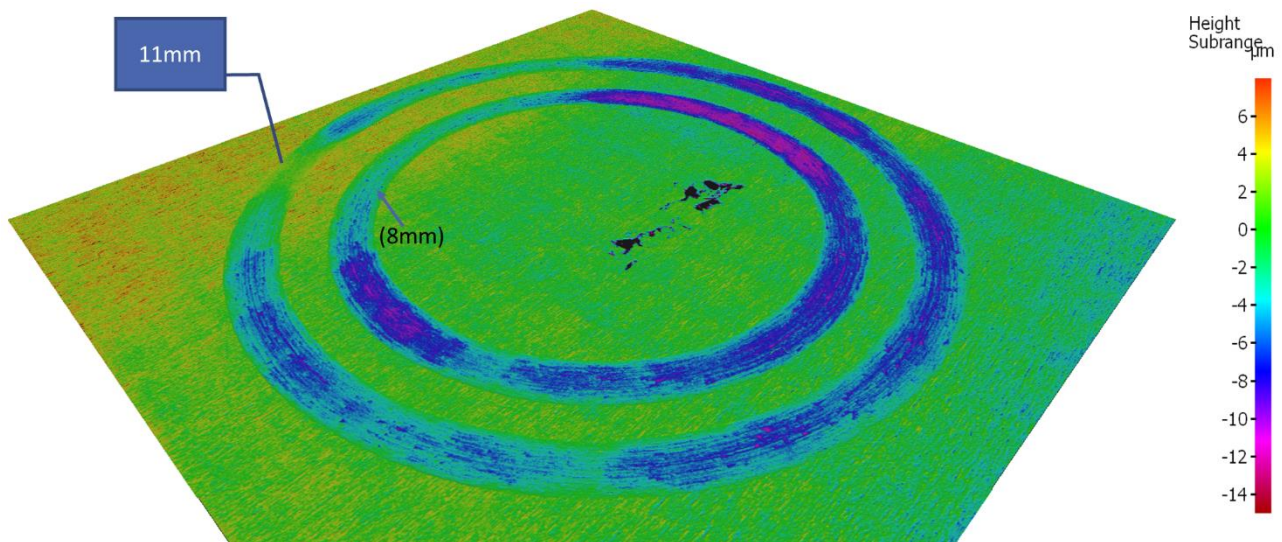
Figure 4-49: W20.19-H6.3 11mm radius 10N force worn track profilometer overview.

The following last two were performed using the final parameters described in Table 3-6. In this case the surface was almost flat indeed the tracks are more homogeneous.
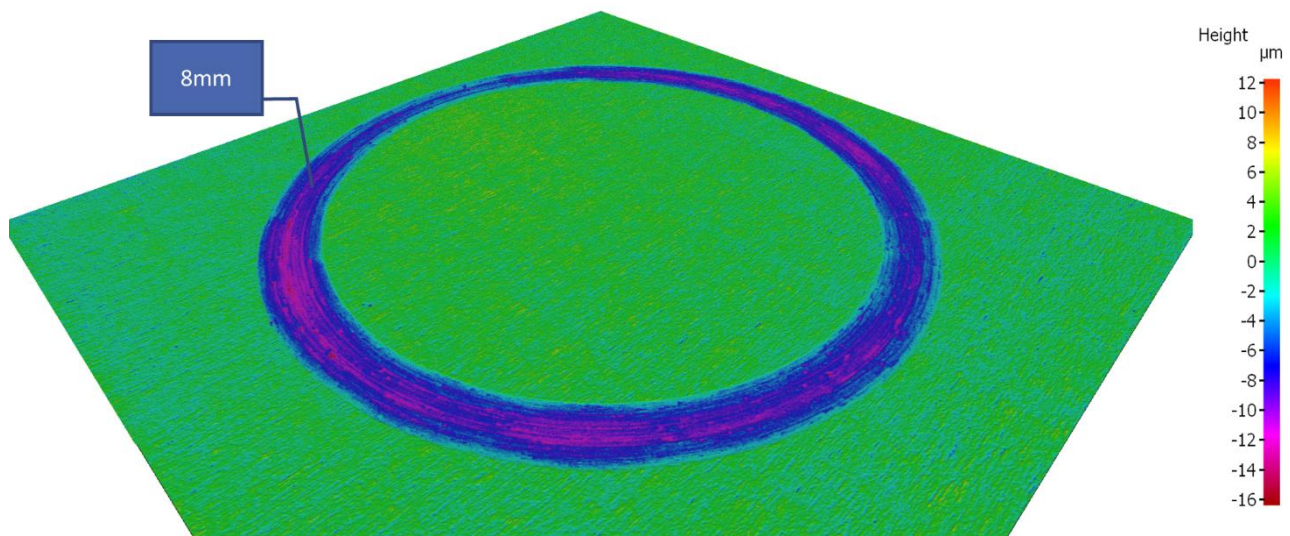
Figure 4-50: W20.14-F6.3 8mm radius 10N force worn track profilometer overview.
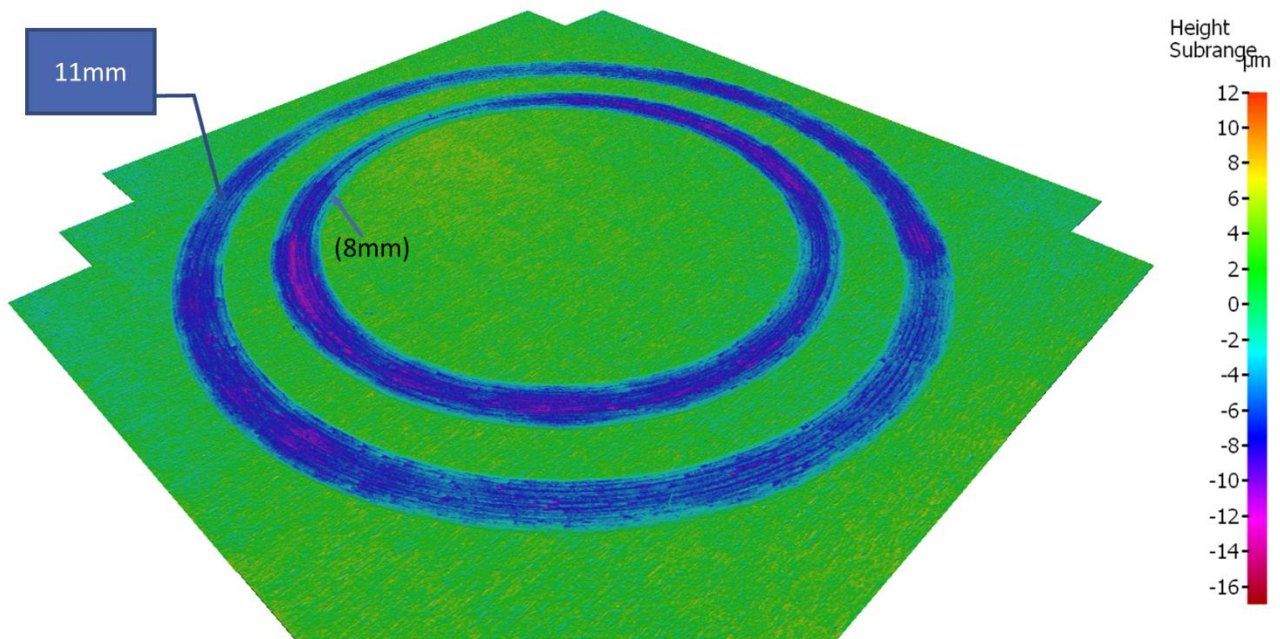
Figure 4-51: W20.14-F6.3 11mm radius 10N force worn track profilometer overview.

As settled before (4.3.1), after the tests for the setup of the tribometer and another two tests to check the good repeatably of the tests, the interrupted tests were carried out. The tracks of each are reported in the following.
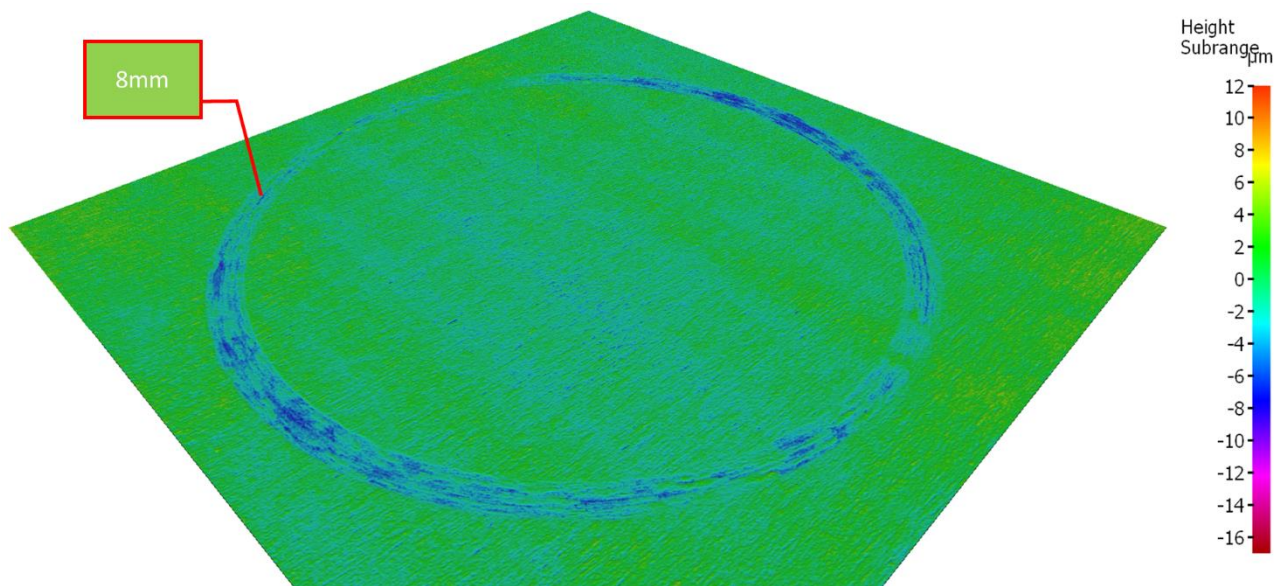
Figure 4-52: W20.18-F6.3 8mm radius 10N force worn track profilometer overview.

The shorter test leads to a track that is very shallow.
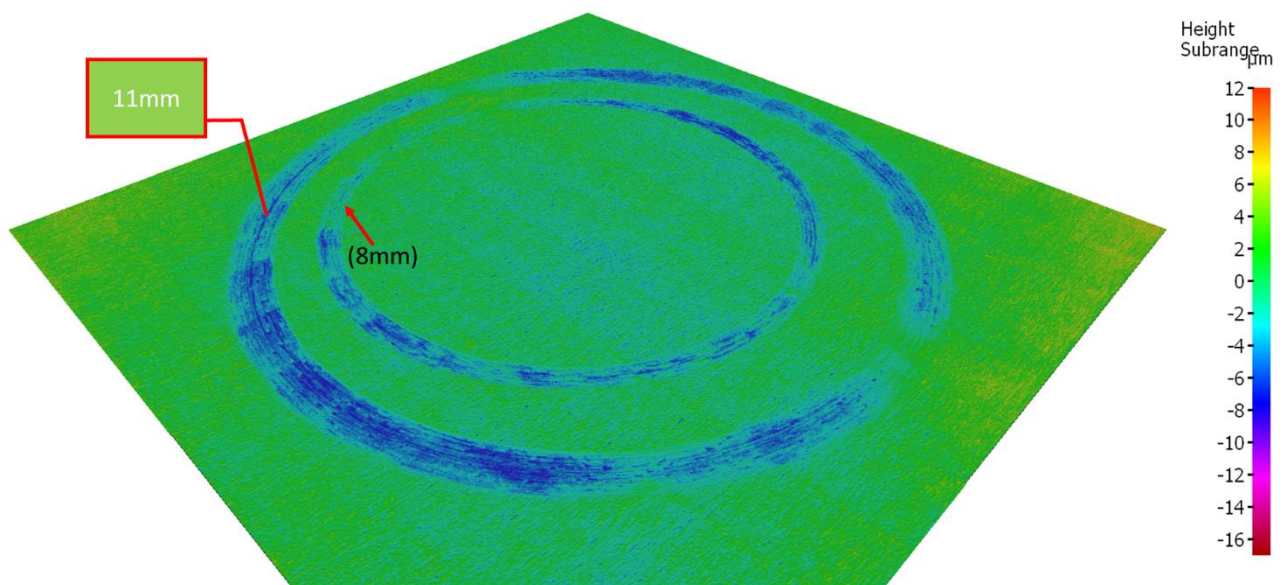
Figure 4-53: W20.18-F6.3 11mm radius 10N force worn track profilometer overview.

The second test, made on the same surface of the shorter but at 11mm radius, brings to a slightly deeper track.
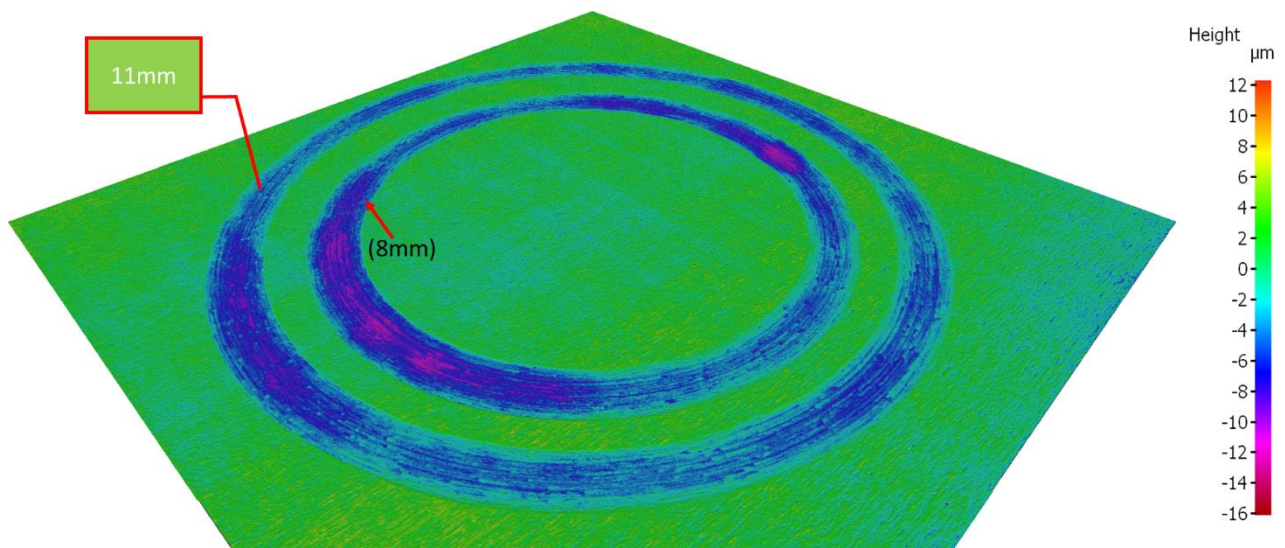
Figure 4-54: W20.14-H6.3 11mm radius 10N force worn track profilometer overview.
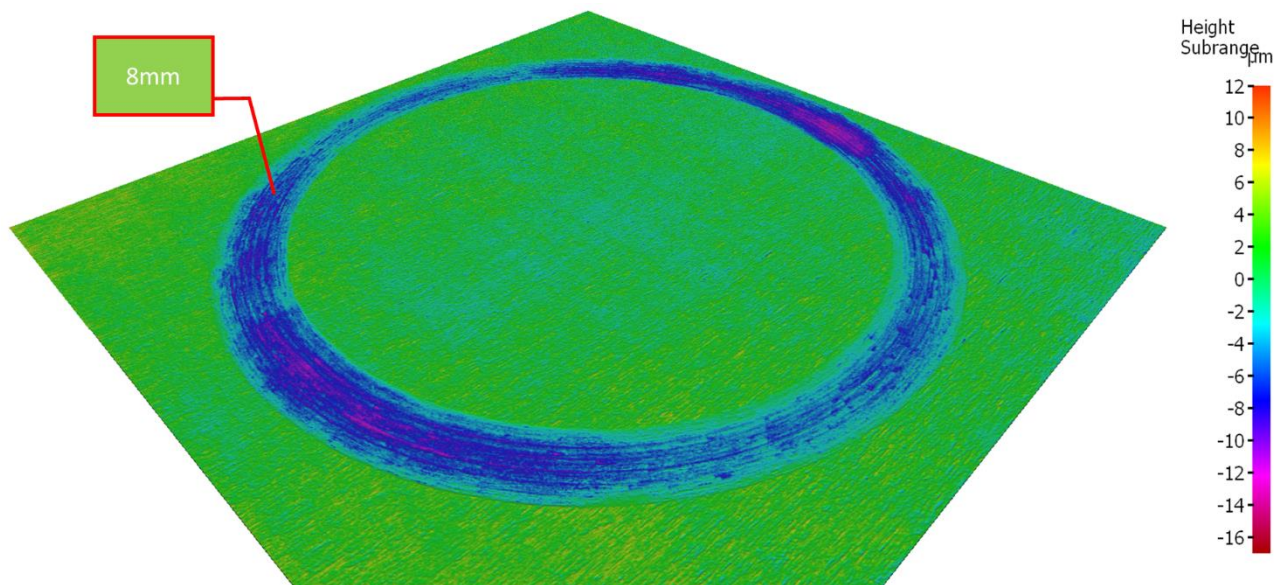
Figure 4-55: W20.14-H6.3 8mm radius 10N force worn track profilometer overview.

The last two, performed on another sample, are the longest interrupted tests. Indeed, the tracks are deeper.

Noticing punctual hollows on the Figure 4-51, the track was observed also using a higher magnification (Figure 4-56) in order to investigate the nature of those zones.
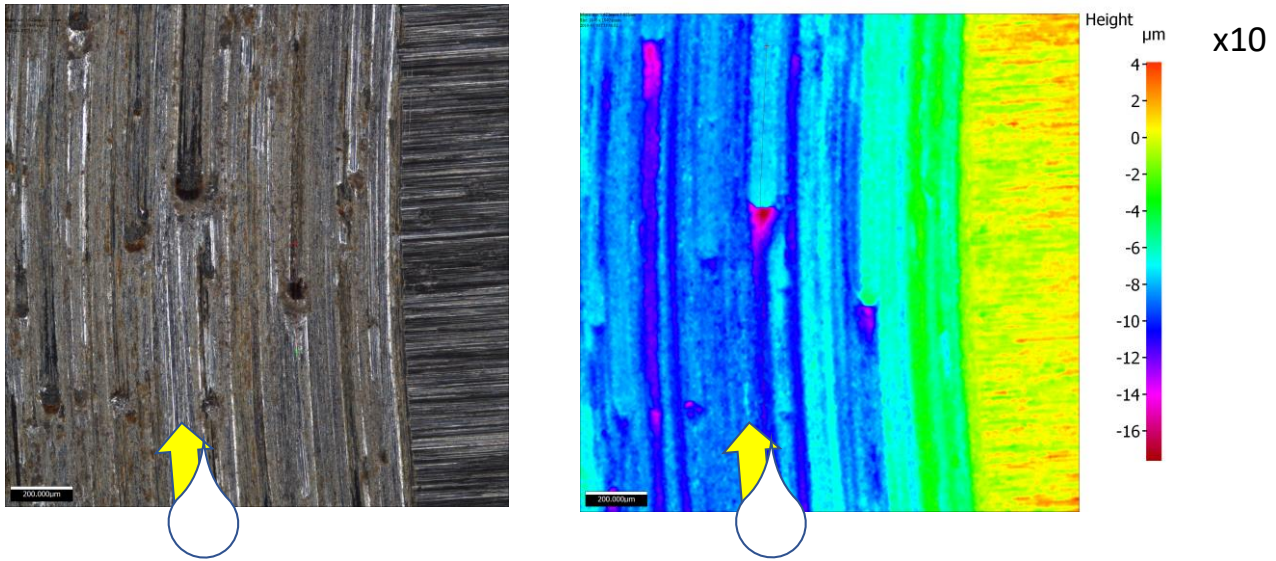
Figure 4-56: Detail on the track.

A deeper zone just in front of the carbides can be noticed.

4.3.3.1 Worn track estimation

The average depth of the track was evaluated using profilometer measures along the depth and the circular profile tool, allowing to measure the average value of the depth on a circular shape. Moreover, it was decided to design linear horizontal and vertical profiles in order to see the variation of the depth across the whole sample. Finally, a short linear profile was carried out on a zone of the track where the depth has an average value from the previous measure. This last step was done to have a specific measure of the wear track. In the following the most relevant results are illustrated:
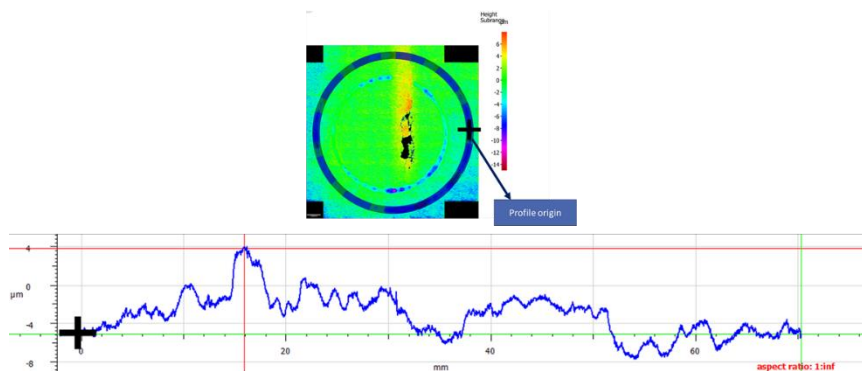
Figure 4-57: Circular profile on W20.19-F6.3 11mm radius 5N force worn track.
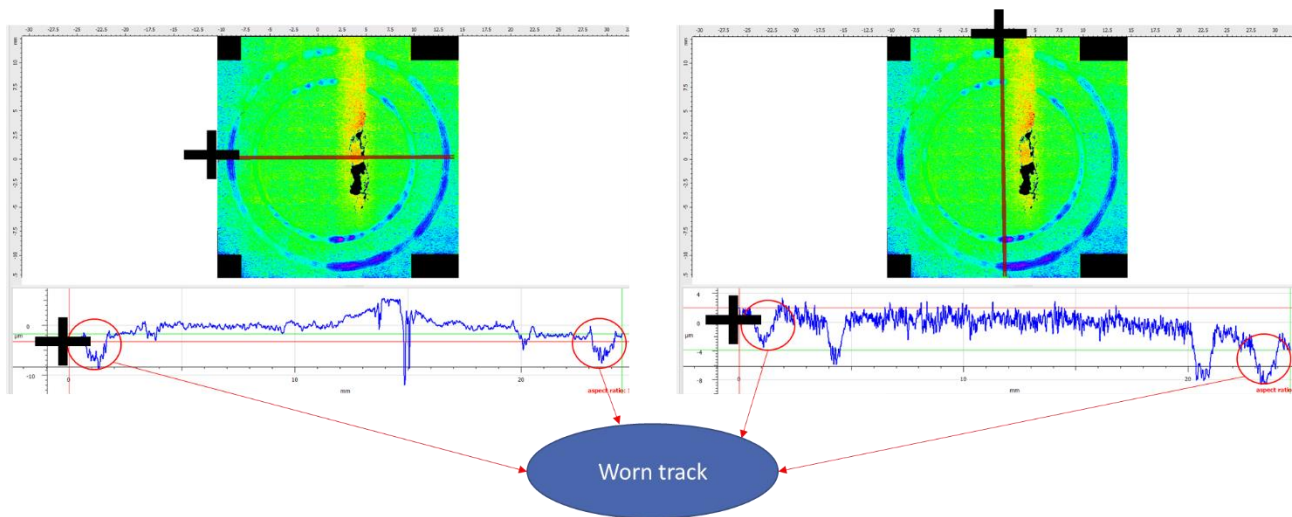
Figure 4-58: Horizontal (left) and vertical (right) profile on W20.19-F6.3 11mm radius 5N force worn track.
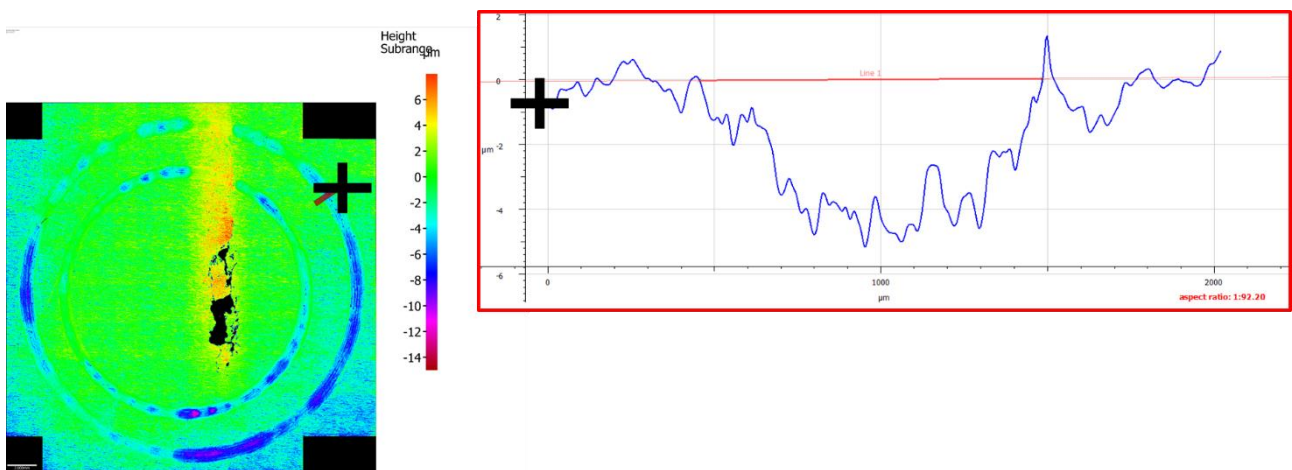
Figure 4-59: Short linear profile on W20.19-F6.3 11mm radius 5N force worn track.

Table 4-6: Measurements of the short linear profile on W20.19-F6.3 11mm radius 5N force worn track.

Max depth [µm]	Width [mm]
5.2	1.03
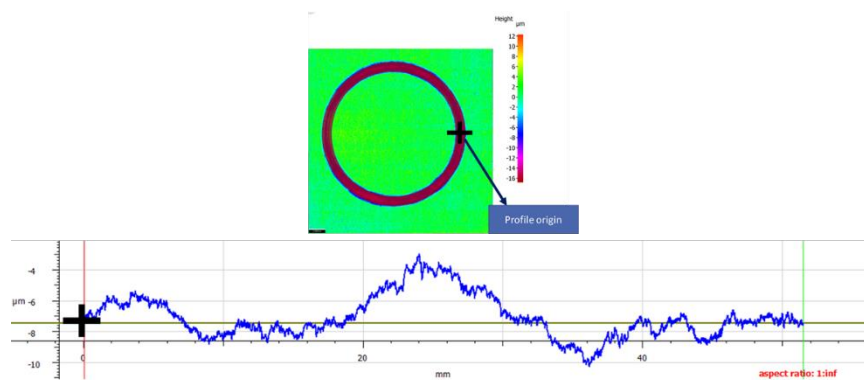
Figure 4-60:Circular profile on W20.14-F6.3 8mm radius 10N force worn track.

84
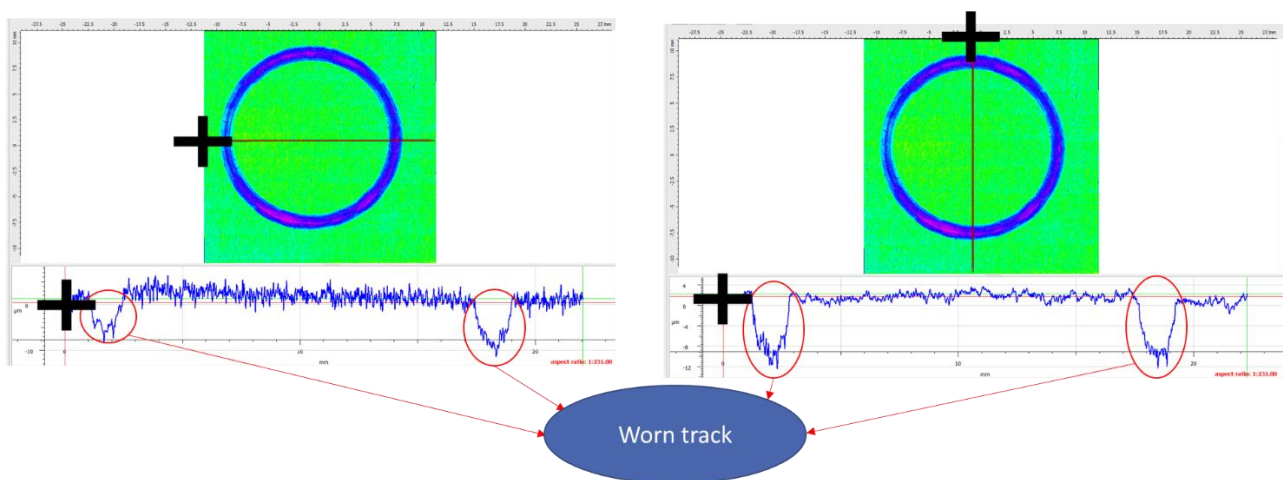
Figure 4-61: Horizontal (left) and vertical (right) profile on W20.14-F6.3 8mm radius 10N force worn track.
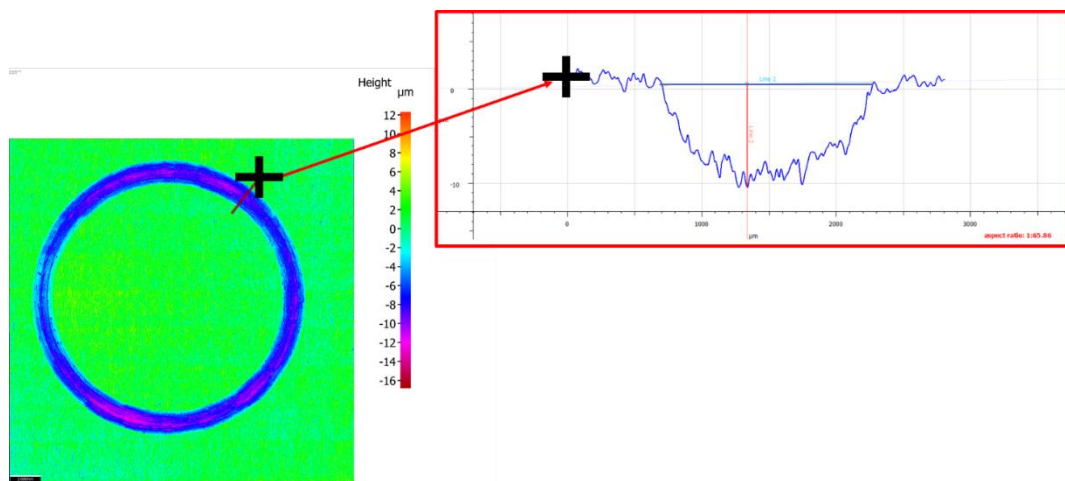
Figure 4-62: Short linear profile on W20.14-F6.3 8mm radius 10N force worn track.

Table 4-7: Measurements of the short linear profile on W20.14-F6.3 8mm radius 10N force worn track.

Max depth [μm]	Width [mm]
9	1.8

The same method described at the beginning of this chapter was used to measure the wear tracks of the interrupted tests too. As example, the results on the first interrupted test is illustrated in the following:
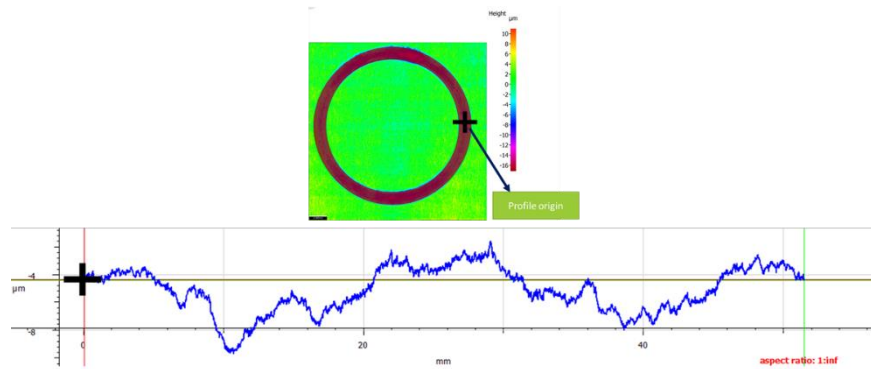
Figure 4-63: Circular profile on W20.18-F6.3 8mm radius 10N force worn track.
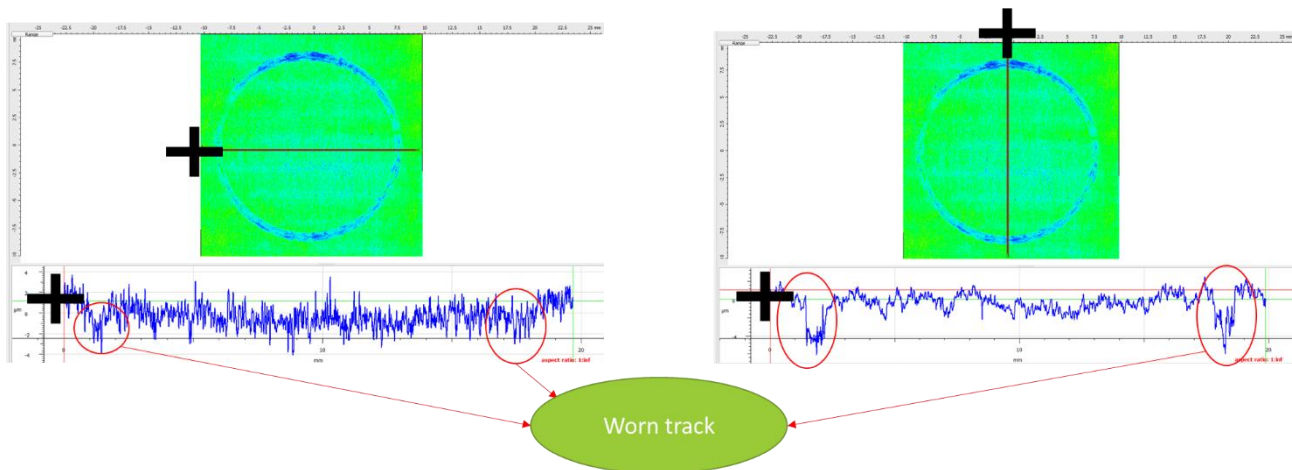
Figure 4-64: Horizontal (left) and vertical (right) profile on W20.18-F6.3 8mm radius 10N force worn track.
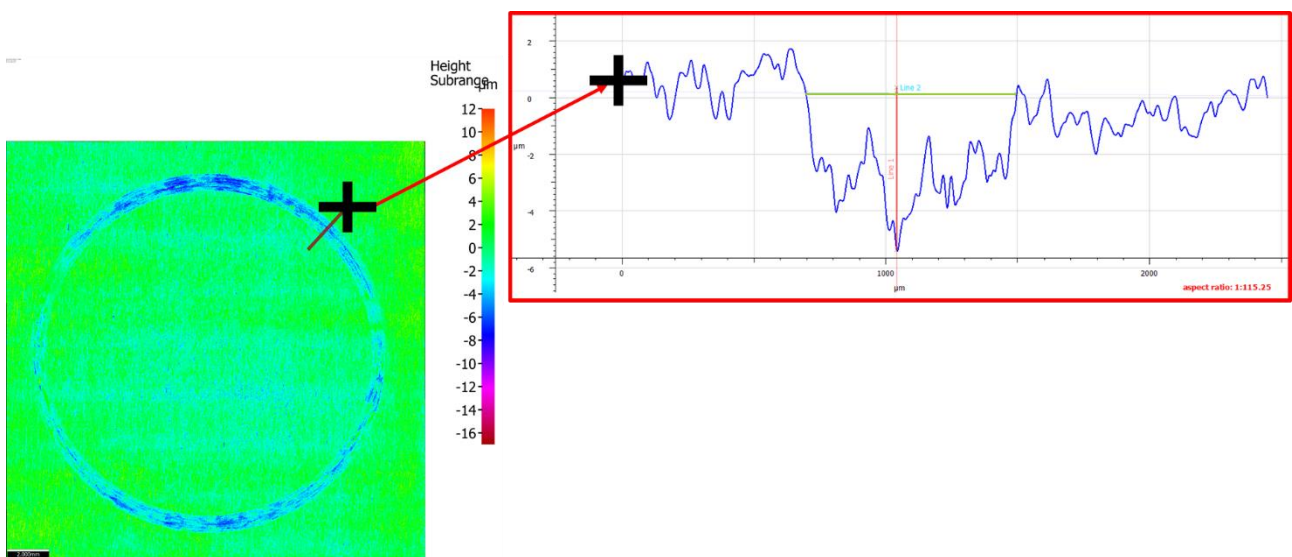
Figure 4-65: Short linear profile on W20.18-F6.3 8mm radius 10N force worn track.

Max depth [μm]	Width [mm]
5.7	0.8

In order to have a general overview of the data, the different measures obtained from the tracks are reported in Table 4-9. A better look of the results is given by the Figure 4-66 where the different measures obtained from the tracks are plotted on against the number of cycles of the relative test. The preliminary tests are not included. As expected, the values increase at the increase of the number of cycles for the same tested surface.

Table 4-9:Track measurements resuming table.

TEST	Track depth [μm]	Track width [mm]
W20.18-F6.3 8mm 10N	5.7	0.8
W20.18-F6.3 11mm 10N	5.87	1.62
W20.14-H6.3 11mm 10N	8.9	1.75
W20.14-H6.3 8mm 10N	10	1.8
W20.14-F6.3 8mm 10N	9	1.8
W20.14-F6.3 11mm 10N	9.5	1.6
W20.19-F6.3 8mm 5N	7	1
W20.19-F6.3 11mm 5N	5.2	1.03
W20.19-H6.3 8mm 10N	8.1	1.78
W20.19-H6.3 11mm 10N	9	1.76
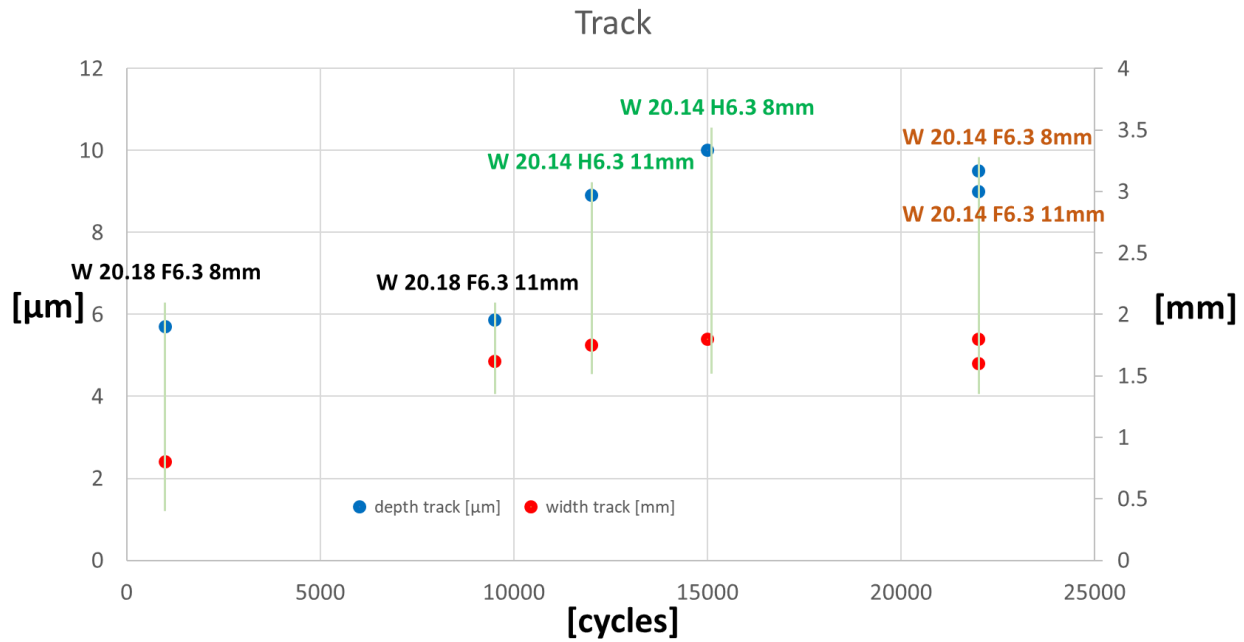
Figure 4-66: Resuming chart. Track depth (left axis) and track width (right axis) in function of the number of cycles.

4.3.4 Worn Alumina ball's analysis

The wear tests did not lead only to a formation of a track; even the counter body was consumed. After each test, the dimensions of the alumina ball were evaluated using the profilometer. To overcome the problem of the light reflection (described in section 3.6), a circle fitting based on the portion of not-consumed alumina ball was performed. In this way it was possible to have a quantitative comparison between the virgin ball and the after-test one. Some results are reported in the following images.
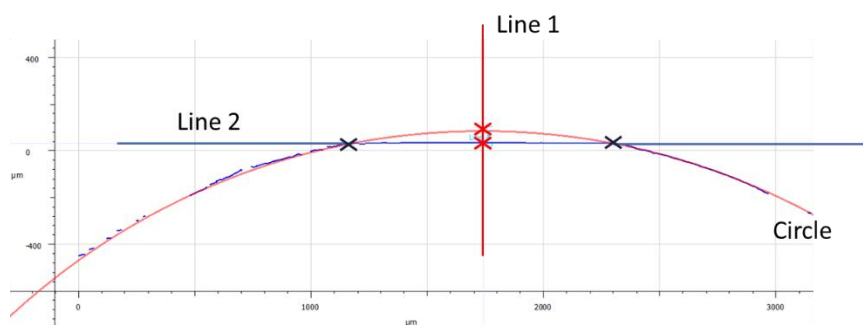
Figure 4-67: Al$_2$O$_3$ BALL after W20.19-F6.3 11mm 5N.

Table 4-10: Measurements on Al$_2$O$_3$ BALL after W20.19-F6.3 11mm 5N.

Circle radius [mm]	Line 1 (depth) [μm]	Line 2 (width) [μm]
3	49.3	1100
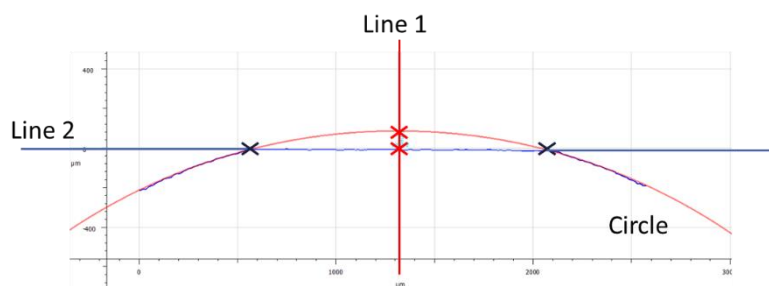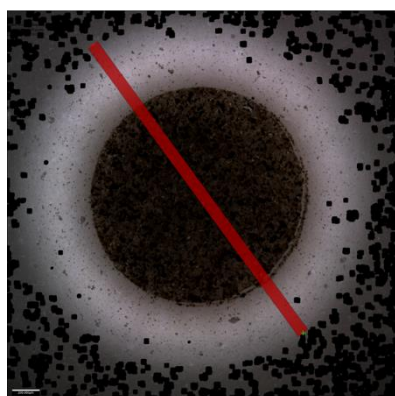
Figure 4-68: Al$_2$O$_3$ BALL after W20.14-F6.3 8mm 10N.

Table 4-11: Measurements on Al$_2$O$_3$ BALL after W20.14-F6.3 8mm 10N.

Circle radius [mm]	Line 1 (depth) [μm]	Line 2 (width) [μm]
3.02	95	1502

The measurements on the alumina ball were performed also after the interrupted tests. Only the results of the first interrupted test are illustrated.
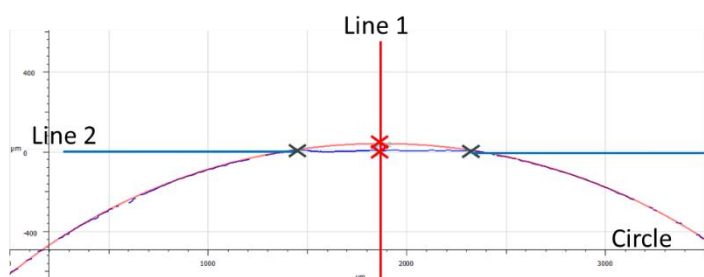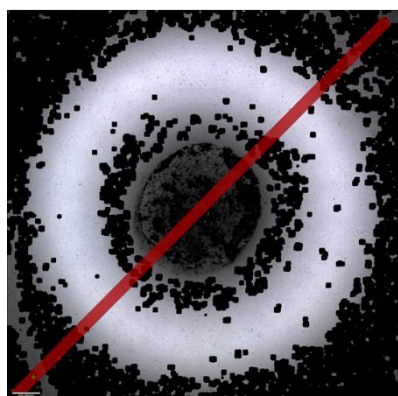
Figure 4-69: Al$_2$O$_3$ BALL after W20.18-F6.3 8mm 10N.

Table 4-12: Measurements on Al$_2$O$_3$ BALL after W20.18-F6.3 8mm 10N.

Circle radius [mm]	Line 1 (depth) [μm]	Line 2 (width) [μm]
3	36	880

As done for the tracks consideration, in order to have a general overview of the data, the different measures obtained from the alumina balls are reported in Table 4-13.

Table 4-13: Al$_2$O$_3$ measurements resuming table.

TEST	Ball depth [μm]	Ball worn surface width [mm]
W20.18-F6.3 8mm 10N	36	0.9
W20.18-F6.3 11mm 10N	108	1.61
W20.14-H6.3 11mm 10N	120	1.68
W20.14-H6.3 8mm 10N	125	1.74
W20.14-F6.3 8mm 10N	95	1.5
W20.14-F6.3 11mm 10N	95	1.5
W20.19-F6.3 8mm 5N	44.8	1.05
W20.19-F6.3 11mm 5N	49.3	1.1
W20.19-H6.3 8mm 10N	103	1.6
W20.19-H6.3 11mm 10N	95	1.5

Moreover, they are plotted on Figure 4-70 against the number of cycles of the relative test to see better the evolution of the wear resulting on the ball. The preliminary tests are not included.
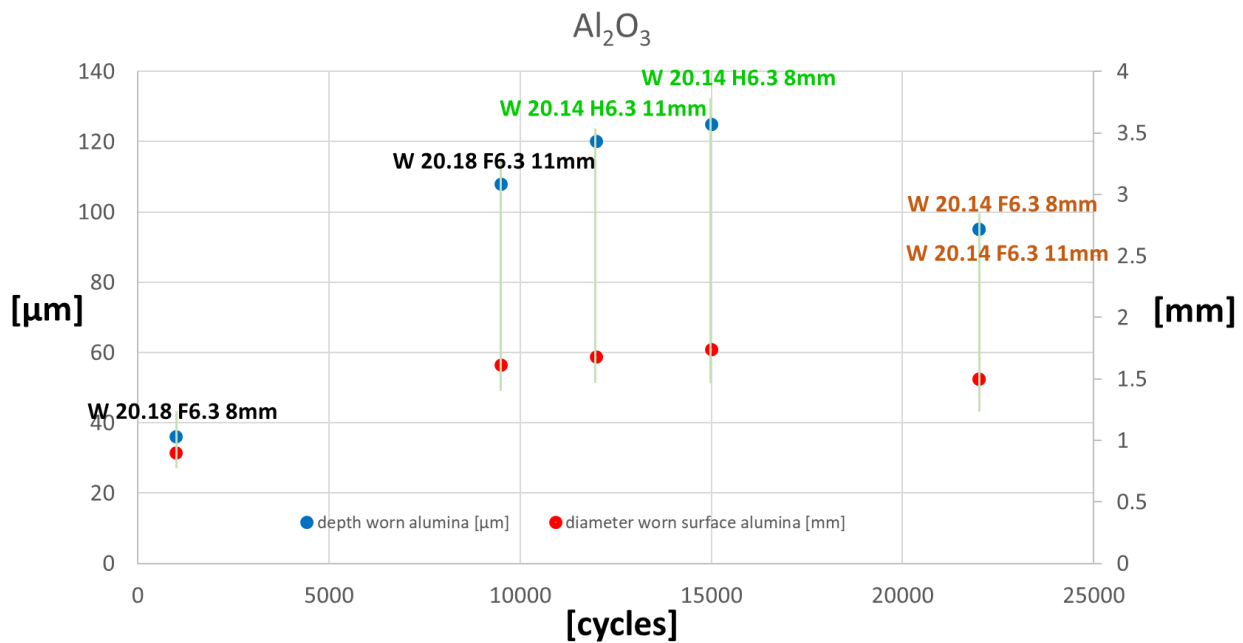
Figure 4-70: Resuming chart. Worn Alumina depth (left axis) and worn surface diameter (right axis) in function of the number of cycles.

The dimensions of the worn ball were plotted also in function of the distance covered during each test (Figure 4-71). As in the case of the previous results on the worn tracks (Figure 4-66), the worn volume from the alumina ball increase at the increase of the number of cycles.
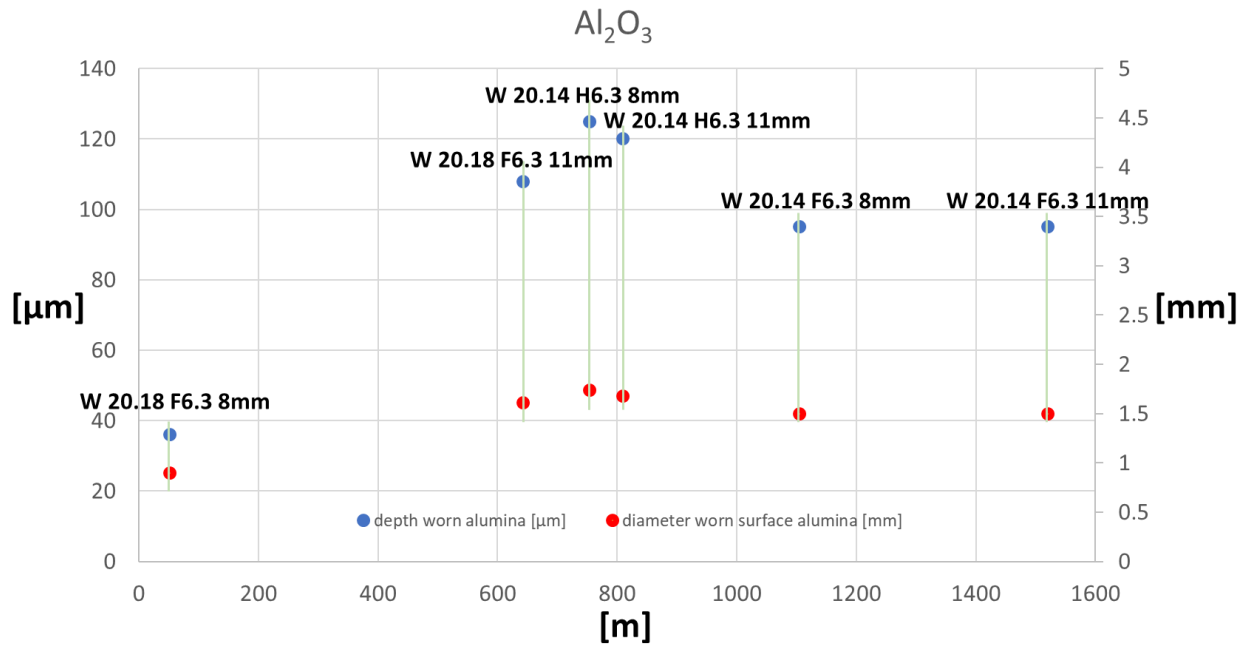
Figure 4-71: Resuming chart. Worn Alumina depth (left axis) and worn surface diameter (right axis) in function of the distance.

4.3.5 SEM images

The wear samples were analyzed by the Scanning Electron Microscope (SEM) before and after the pin-on-disc tests. The initial condition of the sample is shown in Figure 4-72.
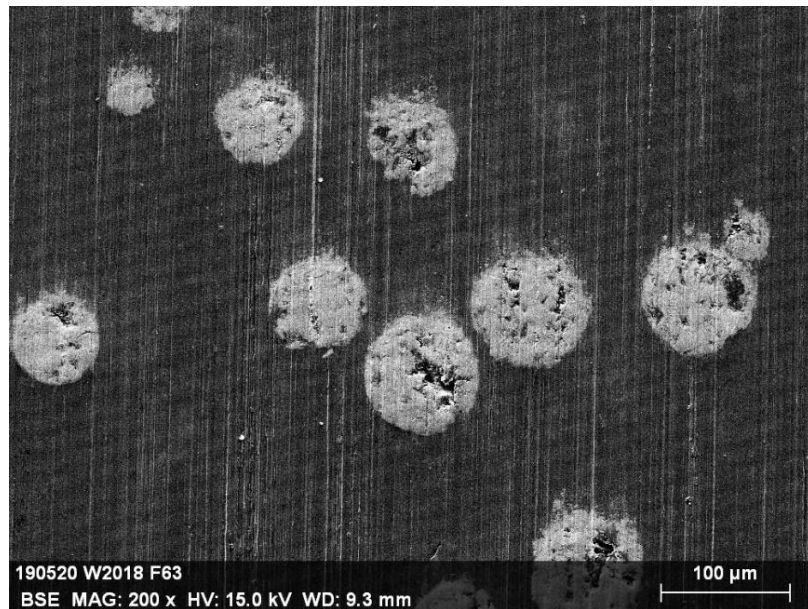
Figure 4-72: Tungsten carbides outside the worn track.

The polishes surface presents some scratches caused by the grinding process. The carbides dispersed in the matrix are not possible to be observed. It is interesting to focus on the describing of the original partially melted tungsten carbides (WC). In Figure 4-72 many WC are present and most of them have a diameter of more or less 70/80µm (as reported in section 4.1). Some WC seem to be already fractured, meanwhile others are intact.

Several images were carried out along the worn track on the post-mortem samples. Many different peculiar zones where detected, often just in few samples. Many different statuses of the surface were found and observed. Some common examples are fractured layers in Figure 4-74, several grooves in front of the WC giant carbides in Figure 4-84, stacking of material in front of the carbides (Figure 4-85) and fractured carbides (Figure 4-86) can be observed. Large attention was played especially on the interrupted tests since each wear step observed on the µ-cycles plot could lead to the different phenomena.

Firstly, the SEM investigation was based on the sample with the big hole in the middle.
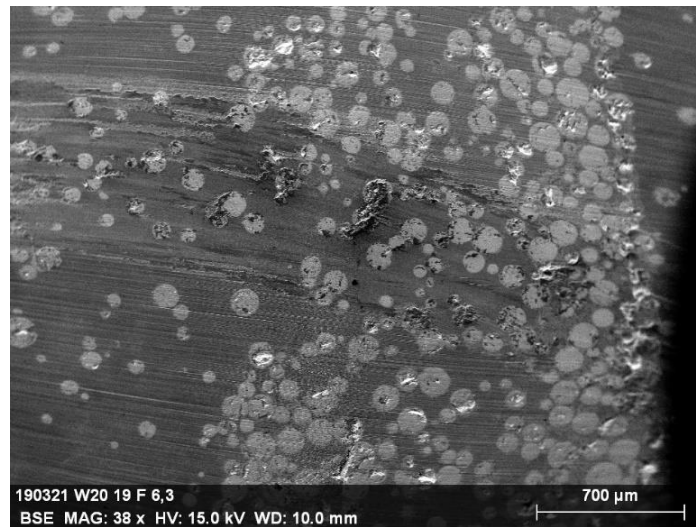
Figure 4-73: Detail of W20.19-F6.3 radius worn track (5N applied force).

As it can be seen in Figure 4-73, a massive concentration of carbides is found near the defect shown in Figure 4-34. Probably during the grinding of the sample, the zone corresponding to the actual hole, pulled out since it was too fragile. The near zone rich of WC, is slightly higher respect the rest of the sample (Figure 4-46) and it resisted very well to the wear test. This heterogeneity was found only in the sample W20.19, at this particular height.

4.3.5.1 First interrupted test (~1000cycles)

The first interrupted test was performed on the sample W20.18-F6.3 at 8mm radius. It was stopped very early, at more or less 1000cycles (the longest of the interrupted test sustain more than 15000 cycles). The typical scenario along the track formed during this test, is the one reported in Figure 4-74. From that images, the presence of a heterogeneous layer on the wear track is detected.
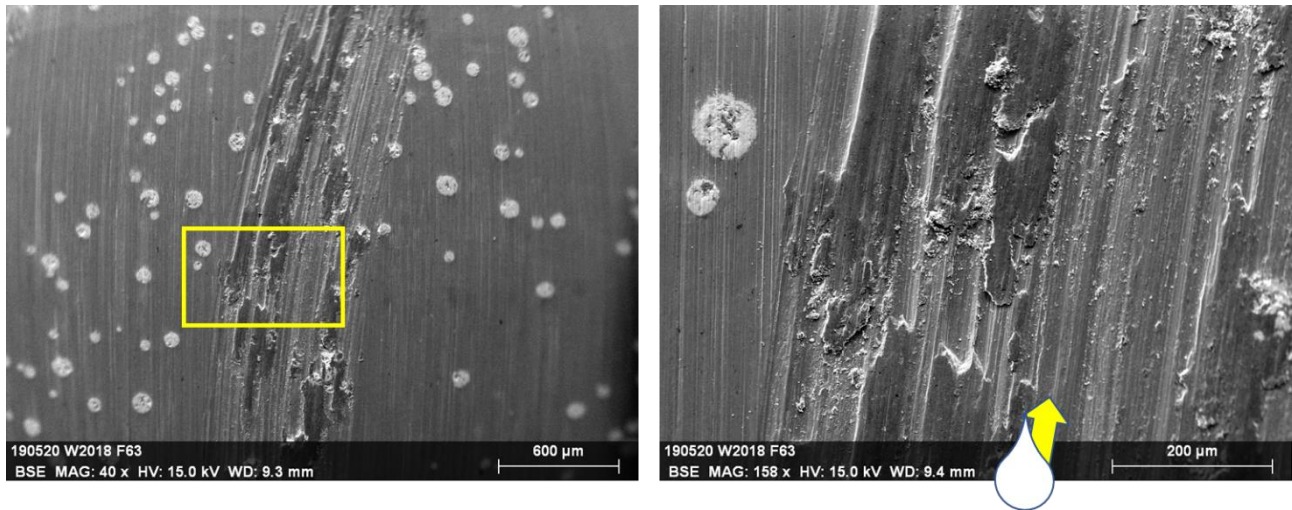
Figure 4-74: Detail of the worn tracks after the first interrupted test. On the right there is a zoom of the zone highlighted on the left.

This layer covers the carbides (Figure 4-75). The EDS composition map of this layer is given in Figure 4-75.
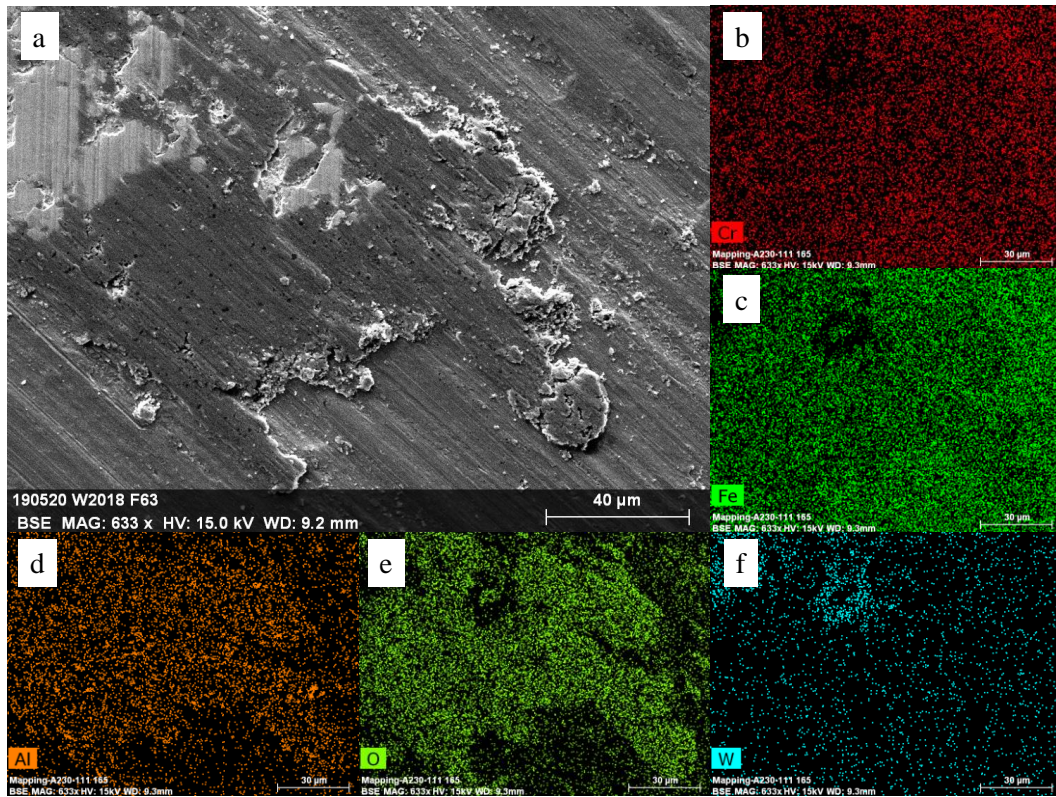
Figure 4-75: (a) BSE mode of a zone on the layer inside the track W20.18 F6.3 8mm (shortest interrupted test: about 1000 cycles) ; from (b) to (f) EDS Composition maps of the zone.

The layer is enriched in aluminum and oxygen. Chromium and iron are present too, but a higher amount is present outside the layer. Lots of tungsten is detected in correspondence to visible portion on the WC.

Another possibility is to observe some carbides not completely covered by this layer (Figure 4-76). The EDS composition map was carried out on this scenario as well:
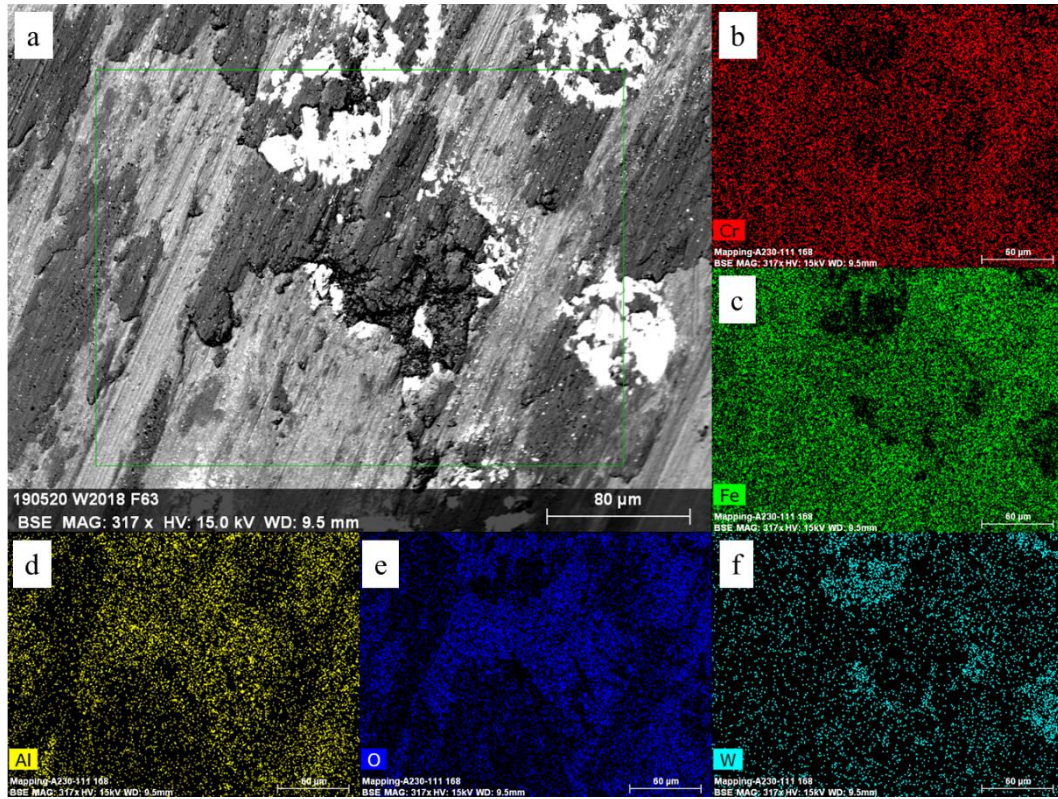
Figure 4-76: (a) BSE mode of a zone stacked material over the WC inside the track W20.18 F6.3 8mm (shortest interrupted test: about 1000 cycles) ; from (b) to (f) EDS Composition maps of the zone.

The stacked material is characterized by a mixed composition of aluminum, oxygen, iron and chromium. The chemical composition of this material is quite similar to the one found for the compact layer. Small local variations in the composition are possible but they do not affect the result.

4.3.5.2   *Second interrupted test (~9500 cycles)*

The second interrupted test was performed like the first on the sample W20.18-F6.3, but at 11mm radius. It was stopped at more or less 9500cycles, just before a sharp variation of the friction coefficient (Figure 4-43). The typical scenario along the track formed during this test, is the one reported in Figure 4-77.
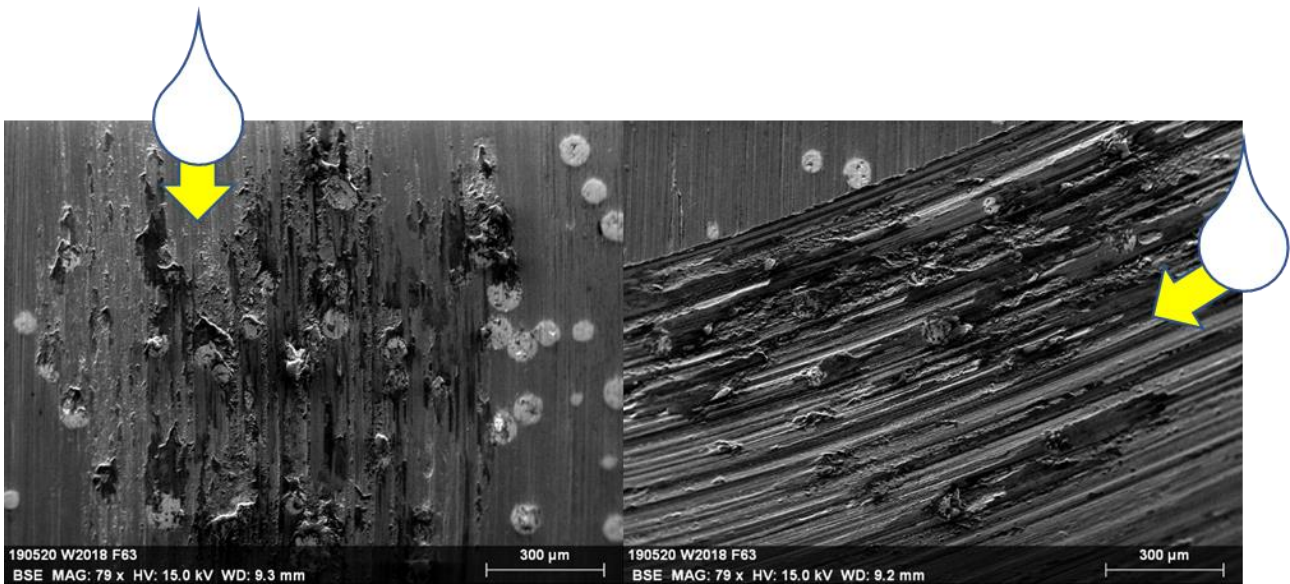
Figure 4-77: Details of the worn tracks after the second interrupted test.

The picture on the left refers to a zone that is less worn (differences in the track depth illustrated in Figure 4-53) while on the right it is shown a more worn zone. Indeed, on the right the presence of grooves is clearer. The images of the tracks (section 4.3.3) show that the depth of the track is not homogeneous everywhere. The Scanning Electron Microscope (SEM) observations show that if a higher concentration of original partially melted tungsten carbides (WC) is present, in that zone the worn track depth is higher.

EDS composition maps were carried out close to a WC in order to observe the distribution of the elements in these zones.
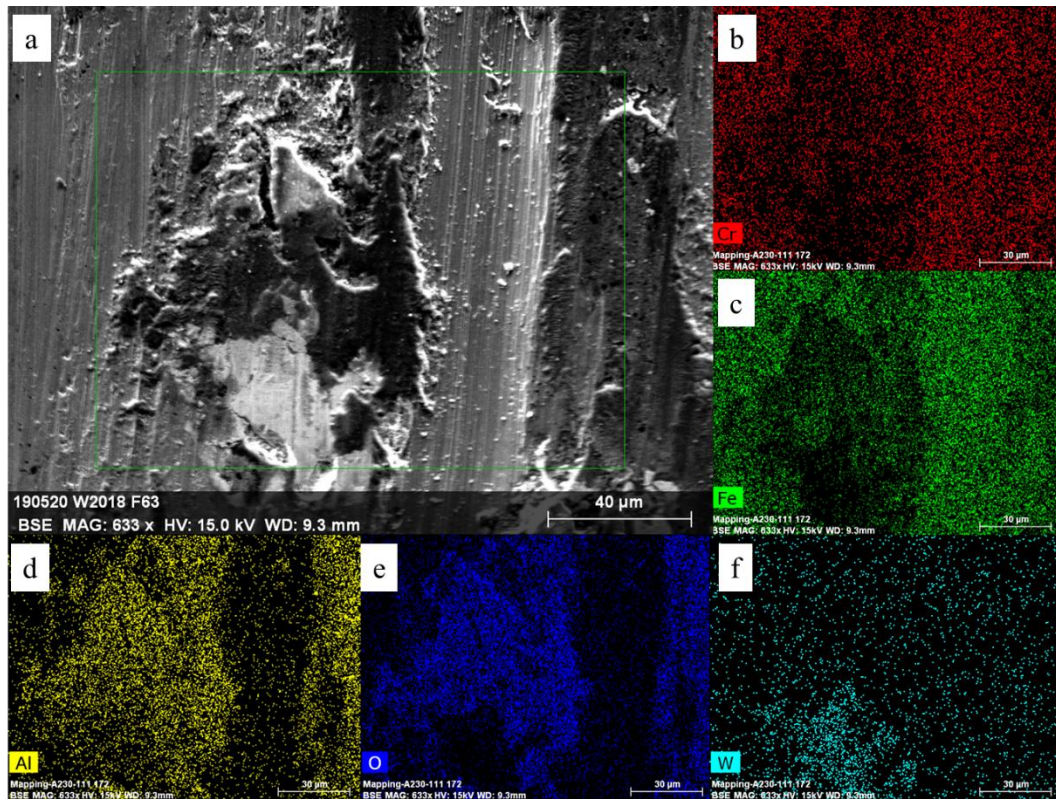
Figure 4-78: (a) SE mode of a detail close to a WC on the worn track of W20.18 F6.3 11mm (stopped at about 9500 cycles, after the stable friction coefficient region); from (b) to (f) EDS Composition maps of the zone.

The material just in front of the carbide is enriched in aluminum and oxygen. The brighter zones own even higher amount of aluminum.
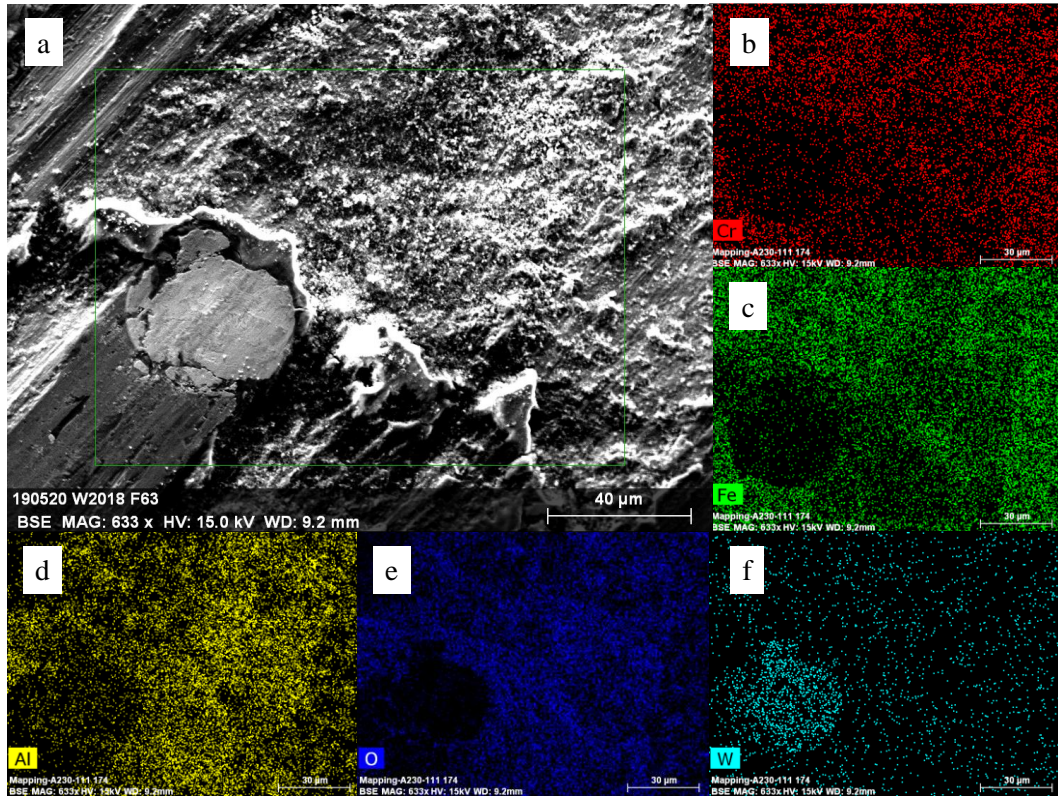
Figure 4-79: (a) SE mode of a detail close to a WC on the worn track W20.18 F6.3 11mm (stopped at about 9500 cycles, after the stable friction coefficient region); from (b) to (f) EDS Composition maps of the zone.

The zone in front of the carbide correspond to a groove, also observed with the profilometer (Figure 4-56). The composition map gives a mixed chemical composition. As settled in the description of the previous image (Figure 4-78), it can be noticed that to the brighter zones correspond higher amount of aluminum.

4.3.5.3 *Third interrupted test (~12000 cycles)*

The third interrupted test was performed on the surface W20.14-H6.3, but at 11mm radius. The test was stopped at slightly less than 12000cycles, just after a sharp variation of the friction coefficient (Figure 4-44). The typical scenario along the track formed during this test is reported in Figure 4-80.
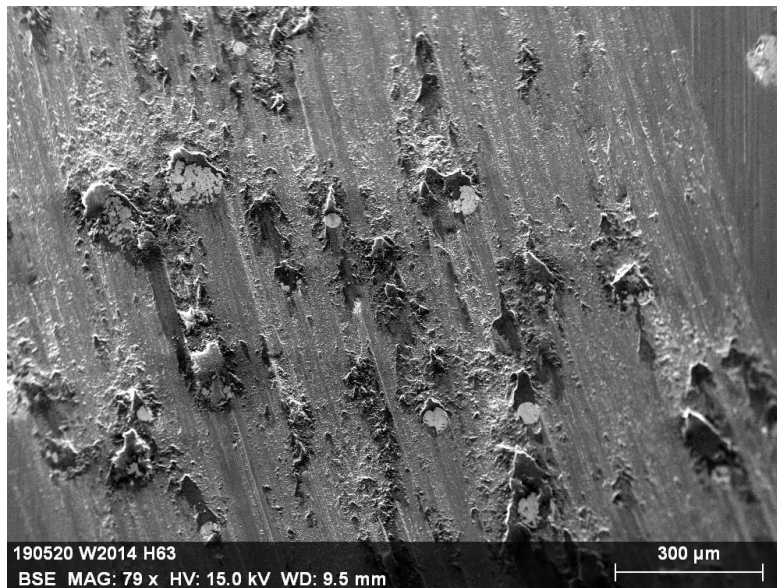
Figure 4-80: Detail of the worn tracks after the third interrupted test.

The grooves can be observed independently to the position of the track, as in the sample before (section 4.3.5.2). The entire surface shows insights of generalized wear.

A detail of the zone in Figure 4-80 is illustrated in Figure 4-81.
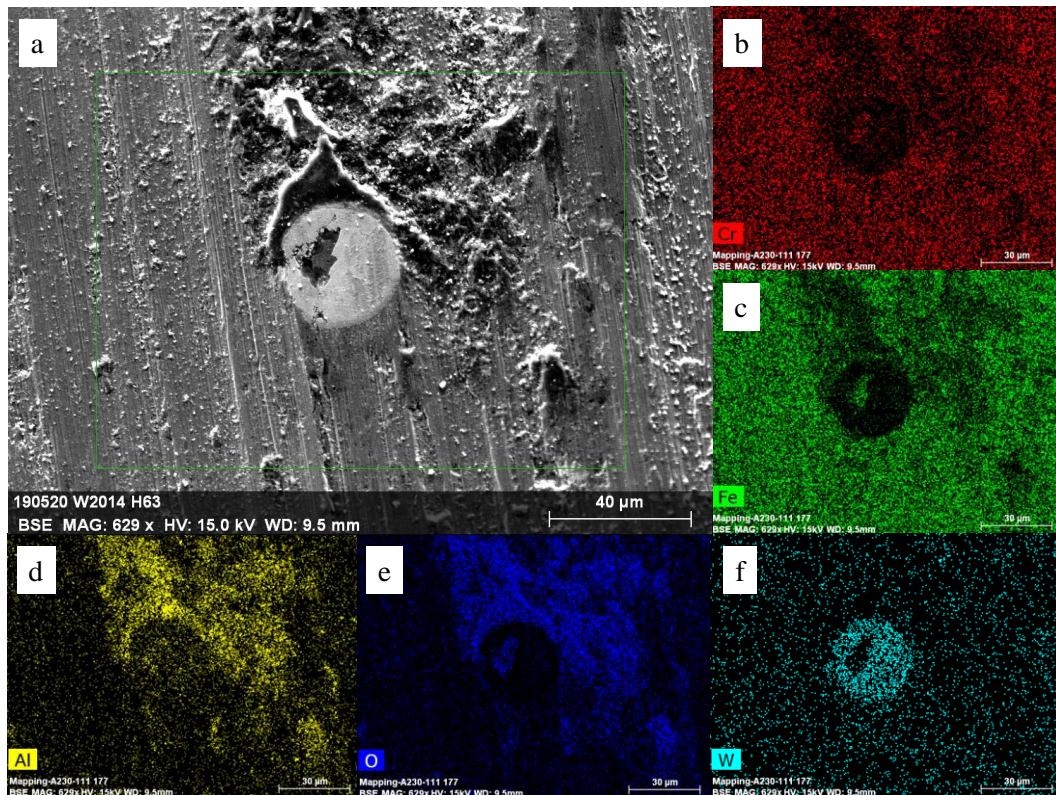
Figure 4-81: (a) BSE mode of a zone on the layer inside the track W20.14 H6.3 11mm (stopped at less than 12000cycles, interrupted just after the drop of the friction coefficient); from (b) to (f) EDS Composition maps of the zone.

In Figure 4-81 it is possible to see a WC. The EDS composition maps shows that the entire examined zone is not oxidized. However, the triangular shaped zone placed at the side of the carbide on the sliding direction is enriched in aluminum and oxygen, despite lower content of iron and chromium.
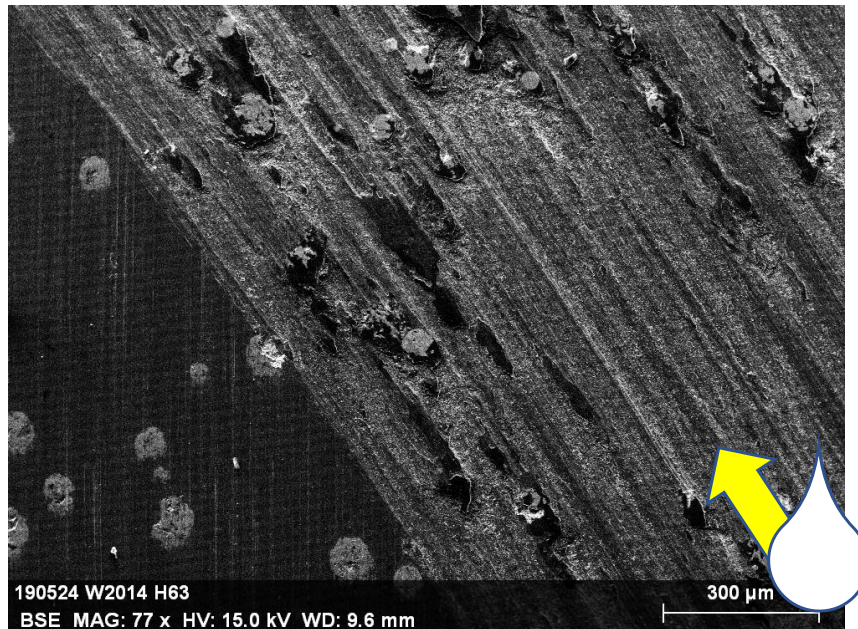
Figure 4-82: Detail of the worn tracks after the third interrupted test.

4.3.5.4   Fourth interrupted test (~15000 cycles)

The fourth interrupted test was performed on the surface W20.14-H6.3 at 8mm radius. This test was stopped at slightly more than 15000 cycles, just before a second sharp variation of the friction coefficient (Figure 4-45). The typical scenario along the track formed during this test, is the one reported in Figure 4-83. Here, a mix of the situations seen before is present. Indeed, there are some local grooves in front of the carbides, stacking of material over few carbides and a very small portion of a dark layer.
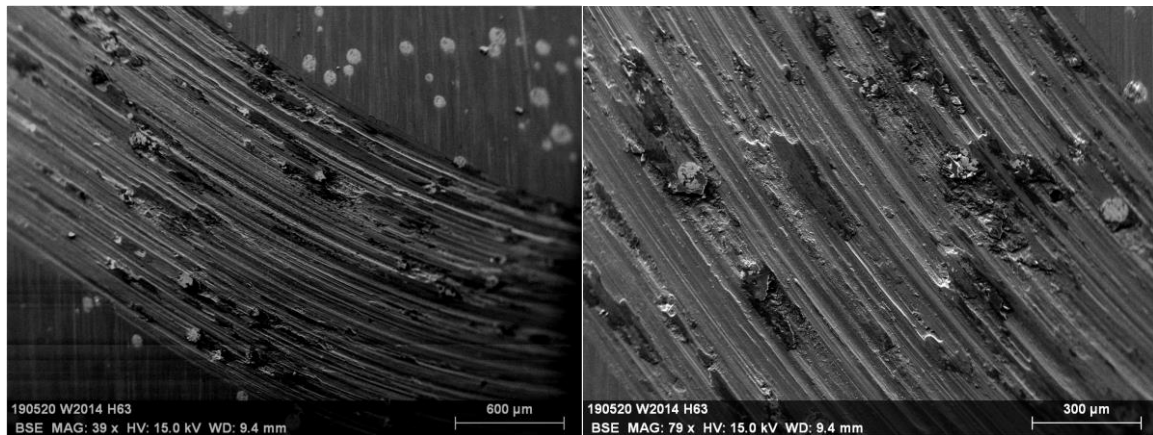
Figure 4-83: Details of the worn tracks after the fourth interrupted test.

4.3.5.5   *Not interrupted test (22000 cycles)*

The longest tests examined in this section ware performed on the sample W20.14-F6.3 (Figure 4-39, Figure 4-40, Figure 4-50, Figure 4-51). It is possible to observe on worn tracks the same phenomena described in the previous sections.
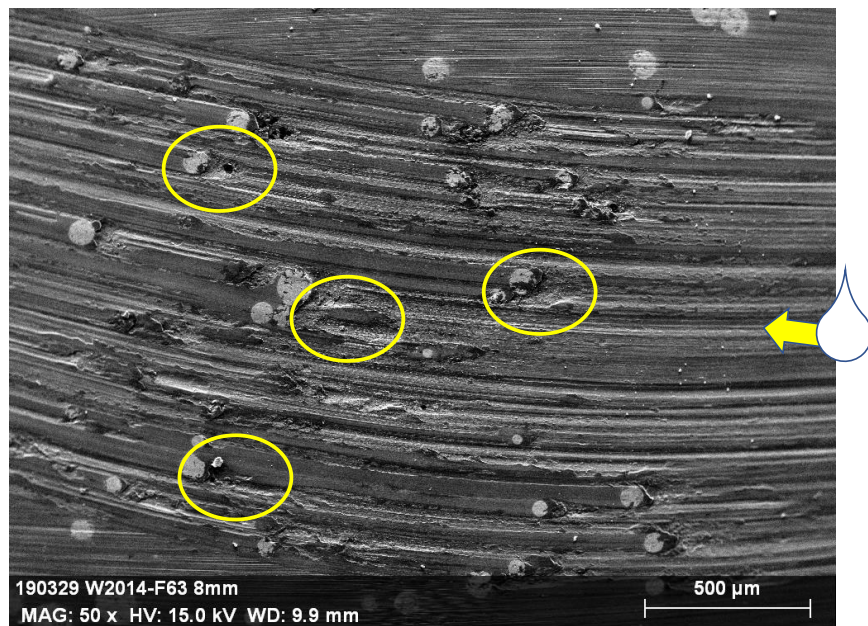
Figure 4-84: Detail of the W20.14-F6.3 10N worn track. The grooves correspond to the highlighted zones.
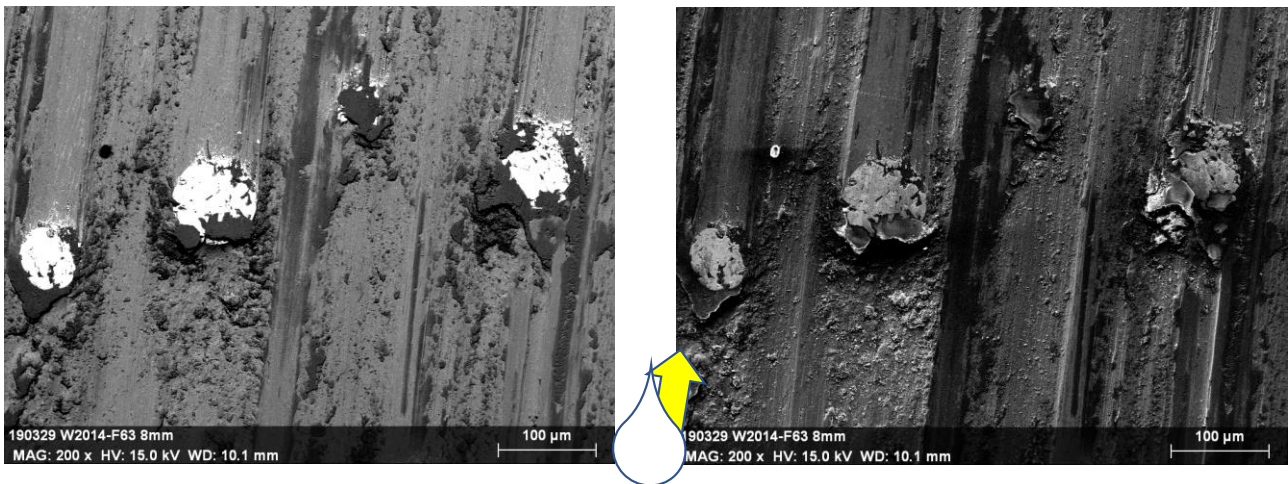
Figure 4-85: Material stacked in front of the carbides
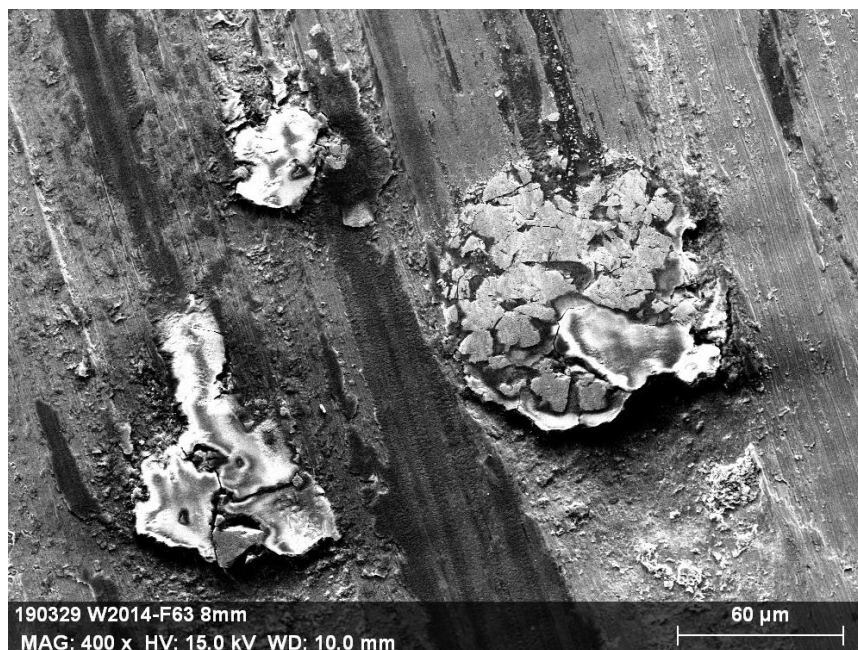
Figure 4-86: Fractured carbide.

In Figure 4-87 the composition of the layer already noticed (section 4.3.5.1) is given. Moreover, it is possible to observe the presence of a crack inside.

Mass %	C	O	Cr	Fe	Al	W	Ni	Si	Mo
Zone 1	2.25	28.08	8.98	33.06	3.58	17.48	5.43	0	0.87
Zone 2	1.93	2.63	15.3	58.62	0.29	7.97	10.88	0.24	2.14
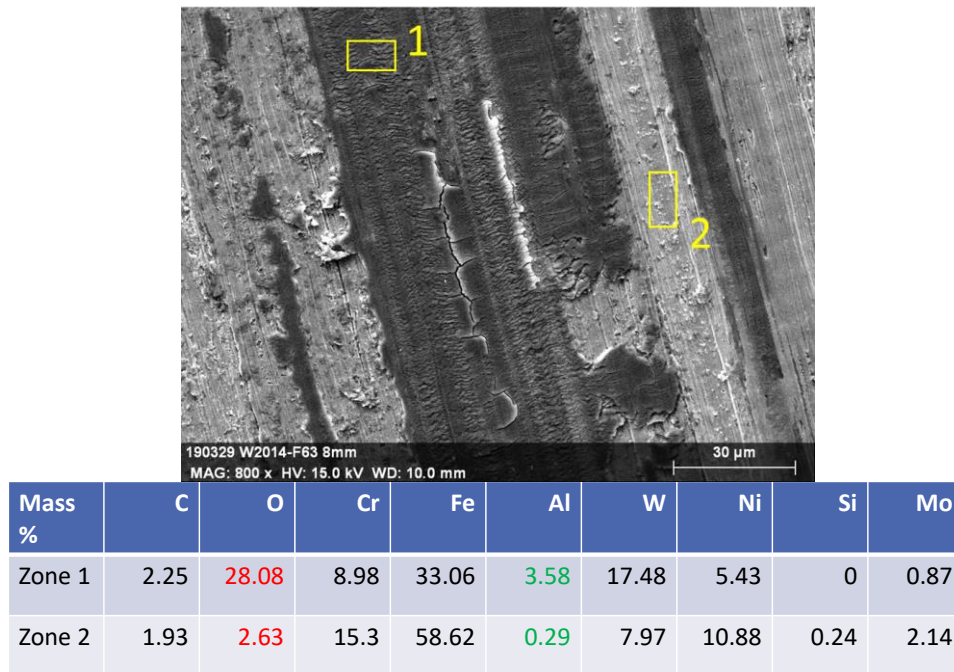
Figure 4-87: Layer cracked from W20.14-6.3.

Some SEM investigations were carried out even in one of the cross sections of the sample where the longest tests were performed. In Figure 4-88 it is possible to observe on fractured carbide well linked to the surrounding matrix and deformation occurred on the carbides dispersed in the matrix according to the sense of the wear test. The out-of-equilibrium carbides follow the deformation and crack at a certain deformation. Those fragments mix with the austenite of the matrix on the first 2-3 µm of the track.
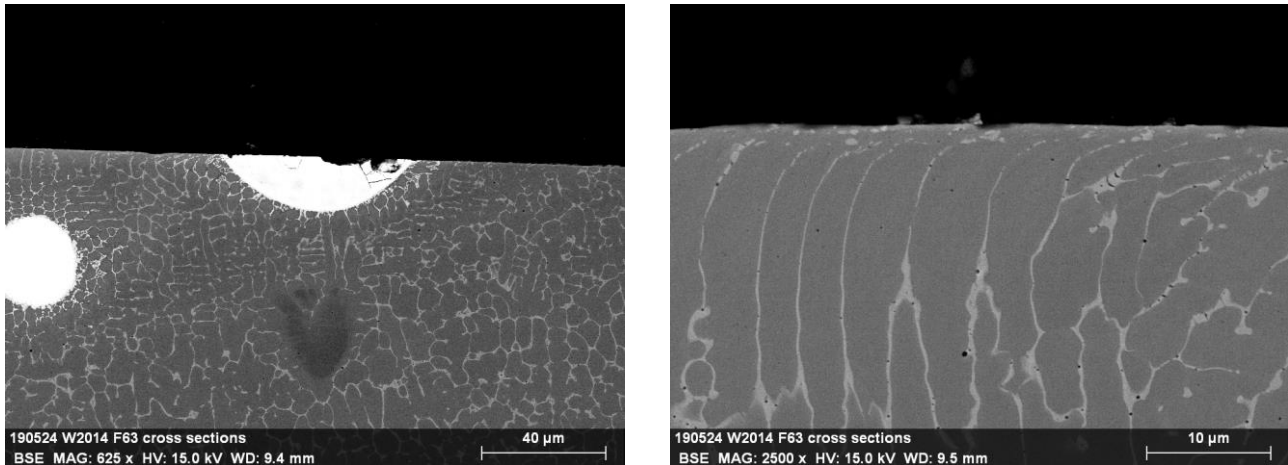
Figure 4-88: Fractured carbide (on the left) deformation of the carbides dispersed in the matrix (on the right).

EDS composition map was carried out in order to analyze a zoom of a small dark debris shown in Figure 4-74. It was recognized as an oxide as well (probably alumina).
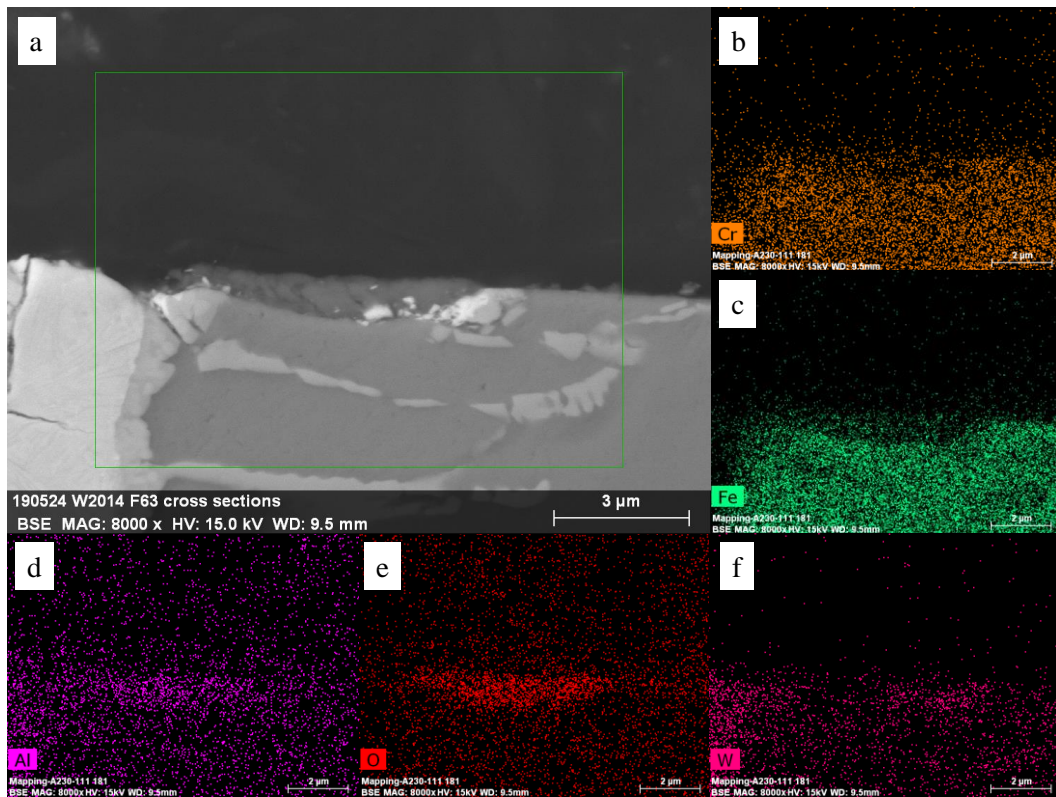
Figure 4-89: (a) BSE mode of a detail found on the cross section of the W20.14 F6.3 (22000cycles); from (b) to (f) EDS Composition maps of the zone.

4.3.5.6   Debris

A small quantity of debris was produced by the wear tests performed. Indeed, their collection was very difficult. Nevertheless, SEM images and a chemical composition analyses were carried out on the debris from the preliminary wear tests and from the two first interrupted tests on the W20.18-F6.3.
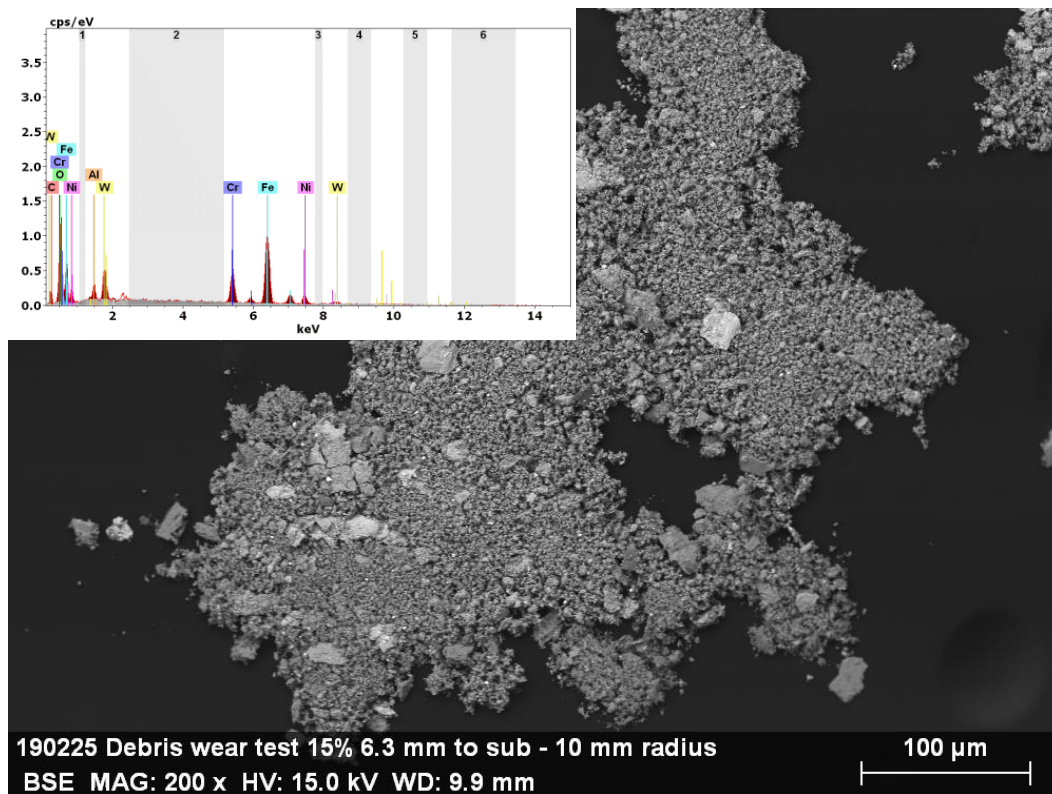
Figure 4-90: SEM image and chemical spectra of small debris from the preliminary tests.

The small debris shows the presence of oxygen and a mixture of element, such as Fe, Al, Cr and W.
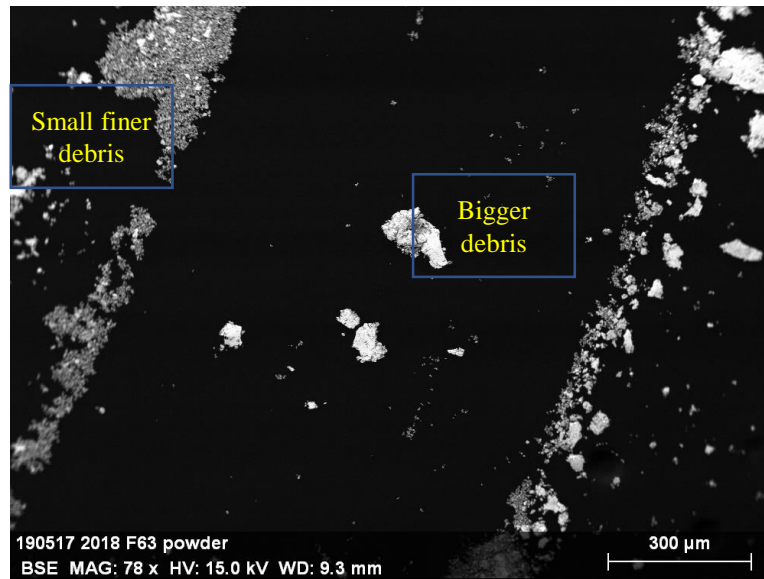
Figure 4-91: Debris SEM image
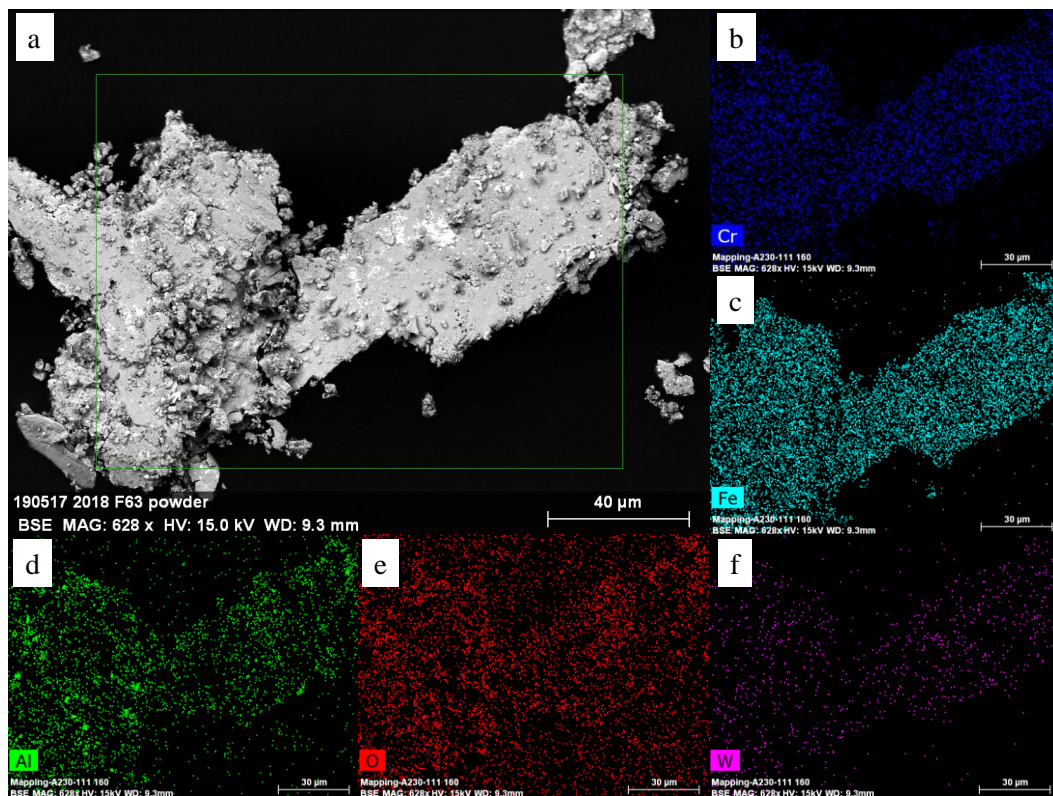
Figure 4-92: : (a) BSE mode of the big debris collected after the two testes on the W20.18-F6.3 (after 1000cycles and after 9500cycles)); from (b) to (f) EDS Composition maps of the zone

Figure 4-92 shows the presence of all the elements on the big debris. Higher concentration of aluminum is present locally.

5. *Discussion*

5.1 *Carbides distribution*

In section 4.1 the distribution of the carbides on the different sections was shown. Firstly, the section XZ was investigated. An almost constant carbides distribution was noticed but slight changes are present (Figure 4-7). These very small variations in the carbides distribution could be explained considering two phenomena:

1) very rarely the laser cladding machine distributes a inconstant WC feed;

2) the "smallest" WC particles are completely melted in the matrix, meanwhile the "biggest" that are only partially melted [97]. This could lead to different amount of WC in the height of the deposit due the different specific surface in contact with the liquid metal. Indeed, the WC carbides observed after cladding in the microstructure are only the "biggest" partially dissolved carbides.

In Figure 4-8 the carbides distribution on the section YZ was presented. Slight inhomogeneities are present. The inhomogeneities in this last case are slightly more evident in comparison to the section XZ because the YZ plane is perpendicular to the layers (the Y direction is the deposition direction). Nevertheless, the change in the carbides distribution can be related to the same two phenomena valid for the section on the XZ plane.

The third examined section (Figure 4-9) was the most representative with respect to the wear tests of this thesis since the wear resistance of the composite was tested on the XY plane. The sharpest variation is along the X distribution. This sudden change of the frequency can be explained with the overlapping of the tracks. Indeed, the side of the deposit is a peculiar zone, where it is possible to have differential deposition that leads to an imprecise overlapping. This means that it is possible to observe the sections of those tracks, but at different heights of the layer.

In all the sections inspected the carbides size distribution has its maximum for 70μm of diameter. The distribution of the original tungsten carbide particles instead has its maximum for 90μm (Annex B 10.2). This is an additional effect of the total or partial dissolution of the WC carbides during cladding depending on their size. During the process the "smallest" particles are completely melted, while the "biggest" ones are partially melted leading the shift on the particles dispersion dimension [97].

Hardness tests were performed on the XZ (Figure 4-1) and XY section (Figure 4-2). In Figure 5-1 the hardness values distribution is compared to the carbides distribution.
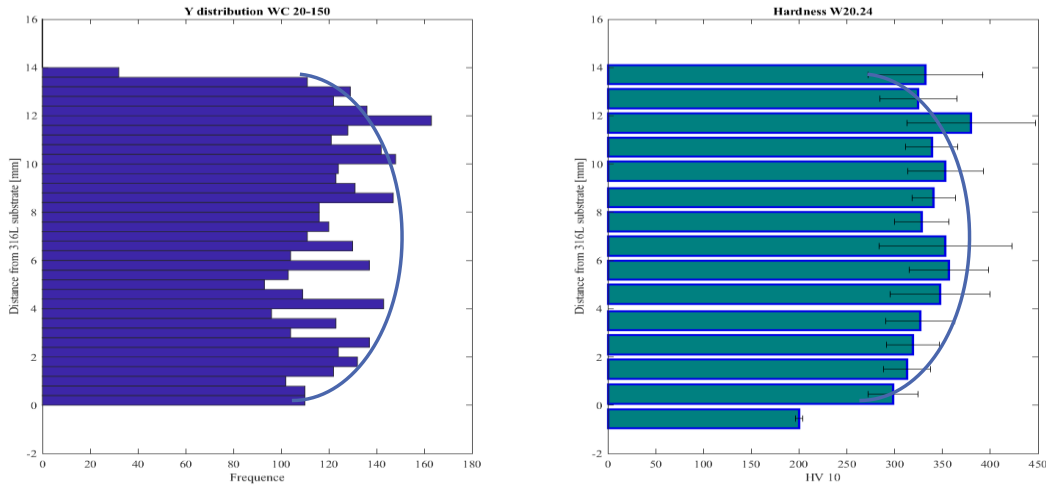
Figure 5-1: Carbides distribution trend on the section XZ in function of the distance from the substrate (left) and hardness trend on section XZ in function of the distance from the substrate (right).

It can be noticed that in many points the hardness follows the carbides distribution. Moreover, a general trend can be defined. The hardness close to the substrate is lower. Then it increases and reaches a higher value at more or less the middle of the deposit. Close to the top, the hardness slightly decreases again.

More hardness tests were performed on other samples (section 4.2). In   *a)*
b)

Figure 4-32a comparison between the pure SS316L and the SS316L+WC is made. A different trend can be noticed. Moreover, the average value of the SS316L+WC is higher in comparison to the SS316L one. This confirm the reinforcing effect of the tungsten carbides.

The section on the XY plane regarding the carbides distribution was found to be particular (section 4.1). Indeed, it is interesting to observe the hardness trend in the X direction (Figure 4-33) and correlate it with the carbides distribution. Meanwhile, the Y direction hardness has an almost homogeneous distribution. Indeed, the observed track with many carbides corresponds to the maximum of the macrohardness, meanwhile an average quantity of WC carbides corresponds on a homogeneous macrohardness.

5.2 Microstructure of the deposit

Investigations were carried out with the Optical Microscope to observe the distribution of the carbides (section 4.1.1). Hardness tests were performed to check the influence of the reinforcement introduced in the SS316L (section 3.4). Then, the microstructure of the material was investigated using the SEM microscopy. In the following, the discussion about the relative results obtained are shown.

In the section 4.1 the different phases present in the SS316L+WC were shown in the different zones. Close to the WC carbides and in the HAZ, two different carbides are observed, while complex regular carbides are present inside the track.

The identification of the phases present in the microstructure was done from the cross consideration of the classical SEM microscopy (morphology and composition) and the results of the EBSD analyses (lattice crystals).

Concerning the EBSD analysis (Figure 4-29 and

Table 4-5) the giant WC is identified as MC (Hexagonal crystal lattice) and M_2C carbide (Trigonal and Orthorombic crystal lattice). A narrow layer of pure tungsten (BCC) is observed around it from the interaction with the liquid metal [95]. The solidification carbides formed around the carbide are identified as cubic crystal lattice. The complex regular carbides are well indexed, but they were not identified.

Considering those results, the cubic carbides around the WC and in the HAZ were associated to M_6C and $M_{23}C_6$ carbides depending on the W and Cr amount. Indeed, their lattice structure is similar and the EBSD is not able to distinguish them completely (Figure 4-28) [96,98]. Indeed, the compositions of the two carbides (brighter and darker) in the two different situations are quite similar with one W-rich brighter carbide and one Cr-rich darker carbide. The skeletal morphology of the brighter carbide and those considerations lead to the association with the M_6C carbide. The FCC lattice crystal and the relative high concentration of Cr lead to the $M_{23}C_6$ carbide for the darker carbide. Regarding the complex regular carbide observed in the track, the peculiar morphology could lead to associate it to the M_2C carbide [48], but the EDS composition is not enough to prove it. Due to the fact that it was indexed, but not identified by the EBSD analyses, there are not informations about the lattice structure of this carbide and considering the extremely high cooling rates at which it is formed, it was so-called out-of-equilibrium carbide. Based on these considerations, precedent and

on-going studies, Figure 5-2 shows the modified Figure 4-13 with the summary of the possible phases present in the microstructure.

Moreover, these reaction carbides own a mixed chemical composition (Table 4-1 and Table 4-3). This particular chemical composition can be related both to the M_6C and the $M_{23}C$. Instead, the carbides in the Heat Affected Zone seem to have morphology that can be found in literature. The brighter carbides have a skeletal morphology that is typical of the M_6C [99] while darker carbides seem to be chromium-based carbides ($M_{23}C_6$). The chemical analysis (Table 4-2, Table 4-4) show that the brighter carbides are more enriched in the heaviest element (Tungsten) while the darker are more enriched in Chromium. Indeed, with a good rate of certitude, it can be said that they are W_6C and $Cr_{23}C_6$ respectively.
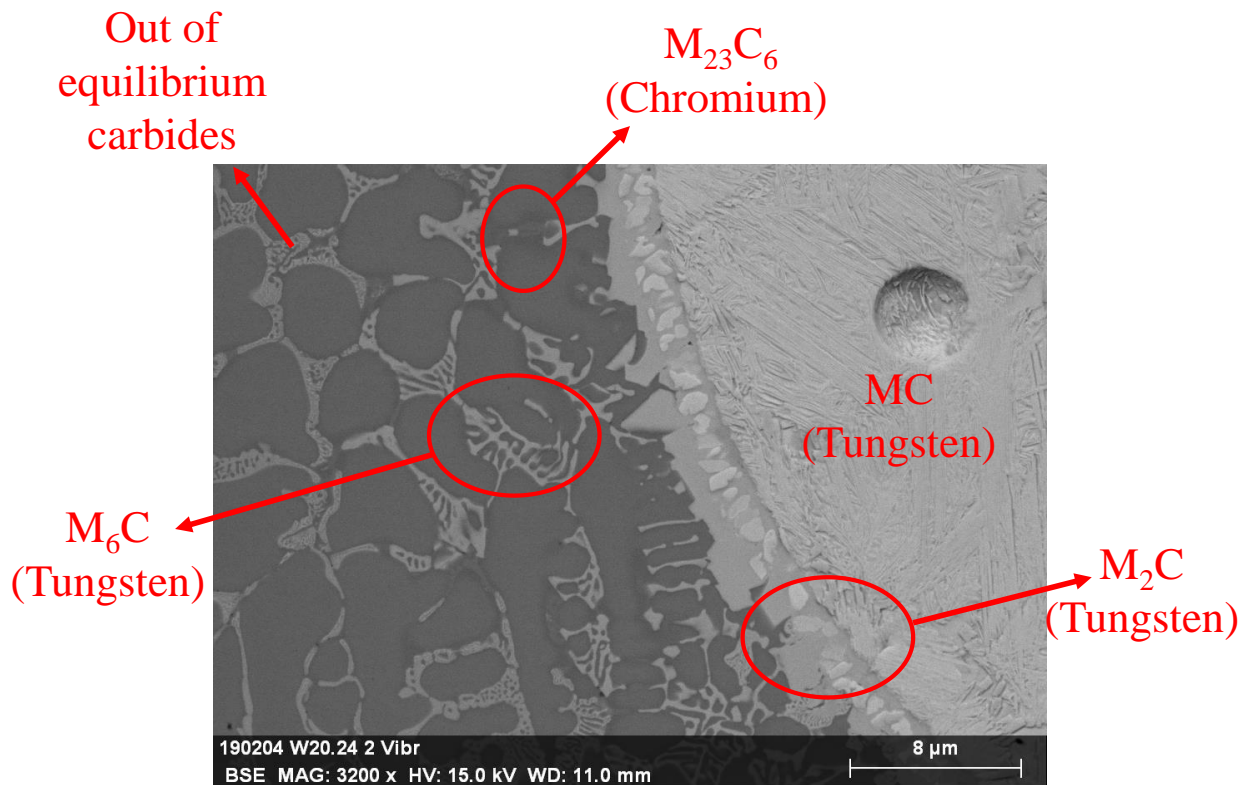
Figure 5-2: Different morphologies of the phases detected.

5.3   Wear behavior of the 316L+20%WC at room temperature

5.3.1 Cross consideration of pin-on-disc results and profilometer observations

The results obtained from the profilometer measurements performed on the wear samples (Table 4-9, Table 4-13) compared to the graphs of the COF evolution (section 4.3.2) allow to make some important consideration.

➢ Table 4-9, Table 4-13 and Figure 4-66, Figure 4-70 show that after a small number of cycles the consumption of the material and of the ball is already important. The measurements on the first interrupted test demonstrate that the dimensions of the track reached more or less 50% of the worn track depth and width on the longest tests, which were performed on the W20.14-F6.3 after 22000cycles (Table 4-9 e Figure 4-66). The worn ball depth and diameter differ of about the 40% (Table 4-13 e Figure 4-70). These results show that during the first stages of the pin-on-disc tests a phenomenon, or a combination of phenomena, causes a severe wear, both on the sample and on the counter-body.

➢ The second drop of the COF present on the results obtained from the two longest tests (after 22000cycles) (Figure 4-39 and Figure 4-40) does not translate in a big change of the wear behavior. Indeed, the dimensions of the worn tracks from the three long tests (the longest among the interrupted stopped at 15000cycles, and the two after 22000cycles) (Table 4-9) are similar. The dimensions of the worn ball after the longest tests (after 22000cycles) are even smaller with respect to the interrupted test after 12000cycles and the one that was stopped at 15000cycles. Tests number three and four, interrupted after 12000cycles and 15000cycles respectively, are the longest test among the interrupted tests, but they were interrupted before the second drop the COF;

➢ The period (number of cycles) in which the COF is stable does not lead to an increase of the worn track depth (Figure 4-66). Indeed, the track depth of the first two consecutive interrupted tests (number one 1000cycles and number two 9500cycles: Figure 4-41) is almost the same. Moreover, the worn track depths detected after the second two tests (number three after 12000cycles, and number four after 15000cycles) have only about 10% of difference (Table 4-9 and Figure 4-66). The worn Al_2O_3 balls for the latest interrupted test do not show great differences in the dimensions. Instead, the balls after the first two interrupted tests are very different (Table 4-13 and Figure 4-70, Figure 4-71). Also, the width of the two tracks and the diameter of the two balls are very different.

113

It is important to say that the longest tests (tests performed checking the repeatability, both stopped after 22000cycles) and the last two interrupted tests (after 12000cycles and after 15000cycles) were made on the same sample (W20.14), on the F surface and on H surface respectively. Meanwhile, the first two interrupted tests (after 1000cycles and after 9500cycles) were done on another sample (W20.18) on the F surface (Figure 3-11).

5.3.2 Elucidation of the wear sequence
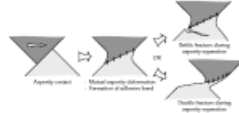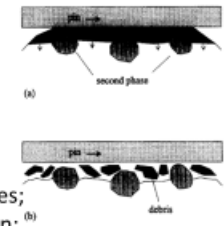
All the work made is focused on the understanding of the wear behavior of the SS316L+WC. The analyses on the microstructure lead to the detection of the phases present in this kind of composite. The tribological tests led to the observation of the friction behavior. The friction behavior was deeper investigated thanks to the cross consideration of the pin-on-disk results and the profilometer analysis. The following wear explanation is obtaining taking in account all the results, the considerations made about them, and the insights provided by the SEM observations.

In section 4.3.1, it was underlined that all the COFs obtained from the wear tests have more or less the same evolution. Based on this observed phenomenon, the profilometer measurements (section 4.3.3 and section 4.3.4) and the SEM analyses (section 4.3.5) it was possible to associate the different wear types in literature, with all the variations or steady state stage of the COF. Moreover, the previous three observations are helpful to fully understand the wear mechanisms acting on the composite material.

A division could be done between the phenomena acting on the partially melted original tungsten carbides (WC) and the phenomena acting on the matrix. The influence of the carbides dispersed in the matrix is not discussed because the cross-sections were not deeply observed. The possible wear mechanisms are summarized in the following tables:

Table 5-1: Phenomena acting on the WC and on the matrix basing on the observations made and the proofs gained.
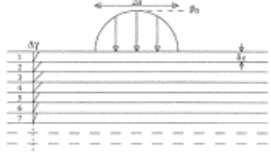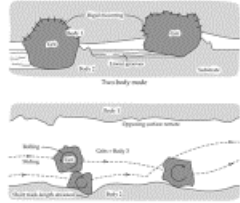
[G.W. Stachowiak, Engineering Tribology, fourth, Butterworth-Heinemann, Oxford, 2013]

	WEAR MECHANISM	OBSERVATIONS	PROOFS	
WC	Adhesive plate-like wear	WC blocks sliding (microscope images)	• Debris "shape"; • Hole in front of WC; • microscope images.	
	Adhesive WC-Al2O3	Electronegativity difference	o WC covered by Al2O3 o Small debris after only few cycles (from weaker asperities)	
MATRIX	Adhesive 316L-Al2O3	• Sliding low at the beginning; • Different electronegativity	• No oxide everywhere;	
	Oxidative wear	o Friction coefficient; o Silence during test; o Chemical composition	o Cracks on oxide layers in holes; o Small fine debris composition; o Oxides on the holes	

[M. Vardavoullas, The role of hard second phases in the mild oxidational wear mechanism of high-speed steel-based materials,,Wear, 1994]

Regarding the wear phenomena occurring with or on the WC big carbides, the presence of Al$_2$O$_3$ over the WC and the formation of small debris after a few cycles lead to the adhesive wear acting between the WC and the counter body. This type of wear is associated to a difference in the electronegativity between the two elements in contact [82], as in this case. The different electronegative is also present between the matrix and the alumina. Moreover, the shape of debris (Figure 4-92) and the grooves in front of the carbides (Figure 4-84) allow to affirm that there is presence of the adhesive plate-like wear [82]. It leads to the WC that "blocks" the sliding. Indeed, some pieces of the WC could pull out after grinding (Figure 4-72) or during the wear test leading to the formation of holes or cavities. The contact of WC and alumina leads to the deposition of the ball by mechanical locking on the resistant side of the carbide, blocking further wear of the alumina. This mechanical effect leads to stacking of alumina over the WC, that is why it is referred to as adhesive wear. The grooves are formed due to the blocking of oxidized and harder debris, causing a plate-like wear with the further cycles of the test and thus the grooves only in front of the WC.

Table 5-2: Phenomena acting on the matrix basing on the observations made and the proofs gained.

	WEAR MECHANISM	OBSERVATIONS	PROOFS	
MATRIX	Delamination	Strain accumulation+ adhesive	• Big debris; • Microscope images	
	Abrasive wear: • 2-body; • 3-body	Oxides/fragments of WC/particles mix form the previous occurrences (and initial asperities)	○ Small debris; ○ Images of fragment carbides	

The adhesive wear involves even the matrix. The presence of small debris, already associated to the WC, actually could be formed by the matrix. Indeed, the small debris can take origin from the small asperities always present on the surface (section 2.5). These asperities are generally very weak because of their size, thus they break quite easily. Moreover, the association of this type of wear mechanism with the matrix is due to the presence of the oxide layer just in few positions of the track.

The oxide formation leads to the logical connection that the oxidative wear [82,83,93] acts in this material. A very high oxygen amount was found in some holes and grooves (Figure 4-79). The oxidative wear was observed by chemical composition analyses on the debris (Figure 4-90) and cracks observed on some layers enriched in oxygen (Figure 4-87). Furthermore, the steady value of the friction coefficient (i.e. Figure 4-40) is typical of this wear type [82,83]. Moreover, interruption of friction noise was observed from the users during more or less 10-20 seconds of the tests before the sudden decreases of μ. This was connected to the wear equilibrium and complete compaction of an oxide layer (during the stable regime, Figure 4-40). Consequently, the drop of the coefficient was assumed to be the breakdown of this layer. This layer has inside a certain content of oxygen as settled by the chemical composition (Figure 4-75).

The delamination wear [84] is associated to the matrix as well from the SEM observations. Indeed, big debris, slipping pieces of the surface (Figure 4-74) and deformed cross-section were connected to this wear. The continuous sliding of the counter body results into a strain accumulation on the sample. The strain accumulation is typical of this wear type [79].

The last wear type associated is the abrasive wear [81,82]. As said in section 2.5.3, it could occur as 2-body abrasive wear and/or as 3-body abrasive wear. The 2-body can be associated to the alumina ball that abrades the matrix, but the WC could wear the ball as well. Indeed, fractured carbides (Figure 4-86 and Figure 4-88) and the deep furrows due to the contact with the ball (matrix is damaged) were detected. The 3-body mechanism is connected to the wear of the matrix since the oxidized and harder debris formed during the wear test cannot be easily evacuated from the track. They remain entrapped during sometime between the ball and the sample, leading to abrasion.

The different wear types enumerated are associated to the Coefficient Of Friction evolution (COF) (Figure 5-3, Figure 5-4, Figure 5-5). The graph of a long test was used as base.
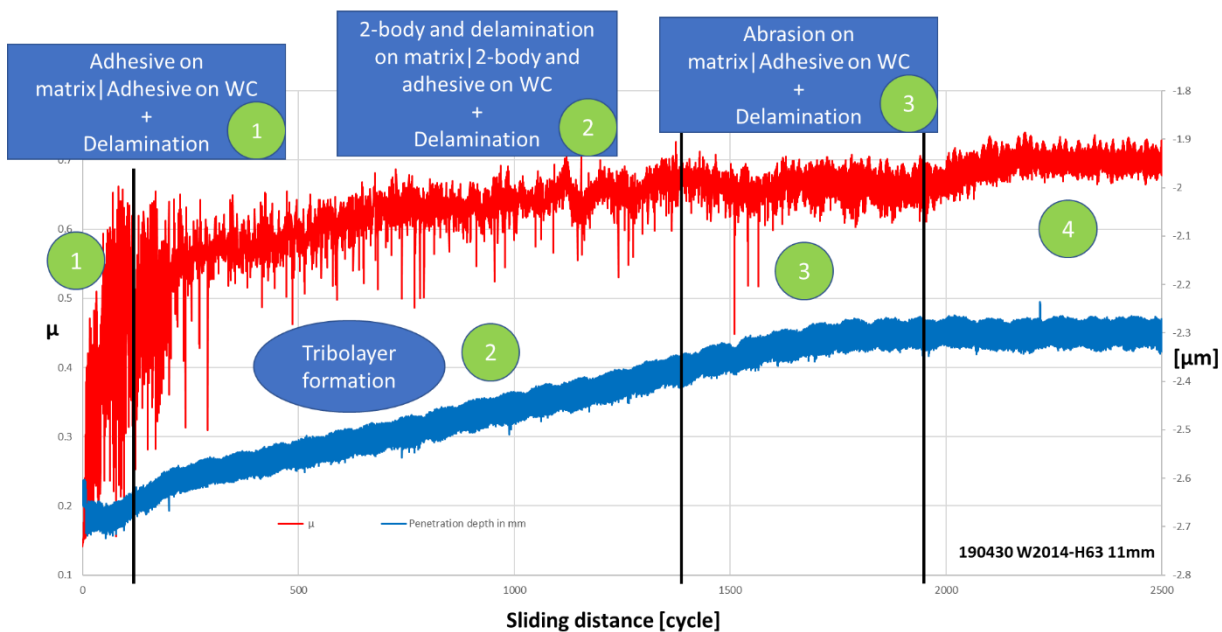
Figure 5-3: Association of the different wear types to the COF evolution.

(1) The sudden increase of the COF can be associated with the adhesive wear [79] and the delamination (Figure 4-74). Indeed, the initial contact of the ball with the sample causes bonding with the asperities of the surface. When the test begins, the asperities are deformed and breaks. This stage is very short because the phenomenon is very fast. Moreover, if the ball encounters protruding part of the WC (Figure 4-72), it could stack over them. Delamination can be present since the original oxidative layer (from the SS316L) was observed in the initial debris. The penetration depth evolution is in agreement with the previous assumptions. Indeed, the penetration depth does not increase, thus the material is not damaged during this first stage.

(2) In the second stage the COF has a huge variability. As mentioned before, the 2-body abrasive wear starts to damage both the matrix and the ball. Moreover, adhesive wear can be present

117

due to the smoothing process of the matrix acting during the first cycles and the stacking of the Al_2O_3. Delamination is still present. The outer parts of the sample, the ones without a great concentration of WC, are sensitive to the wear and start to slide. In this second stage, the formation for debris is more consistent and therefore the formation of a tribolayer begins [53,57,82,93,100]. The penetration depth in this second stage increases since the matrix and the ball started to get damaged. Actually, a large part of the debris enriching the tribolayer are formed by the plate-like wear in the grooves at WC side. When the quantity of debris formed are in excess, some particles can move freely laterally without obstacles (Figure 4-91).

(3) In the third stage the stacking of alumina on the WC continues and the abrasion continues on the matrix. Hence, the ball continues to penetrate in the sample.
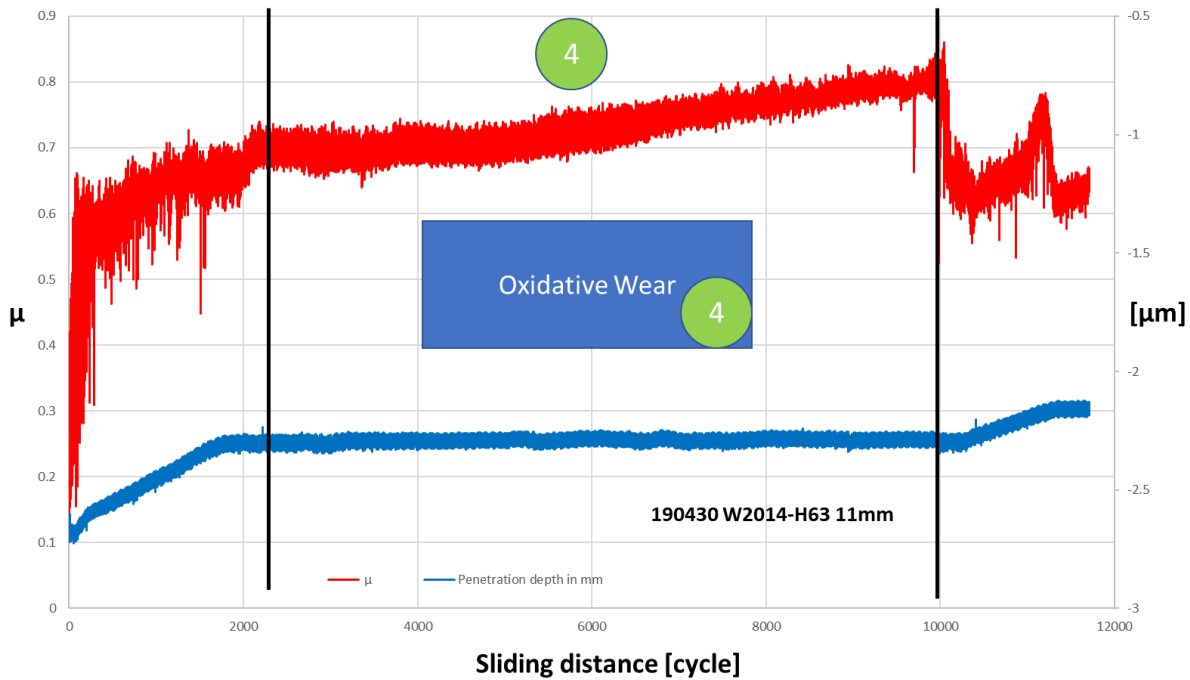
Figure 5-4: Association of the different wear types to the COF evolution.

(4) In the fourth stage the tribolayer is compacting and some debris removed from the material starts to oxide. The oxidative wear mechanism acts in this stage. As settled in literature [81–83] the COF remains almost stable because the tribolayer is partially oxidized and it does not have a great influence on the sliding. The penetration depth remains stable too. Indeed, the material and the ball are not so damaged during the COF steady stage (Table 4-9 and Table 4-13).

118
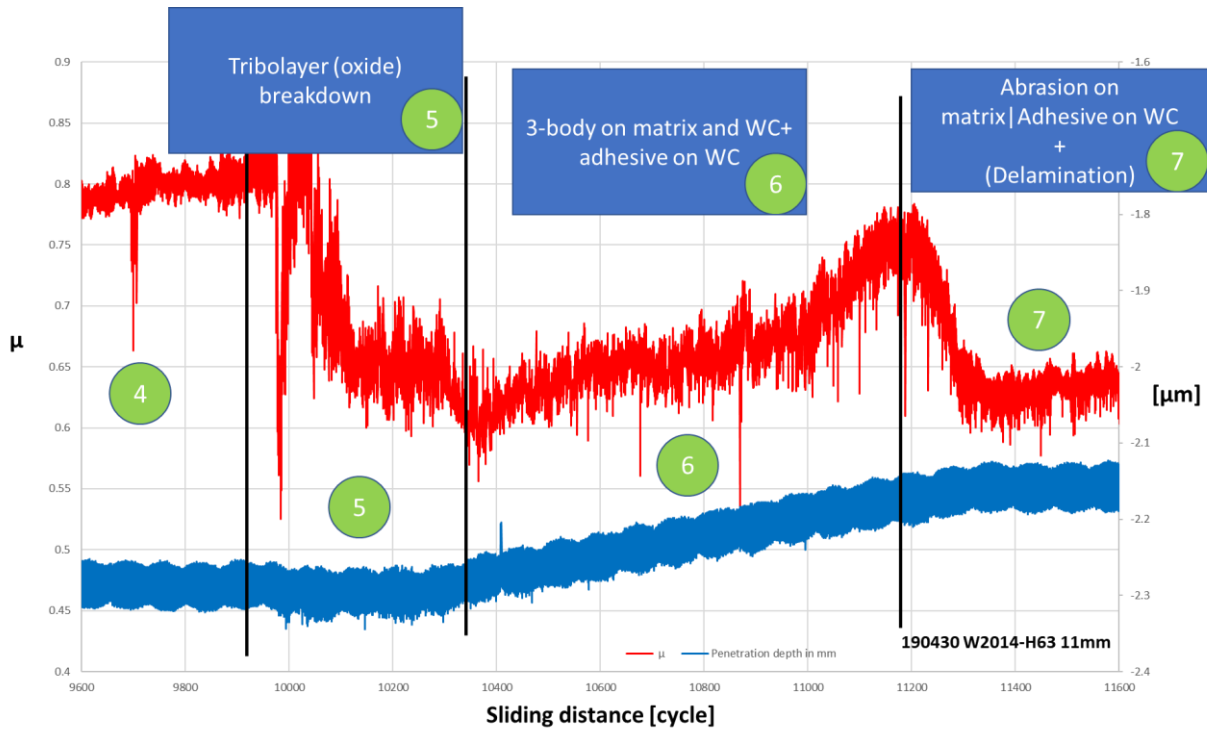
Figure 5-5: Association of the different wear types to the COF evolution.

With the progress of the test, the quantity of debris increases and the compaction of the tribolayer proceeds, thus leading to an increase of the strain with the sliding. When the thickness reaches a critical value [82] and the strain is too high to be sustained [84] the tribolayer breaks. **(5)** This phenomenon leads to a sharp drop of the COF because the counter body finds less resistance. The penetration depth shows a greater variability probably because the tribolayer does not break uniformly along the entire track, but instead it seems that the penetration depth decreases. This can be related to the debris of the broken tribolayer that needs time to go away from the track. Thus, at the beginning of the breakdown the debris produced a very small rise the alumina ball.

(6) In the sixth stage the presence of the tribolayer debris leads to the 3-body abrasive wear mechanism. Some of these debris remain entrapped inside the track. The penetration depth increases since the material is abraded so the ball can slightly penetrate.

When the debris go away or are compacted, the COF and the penetration depth continue to vary since the last wear stage begins. **(7)** The last stage (number seven) is characterized by the same mechanisms as the third stage. This is because the scenario after the tribolayer breakdown is similar to the one at the beginning of the wear test, after the second stage with the exposition of the WC and new layer of matrix.

119

Because the seventh stage is similar to the third, it can be assumed that oxidative wear will be repeat, leading to a kind of cyclical wear behavior. Thus, a second COF stability region will be present and also a second drop as seen in some test, leading to further loss of material.

6. *Conclusions*

The friction evolution and the wear behavior of laser clad SS316L+ WC composite coating at room temperature was studied. The samples were produced in Sirris [1].

The wear tests were performed after the microstructural characterization and its influence on the hardness. It is possible to make some consideration after the observations of the worn tracks formed by the counter body (Al_2O_3 ball). The scenario consisting of a very high concentration of carbide in a well-delimitated zone of the sample, acts as protection to the wear (section 4.3.5).

All the samples shown almost the same friction behavior characterized by some different steps in the Coefficient Of Friction (COF) evolution (section 4.3). Each of these stages suggested the presence of many wear mechanisms acting during the tests. Hence, shorter tests were carried out in order to check the wear response of the material for each COF evolutions. Profilometer measurements allowed to evaluate the dimensions of the worn track and the worn Al_2O_3 ball (section 4.3.3 and 4.3.4). With the cross consideration of pin-on-disk results, profilometer analysis and SEM observation, it was possible to understand the wear behavior of the SS316L+WC composite material.

After only few cycles a very consistent part of the wear already takes place (section 5.3.1). Indeed, several wear mechanisms that leads to materials consumption act just at the beginning of the tests. Proofs of adhesive wear, abrasion wear (especially 2-body type) and delamination were found related to the evolutions of the COF within 1500/2000 cycles. In this part of the experiments the formation of the tribolayer begins. Material consumption continues further. The oxidation of the tribolayer gives a steady COF period. Typical of this wear mechanism is the action of protection by the tribolayer on the samples. When the thickness reaches a critical value and when the strain accumulation cannot be sustained anymore, the partially oxidized tribolayer breaks down. The debris resulting from this phenomenon act as 3rd body between the sample and the alumina ball. Thus, weak abrasion wear (3-body type) take place. When the debris go away abrasion, adhesion and delamination act again till the beginning of the oxidation of a second newly formed tribolayer. The second COF steady state and the second COF drop observed in some uninterrupted tests, suggests a sort of repetitiveness of some wear mechanism corresponding to the COF cycling evolution.

7.   Perspectives

The SS316L+WC composite coating could be used in the industries to enhance the work life of the mechanical parts subjected to wear. This MMCs has all the good properties owned by the stainless steel. In addition, the introduction of the WC improve the hardness of the material and it was found that the WC have a protection effect on the wear acting during room temperature tests. A reference test on the pure SS316L is crucial to have the final confirmation.

In this study all the tests were performed at the same altitude so it will be interesting check also the wear performing tests at the different height of the deposited produced. Moreover, many industrial environments are characterized by high temperature condition. Thus, one of the next steps will be to perform high temperature wear test.

The wear behavior is a very complex phenomenon to be understand because it can involve combinations of various different mechanisms. The setup of the tribometer utilized influences each wear mechanism. Nevertheless, the evaluation of the wear loss volume is necessary in order to have a base for comparison with other materials on the market.

Finally, it would be interesting investigate also the influence of the carbides dispersed in the matrix. In this work it is not discussed because the cross-sections were not deeply observed.

9. References

[1] Sirris. https://www.sirris.be/ (accessed May 19, 2019).

[2] ASTM International, ISO, INTERNATIONAL STANDARD ISO / ASTM Additive manufacturing — General principles — Requirements for purchased AM parts, 5 (2017).

[3] Y. Zhai, D.A. Lados, J.L. Lagoy, Additive Manufacturing: Making imagination the major Limitation, Jom. 66 (2014) 808–816.

[4] M.P. Groover, E.W. Zimmer, CAD/CAM: computer-aided design and manufacturing, P T R Prentice Hall Prentice-Hall, Inc., New Jersey, 1984.

[5] A. Mertens, Personal lesson notes of Techniques de fabrication additive et 3D Printing., (2018).

[6] Y. Lee, M. Nordin, S.S. Babu, D.F. Farson, Effect of fluid convection on dendrite arm spacing in laser deposition, Metall. Mater. Trans. B Process Metall. Mater. Process. Sci. 45 (2014) 1520–1529.

[7] C. Navas, A. Conde, B.J. Fernández, F. Zubiri, J. de Damborenea, Laser coatings to improve wear resistance of mould steel, Surf. Coatings Technol. 194 (2005) 136–142.

[8] V.K. Balla, M. Das, A. Mohammad, A.M. Al-Ahmari, Additive Manufacturing of γ-TiAl: Processing, Microstructure, and Properties, Adv. Eng. Mater. 18 (2016) 1208–1215.

[9] W.E. Frazier, Metal additive manufacturing: A review, J. Mater. Eng. Perform. 23 (2014) 1917–1928.

[10] W.E. King, A.T. Anderson, R.M. Ferencz, N.E. Hodge, C. Kamath, S.A. Khairallah, A.M. Rubenchik, Laser powder-bed fusion additive anufacturing of metals; physics, computational, and materials challenges, Addit. Manuf. Handb. Prod. Dev. Def. Ind. 041304 (2017) 461–506.

[11] M. Weglowski, Electron Beam Additive Manufacturing with Wire, Trends Civ. Eng. Its Archit. 1 (2018) 25–2.

[12] R. Vilar, Laser Cladding, J. Laser Appl. 119 (1999) 263–306.

[13] E.C. Santos, M. Shiomi, K. Osakada, T. Laoui, Rapid manufacturing of metal components by laser forming, Int. J. Mach. Tools Manuf. 46 (2006) 1459–1468.

[14] A.K. Ehsan Toyserkani, S. Corbin, Laser Cladding, CRC PRESS, Boca Raton, Florida, 2004.

[15] L. Santo, Laser cladding of metals : a review, Surf. Sci. 2 (2008) 327–336.

[16] U. de Oliveira, V. Ocelík, J.T.M. De Hosson, Analysis of coaxial laser cladding processing conditions, Surf. Coatings Technol. 197 (2005) 127–136.

[17] E. Mancini, Studio delle etereogenità microstrutturali in un rivestimento composito a matrice metallica di acciaio inossidabile 316L e carburo di tungsteno, (2017).

[18] M. Yakout, M. Elbestawi, Additive Manufacturing of Composite Materials: An Overview, (2017). https://www.researchgate.net/publication/316688880.

[19] J.W. Kaczmar, K. Pietrzak, W. Wlosiński, Production and application of metal matrix composite materials, J. Mater. Process. Technol. 106 (2000) 58–67.

[20] D.D. Gu, W. Meiners, K. Wissenbach, R. Poprawe, D.D. Gu, W. Meiners, K. Wissenbach, R. Poprawe, Laser additive manufacturing of metallic components : materials , processes and mechanisms, 6608 (2013).

[21] M.P. and P.F. Diego Manfredi, Flaviana Calignano, Manickavasagam Krishnan, Riccardo Canali, Elisa Paola Ambrosio, Sara Biamino, Daniele Ugues, Additive Manufacturing of Al Alloys and Aluminium Matrix Composites (AMCs), i (2014) 13.

[22] S. Tjong, K. Lau, Abrasion resistance of stainless-steel composites reinforced with hard TiB 2 particles, Compos. Sci. Technol. 60 (2000) 1–6.

[23] A. Bandyopadhyay, R. Atisivan, G. Kuhn, S. Yeruva, Mechanical Properties of Interconnected Phase Alumina-Al Composites, (2000) 24–31.

[24] J. Nurminen, J. Näkki, P. Vuoristo, Microstructure and properties of hard and wear resistant MMC coatings deposited by laser cladding, Int. J. Refract. Met. Hard Mater. 27 (2009) 472–478.

[25] S. Rawal, Metal-matrix composites for space applications, Jom. 53 (2001) 14–17.

[26] J.C. Betts, B.L. Mordike, M. Grech, Characterisation, wear and corrosion testing of laser-deposited AISI 316 reinforced with ceramic particles, Surf. Eng. 26 (2009) 21–29.

[27] G. Thawari, G. Sundarararjan, S. V. Joshi, Laser surface alloying of medium carbon steel with SiC(P), Thin Solid Films. 423 (2003) 41–53.

[28] N.R. Baddoo, Stainless steel in construction: A review of research, applications, challenges and opportunities, J. Constr. Steel Res. 64 (2008) 1199–1206.

[29] Y.H. Kim, K.Y. Kim, Y.D. Lee, Nitrogen-Alloyed, Metastable Austenitic Stainless Steel for Automotive Structural Applications, Mater. Manuf. Process. 19 (2004) 51–59.

[30] G.L. Winters, M.J. Nutt, Stainless Steels for Medical and Surgical Applications, Stainl. Steels Med. Surg. Appl. (2008).

[31] ASM international, Properties and Selection: Irons, Steels, and High-Performance Alloys, 3 (1990).

[32] International Stainless Steel Forum, The Stainless Steel Family, Www.Worldstainless.Org. 32 (2013).http://www.worldstainless.org/Files/issf/non-image files/PDF/TheStainlessSteelFamily.pdf.

[33] K. Brunelli, Personal notes of Science and Techonogy of Metallic Materials, (2017).

[34] E.L. Hall, C.L. Briant, Chromium Depletion in the Vicinity of Carbides in Sensitized Austenitic Stainless Steels., Metall. Trans. A, Phys. Metall. Mater. Sci. 15 A (1984) 793–811.

[35] A. Atlas Steels, Stainless Steel 316L & 316H Data Sheet, (2011) 1–2. http://www.atlassteels.com.au/documents/Atlas_Grade_datasheet_316_rev_Jan_2011.pdf.

[36] R. Koc, S.K. Kodambaka, ChemInform Abstract: Tungsten Carbide (WC) Synthesis from Novel Precursors., ChemInform. 31 (2010) no-no.

[37] Q. Fang, W. Bai, J. Yang, X. Xu, G. Li, N. Shi, M. Xiong, H. Rong, Qusongite (wc): A new mineral, Am. Mineral. 94 (2009) 387–390.

[38] A.S. Kurlov, A.I. Gusev, Tungsten Carbides: Structure, Properties and Application in Hardmetals, 2013.

[39] M. Ashby, "CES EduPack.," (2017).

[40] M.. Griffith, M.. Schlienger, L.. Harwell, M.. Oliver, M.. Baldwin, M.. Ensz, M. Essien, J. Brooks, C.. Robino, J.. Smugeresky, W.. Hofmeister, M.. Wert, D.. Nelson, Understanding thermal behavior in the LENS process, Mater. Des. 20 (2002) 107–113.

[41] V. Manvatkar, T. Debroy, V. Manvatkar, T. Debroy, Spatial variation of melt pool geometry , peak temperature and solidification parameters during laser assisted additive manufacturing process, 0836 (2015).

[42] Y. Zhong, L. Liu, S. Wikman, D. Cui, Z. Shen, Intragranular cellular segregation network structure strengthening 316L stainless steel prepared by selective laser melting, J. Nucl. Mater. 470 (2016) 170–178.

[43] K. Li, D. Li, D. Liu, G. Pei, L. Sun, Microstructure evolution and mechanical properties of multiple-layer laser cladding coating of 308L stainless steel, Appl. Surf. Sci. (2015).

[44] M. Ziętala, T. Durejko, M. Polański, I. Kunce, T. Płociński, W. Zieliński, M. Łazińska, W. Stępniowski, T. Czujko, K.J. Kurzydłowski, Z. Bojar, The microstructure, mechanical properties and corrosion resistance of 316 L stainless steel fabricated using laser engineered net shaping, Mater. Sci. Eng. A. 677 (2016) 1–10.

[45] P. Guo, B. Zou, C. Huang, H. Gao, Mechanical properties and machinability of efficiently additive manufactured AISI 316L stainless steel by high-power direct laser deposition, J. Mater. Process. Tech. 240 (2017) 12–22.

[46] J.D. Majumdar, A. Pinkerton, Z. Liu, I. Manna, L. Li, Mechanical and electrochemical properties of multiple-layer diode laser cladding of 316L stainless steel, Appl. Surf. Sci. 247 (2005) 373–377

[47] B. Song, X. Zhao, S. Li, C. Han, Q. Wei, S. Wen, J. Liu, Y. Shi, Differences in microstructure and properties between selective laser melting and traditional manufacturing for fabrication of

metal parts: A review, Front. Mech. Eng. 10 (2015) 111–125.

[48]   M. Boccalini, H. Goldenstein, Solidification of high speed steels, Int. Mater. Rev. 46 (2001) 92–115.

[49]   S. Ma, J. Xing, Y. He, Y. Li, Z. Huang, G. Liu, Q. Geng, Microstructure and crystallography of M7C3 carbide in chromium cast iron, Mater. Chem. Phys. 161 (2015) 65–73.

[50]   R.A. Mulford, E.L. Hall, C.L. Briant, Sensitization of Austenitic Stainless Steels II. Commerical Purity Alloys., Corrosion. 39 (1983) 132–143.

[51]   L. da S. Ferreira, K. Graf, A. Scheid, Microstructure and Properties of Nickel-based C276 Alloy Coatings by PTA on AISI 316L and API 5L X70 Steel Substrates, Mater. Res. 18 (2015) 212–221.

[52]   N. Ur Rahman, D.T.A. Matthews, M. de Rooij, A.M. Khorasani, I. Gibson, L. Cordova, G. Römer, An Overview: Laser-Based Additive Manufacturing for High Temperature Tribology, Front. Mech. Eng. 5 (2019) 1–15.

[53]   P.H. Mayrhofer, C. Mitterer, L. Hultman, H. Clemens, Microstructural design of hard coatings, Prog. Mater. Sci. 51 (2006) 1032–1114.

[54]   T. Schopphoven, A. Gasser, K. Wissenbach, R. Poprawe, Investigations on ultra-high-speed laser material deposition as alternative for hard chrome plating and thermal spraying, J. Laser Appl. 28 (2016) 022501.

[55]   M. Pellizzari, D. Cescato, M.G. De Flora, Hot friction and wear behaviour of high speed steel and high chromium iron for rolls, Wear. 267 (2009) 467–475.

[56]   M. Pellizzari, A. Molinari, G. Straffelini, Tribological behaviour of hot rolling rolls, Wear. 259 (2005) 1281–1289.

[57]   H. Torres, M. Varga, F. Widder, U. Cihak-Bayr, O. Viskovic, M. Rodríguez Ripoll, Experimental simulation of high temperature sliding contact of hot rolled steel, Tribol. Int. 93 (2016) 745–754.

[58]   S. Lester, N. Longfield, J. Griffiths, J. Cocker, C. Staudenmaier, G. Broadhead, New Systems for Laser Cladding, Laser surface modifications in steel industry, Laser Tech J. 10 (2013) 41–43. http://www.precitec.de/uploads/media/41_ftp_03.pdf.

[59]   A.S.C.M. D'Oliveira, R. Vilar, C.G. Feder, High temperature behaviour of plasma transferred arc and laser Co-based alloy coatings, Appl. Surf. Sci. 201 (2002) 154–160.

[60]   Y. Yang, Microstructure and properties of laser-clad high-temperature wear-resistant alloys, Appl. Surf. Sci. 140 (1999) 19–23.

[61]   K. Van Acker, D. Vanhoyweghen, R. Persoons, J. Vangrunderbeek, Influence of tungsten carbide particle size and distribution on the wear resistance of laser clad WC/Ni coatings,

Wear. 258 (2005) 194–202.

[62] W. Ya, B. Pathiraj, D.T.A. Matthews, M. Bright, S. Melzer, Cladding of Tribaloy T400 on steel substrates using a high power Nd:YAG laser, Surf. Coatings Technol. 350 (2018) 323–333.

[63] C. Navas, M. Cadenas, J.M. Cuetos, J. de Damborenea, Microstructure and sliding wear behaviour of Tribaloy T-800 coatings deposited by laser cladding, Wear. 260 (2006) 838–846.

[64] M.J. Tobar, J.M. Amado, C. Álvarez, A. García, A. Varela, A. Yáñez, Characteristics of Tribaloy T-800 and T-900 coatings on steel substrates by laser cladding, Surf. Coatings Technol. 202 (2008) 2297–2301.

[65] M.H. Staia, M. Cruz, N.B. Dahotre, Wear resistance of a laser alloyed A-356 aluminum/WC composite, Wear. 251 (2001) 1459–1468.

[66] D. Gu, Y. Hagedorn, W. Meiners, K. Wissenbach, Nanocrystalline TiC reinforced Ti matrix bulk-form nanocomposites by Selective Laser Melting (SLM): Densification , growth mechanism and wear behavior, Compos. Sci. Technol. 71 (2011) 1612–1620.

[67] A. Mertens, D. Ruffoni, T.M. Enrici, Personal notes of Materials selection, (2018).

[68] E. Luc, M. Bigerelle, R. Deltombe, M. Dubar, The representative topography of worn hot rolling mill cylinders, Tribol. Int. 82 (2015) 387–399.

[69] H. Torres, T. Vuchkov, S. Slawik, C. Gachot, B. Prakash, M. Rodríguez Ripoll, Self-lubricating laser claddings for reducing friction and wear from room temperature to 600 °C, Wear. 408–409 (2018) 22–33.

[70] L.J. Yang, Determination of the wear coefficient of tungsten carbide by a turning operation, Wear. 250–251 (2001) 366–375.

[71] C. Rodenburg, W.M. Rainforth, A quantitative analysis of the influence of carbides size distributions on wear behaviour of high-speed steel in dry rolling/sliding contact, Acta Mater. 55 (2007) 2443–2454.

[72] D.N. Hanlon, W.M. Rainforth, The rolling sliding wear response of conventionally processed and spray formed high speed steel at ambient and elevated temperature, Wear. 255 (2003) 956–966.

[73] S. Zhou, X. Dai, H. Zheng, Microstructure and wear resistance of Fe-based WC coating by multi-track overlapping laser induction hybrid rapid cladding, Opt. Laser Technol. 44 (2012) 190–197.

[74] L.M. Vilhena, C.M. Fernandes, E. Soares, J. Sacramento, A.M.R. Senos, A. Ramalho, Abrasive wear resistance of WC-Co and WC-AISI 304 composites by ball-cratering method, Wear. 346–347 (2016) 99–107.

[75] P. Xu, C. Lin, C. Zhou, X. Yi, Wear and corrosion resistance of laser cladding AISI 304 stainless steel/Al2O3 composite coatings, Surf. Coatings Technol. 238 (2014) 9–14.

[76] W.J. Wang, W.J. Jiang, H.Y. Wang, Q.Y. Liu, M.H. Zhu, X.S. Jin, Experimental study on the wear and damage behavior of different wheel/rail materials, Proc. Inst. Mech. Eng. Part F J. Rail Rapid Transit. 230 (2016) 3–14.

[77] N.F. Garza-Montes-de-Oca, W.M. Rainforth, Wear mechanisms experienced by a work roll grade high speed steel under different environmental conditions, Wear. 267 (2009) 441–448.

[78] B. Bhushan, Principles and applications of effects, 8 (1999) 131.

[79] L.J.O. Donnell, Tribology of 316L Austenitic Stainless Steel, Wear. (2010).

[80] K.L. Johnson, Contact Mechanics, Cambridge University Press, Cambridge, 1985.

[81] I. Hutchings, Tribology Friction and Wear of Engineering Materials, Butterworth-Heinemann, Oxford, 2017.

[82] G.W. Stachowiak, Engineering Tribology, fourth, Butterworth-Heinemann, Oxford, 2013.

[83] M. Vardavoulias, The role of hard second phases in the mild oxidational wear mechanism of high-speed steel-based materials, Wear. 173 (1994) 105–114.

[84] A. Kapoor, F.J. Franklin, Tribological layers and the wear of ductile materials, Wear. 245 (2000) 204–215.

[85] A. Martucci, Personal notes of Fondaments of materials science, in: University of Padova, Italy, 2014.

[86] Höganäs, (n.d.). https://www.hoganas.com/ (accessed May 19, 2019).

[87] Struers, (n.d.). https://www.struers.com/ (accessed May 20, 2019).

[88] Olympus BX60. https://www.olympus-global.com/technology/museum/micro/1993_02/ (accessed May 20, 2019).

[89] Phillips XL30 ESEM. https://www.mtm.kuleuven.be/equipment/ESEM-XL30-FEG/ESEM-XL30-FEG (accessed May 20, 2019).

[90] EMCO M1C. http://www.smoregrava.net/emcof1p.htm (accessed May 20, 2019).

[91] Anton Paar, https://www.anton-paar.com/ca-fr/a-propos/actualites/actualites/detail/anton-paar-gmbh-acquires-csm-instruments-sa/ (accessed May 20, 2019).

[92] C.S.M.T. Features, CSM Technical Features //// HIGH TEMPERATURE TRIBOMETER (THT), 2009.

[93] N. Hashemi, A. Mertens, H.M. Montrieux, J.T. Tchuindjang, O. Dedry, R. Carrus, J. Lecomte-Beckers, Oxidative wear behaviour of laser clad High Speed Steel thick deposits: Influence of sliding speed, carbide type and morphology, Surf. Coatings Technol. 315 (2017) 519–529.

[94] Alicona, Alicona Cobots Real3D, (2017).

[95] T. Maurizi Enrici, Metallurgical Study on Hard Fe-based Composites obtained by Ultra-Fast-Cooling, University of Liège, 2020.

[96] T. Maurizi Enrici, Elucidation of the solidification sequence of a complex graphitic HSS alloy under a combined approach of DTA and EBSD analyses, (2019).

[97] T. Maurizi Enrici, D. Mario, O. Dedry, J.T. Tchuindjang, A. Mertens, Recent advances on 316L+WC Composite Coatings Processed by Laser Cladding, in: Leuven, 2019.

[98] T.F. Liu, S.W. Peng, Y.L. Lin, C.C. Wu, Orientation relationships among M23C6, M6C, and austenite in an Fe-Mn-Al-Mo-C alloy, Metall. Trans. A. 21 (1990) 567–574.

[99] P. Ding, G. Shi, S. Zhou, As-cast carbides in high-speed steels, Metall. Trans. A. 24 (1993) 1265–1272.

[100] S.C. Tjong, K.C. Lau, Sliding wear of stainless steel matrix composite reinforced with TiB2particles, Mater. Lett. 41 (1999) 153–158.

10. Annexes

10.1 Annex A: Datasheet SS316L powder

Höganäs

CERTIFICATE OF ANALYSIS Page: 1(1)

Lot number	Print date	
2524517	2018-01-30	
Order no	Delivery	Shipment
0010399939	2079360	3410286

Item name
316 L-5520
Item number
111904

Customer 94660
UNIVERSITE DE LIEGE
Adm.Ress fin. service controle fact.
Plade du Vingt-Aoüt, 7
B-4000 LIEGE
Belgium

Quantity **40.0** Kg
Your reference **ULG18/1800413/R**

	Test result	Unit	Specification MIN	MAX	ISSUE 1
CHEMICAL PROPERTIES					
Carbon	0.015	%		0.030 %	
Molybdenum	2.5	%	2.0	3.0 %	
Nickel	12.6	%	10.0	14.0 %	
Iron is BALANCE					
Manganese	1.5	%	1.0	2.0 %	
Chromium	16.9	%	16.0	18.0 %	
Silicon	0.7	%		1.0 %	
PHYSICAL PROPERTIES					
Apparent density (Hall)	4.14	g/cm3			
Flowrate (Hall)	17.3	sec/50g			
SIEVE ANALYSIS					
+180 Microns	0.00	%		0.00 %	
+150 Microns	0.04	%		3.00 %	
+125 Microns	3.84	%		25.00 %	
+106 Microns	13.20	%			
+71 Microns	49.46	%			
+63 Microns	23.58	%			
+53 Microns	9.02	%		15.00 %	
+45 Microns	0.84	%		1.00 %	
-45 Microns	0.02	%		0.20 %	

10:42:10

2018-01-30

BE 1

COAMMS180AH-A4

Approved by

Carl Mary
Quality Control Manager

Inspection certificate
EN 10 204 3.1

Hoganas Belgium S.A.
Ruelle Gros Pierre 10
B-7800 ATH

Telephone 32 68 268989
Fax 32 68 285775

BANK: Nordea Bank AB, Frankfurt Branch
SWIFT/BIC : NDEADEFF
IBAN (EUR): DE39 5143 0300 6602 6600 01
IBAN (USD): DE12 5143 0300 6602 6600 02
IBAN (GBP): DE82 5143 0300 6602 6600 03

RPM Tournai
BE 0422.056.601

130

10.2 Annex B: Datasheet WC powder

Höganäs

CERTIFICATE OF ANALYSIS

Lot number 2617697	Print date 2018-01-30	
Order no 0010399939	Delivery 2079360	Shipment 3410286

Item name
4590
Item number
104459

Customer
UNIVERSITE DE LIEGE
Adm.Ress fin. service controle fact.
Plade du Vingt-Aoot, 7
B-4000 LIEGE
Belgium

94660

Quantity
20   **Kg**

Your reference
ULG18/1800413/R

	Test result	Unit	Specification MIN	MAX	ISSUE 1
CHEMICAL PROPERTIES					
Carbon	4.0	%	3.5	4.2 %	
Tungsten is BALANCE					
Iron	0.2	%		0.5 %	
Others (Total)	0.1	%		0.2 %	
SIEVE ANALYSIS					
+212 Microns	0	%		0 %	
+180 Microns	0.0	%		0.5 %	
+150 Microns	1.9	%		5.0 %	
+90 Microns	61.8	%			
+53 Microns	35.9	%			
+45 Microns	0.3	%			
-53 Microns	0.4	%		2.0 %	
-45 Microns	0.2	%		0.2 %	

Approved by

Carl Mary
Quality Control Manager

Inspection certificate
EN 10 204 3.1

10.42.09

2018-01-30

BE 1

COMMS480AH-A4